A KARHUNEN-LOÈVE LEAST-SQUARES TECHNIQUE FOR OPTIMIZATION OF GEOMETRY OF A BLUNT BODY IN SUPERSONIC FLOW

A Dissertation

Submitted to the Graduate School
of the University of Notre Dame
in Partial Fulfillment of the Requirements
for the Degree of

Doctor of Philosophy

by

Gregory P. Brooks, B.S.A.E., M.S.A.E.

Joseph M. Powers, Director

Graduate Program in Aerospace and Mechanical Engineering
Notre Dame, Indiana
June 2003

A KARHUNEN-LOÈVE LEAST-SQUARES TECHNIQUE FOR OPTIMIZATION OF GEOMETRY OF A BLUNT BODY IN SUPERSONIC FLOW

Abstract

by

Gregory P. Brooks

Accuracy and efficiency of the Karhunen-Loève (KL) method is compared to a pseudospectral method employing global Lagrange interpolating polynomials for a two-dimensional linear heat conduction problem and for the supersonic flow of an inviscid, calorically perfect ideal gas about an axisymmetric blunt body. For the heat conduction problem, efficiency and accuracy of a KL Galerkin model, pseudospectral approximation, and a second order finite difference approximation are compared for two sets of boundary conditions: one with an infinite number of modes and a second with a finite number of modes. For both the infinite and finite mode boundary conditions, the KL Galerkin model achieves an accuracy consistent with the underlying pseudospectral solver in as few as five modes. Not including the cost of sampling the design space and building the KL model, the KL Galerkin model is an order of magnitude faster than the pseudospectral method for the finite mode boundary condition, two orders of magnitude faster than the pseudospectral method for the infinite mode boundary condition, and five orders of magnitude faster than the finite difference for both types of boundary conditions at an accuracy level of 10^{-4} as measured against a separation of variables solution. In the supersonic blunt body problem, the bow shock is fitted, and the Euler equations are solved in generalized

coordinates using both a KL least-squares model and a pseudospectral method. Not including the cost of sampling the design space and building the KL model, the KL least-squares method requires almost half the CPU time as the pseudospectral method to achieve the same level of accuracy. Single variable design problems are solved for both the heat conduction problem and the supersonic blunt body problem using the pseudospectral solver and the KL model; in both problems, the KL model optimal design predictions are within the expected level of accuracy of the KL models. For both problems, a response surface which is a quadratic polynomial fit of the design problem objective function versus the geometric design variable is built from a design space sampling of three pseudospectral solutions. For the heat conduction problem, the KL model is significantly more accurate than the response surface over most of the design space, while for the blunt body design problem, the KL model is slightly less accurate than the response surface. Since the KL model requires more CPU time, the single variable blunt body design problem posed here offers no advantage over a response surface in terms of CPU time. Nevertheless, the accuracy of the response surface is strongly dependent on the problem, whereas the KL method achieves a consistently low level of error for both the heat conduction and supersonic blunt body problems considered.

CONTENTS

FIGURES

ACKNOWLEDGEMENTS

I would like to thank my advisor, Dr. Joseph M. Powers, for his direction in this research and his friendship over the past four years. I would like to thank Drs. Stephen M. Batill, Samuel Paolucci, H.-C. Chang, and Jonathan L. Mace for serving on my committee and for their helpful comments. I am grateful for the help and friendship of my fellow graduate students in Room 300 Cushing especially Dr. Sandeep Singh, Messrs. Andrew Henrick, Benito Torres, M. Brett McMickell, John Kamel, and Damrongsak Wirasaet.

I would like to thank the U.S. Air Force Palace Knight Program for their generous financial support which allowed me to pursue my work and partial summer support from Los Alamos National Laboratory. Finally, I would like to thank God for His constant love and support, without Him none of this would have been possible.

SYMBOLS

English Symbols

a_i^q	KL approximation coefficient for q^{th} component, $i = 1, ..., L$
A_1	nonlinear function in shock acceleration equation
A_2	nonlinear function in shock acceleration equation
A_3	nonlinear function in shock acceleration equation
$\mathbf{A}$	flux Jacobian matrix associated with ξ direction
b	geometric design variable
b_k	distinct value of the geometric design variable
$\mathbf{B}$	flux Jacobian matrix associated with η direction
c	acoustic speed
c_v	specific heat at constant volume
C_D	drag coefficient
C_p	pressure coefficient
c_p	specific heat at constant pressure
$\mathbf{e}_f$	least-squares error function associated with $\widehat{\mathbf{f}}$
$\mathbf{e}_g$	least-squares error function associated with $\widehat{\mathbf{g}}$
$\mathbf{e}_\eta$	unit vector in the η direction
$\mathbf{e}_{BT}$	unit vector in the direction tangent to the body
$\mathbf{e}_{BN}$	unit vector in the direction normal to the body
$\mathbf{e}_{ST}$	unit vector in the direction tangent to the shock
$\mathbf{e}_{SN}$	unit vector in the direction normal to the shock

$\mathbf{e}_r$	unit vector in the r direction
$\mathbf{e}_z$	unit vector in the z direction
e	total least-squares error function
e^*	dimensional internal energy
$\mathbf{f}$	nonlinear function in unsteady form of the governing equations
$\widehat{\mathbf{f}}$	nonlinear function in the steady-state least-squares formulation of the blunt body problem
f_p	nonlinear functions in differential-algebraic formulation of the blunt body problem
$\mathbf{g}$	boundary conditions for unsteady form of the blunt body problem
$\widehat{\mathbf{g}}$	boundary conditions for steady-state least-squares formulation of the blunt body problem
g_p	differential-algebraic form of boundary conditions in implicit form
$\widehat{g}_p$	g_p written in explicit form
h	distance between $\eta = 0$ and $\eta = 1$ along lines of constant ξ
$\widetilde{h}$	coefficient of convective heat transfer
h^*	dimensional enthalpy
h_o	stagnation enthalpy
$\mathbf{h(x)}$	nonlinear function in the ODE form of the blunt body problem
J	determinant of the metric Jacobian matrix
$\mathbf{J}$	metric Jacobian matrix
k	KL mode number counter
K	number of snapshots in the KL model
L	number of modes in the KL model
L_B^*	length scale in the heat conduction and blunt body problems
$L_n^N(\xi)$	n^{th} global Lagrange interpolating polynomial of order N

$L_m^M(\eta)$	m^{th} global Lagrange interpolating polynomial of order M
$L_\infty[\Omega]$	infinity norm over the domain Ω
$\mathcal{M}$	Mach number
$\mathcal{M}_\infty$	freestream Mach number
M	number of nodes in the η direction
N	number of nodes in the ξ direction
p	pressure
$\mathbf{P}$	left eigenvector matrix of flux Jacobian matrix $\mathbf{B}$
P_1	number of ODEs in pseudospectral approximation to the blunt body problem
P_2	number of equations in pseudospectral approximation to the blunt body problem
q^*	component of $\mathbf{q}^*$ in the η direction
$\mathbf{q}^*$	dimensional heat flux vector
Q	number of rows in $\mathbf{X}$ which are also the number of dependent variables in the governing equations
$\dot{Q}$	constant heat flow rate per unit depth
$\mathbf{R}$	autocorrelation matrix
r	radial coordinate
R	radial coordinate at the blunt body surface
R^*	dimensional specific gas constant
S	boundary of the domain Ω
s	entropy
$\mathbf{s}$	source vector function
t	time in physical coordinate system
T	temperature

$I_{NM}T$	interpolating polynomial approximation to T
u	radial component of velocity
u_r	velocity component in the r direction
u_θ	velocity component in the θ direction
$\widehat{u}$	contravariant velocity component
$\mathbf{v}$	velocity vector
v	component of shock velocity in η direction
v_{BN}	velocity component in the direction normal to the body
w	axial component of velocity
$\widehat{w}$	contravariant velocity component
$\mathbf{X}$	snapshot matrix
x_p	p^{th} component of $\mathbf{x}$
$\mathbf{x}$	vector of unknowns in ODE form of blunt body problem
$\mathbf{y}$	unsteady solution vector
y^q	q^{th} component of $\mathbf{y}$
y_p	unknowns in differential-algebraic form of blunt body problem
$\widehat{\mathbf{y}}$	steady state solution vector
$\widetilde{\mathbf{y}}$	KL approximation of $\widehat{\mathbf{y}}$
$\widetilde{y}^q$	q^{th} component of $\widetilde{\mathbf{y}}$
z	axial coordinate
Z	axial coordinate on the blunt body surface
$\mathbf{z}$	vector of primitive variables

Greek Symbols

α^*	dimensional coefficient of thermal diffusivity
β	Biot number
δ	post shock angle of fluid velocity with respect to the symmetry axis

δ_S component of fluid velocity normal to the shock in the shock-attached reference frame on the downstream side of the shock

δ_∞ component of fluid velocity normal to the shock in the shock-attached reference frame on the upstream side of the shock

δ_{mj} Kronecker delta

θ circumferential coordinate in the counter-clockwise direction

$\widehat{\theta}$ circumferential coordinate in the clockwise direction

θ_C semi-vertex angle of conical body

θ_S cone flow shock angle with respect to z axis

κ^* dimensional thermal conductivity

λ_k^q eigenvalues associated with $\varphi_k^q(\xi, \eta)$

$\mathbf{\Lambda}_\eta$ η direction flux Jacobian eigenvalue matrix

ξ spatial variable in computational coordinate system

η spatial variable in computational coordinate system

γ ratio of specific heats

Γ aspect ratio

Ω spatial domain

ω_g^q weight associated with e_g^q

$\boldsymbol{\omega}$ vorticity vector

ω_θ component of vorticity in the direction normal to the $r - z$ plane

ρ density

σ_i characteristic roots for separation of variables solution

τ time in computational coordinate system

φ_k^q KL eigenmodes

Superscripts

$*$ dimensional quantity

-1	inverse

Subscripts

0	initial condition
k	KL mode number
BN	quantity in the direction normal to the body surface
BT	quantity in the direction tangent to the body surface
o	stagnation quantity
S	post shock value
SN	quantity in the direction normal to the shock
ST	quantity in the direction tangent to the shock
∞	freestream or surrounding medium quantity

CHAPTER 1

INTRODUCTION

Computer-assisted multi-disciplinary design and optimization in the aeronautical engineering community is a promising area of current research. The optimization of air vehicles has often relied on low fidelity aerodynamic models due to the need for rapid evaluation of aerodynamic design variables such as lift, drag, or heat transfer. Unfortunately, the use of low fidelity models can lead to unacceptable uncertainties in the final optimal design, especially where design safety margins are tight [1]. In addition, low fidelity models often do not provide the complete flow field information such as pressure, temperature, and velocity distributions, acoustic signature, shock wave location, which the designer may require. For these reasons, high fidelity models such as the Euler or Navier Stokes equations are often required. For most problems, these model equations can be solved only after discretization.

A major difficulty in employing discrete solvers in a multi-disciplinary design process is the large central processing unit (CPU) requirements of these codes. It is not uncommon for discrete solutions to three dimensional flows around complex aircraft configurations to require on the order of ten or more hours of CPU time per steady state solution [1], and these solutions are often not fully resolved. Complete resolution of complex flow structures could require considerably more CPU time. A design incorporating multiple disciplines, *e.g.* aerodynamics, structures, controls, may easily have hundreds or even thousands of design variables. While interdisci-

plinary coordination schemes using varying fidelity models [2] help to alleviate the CPU cost associated with interdisciplinary dependence, the aerodynamics discipline alone could still involve hundreds or more design variables. For this reason, current gradient-based numerical optimizers can be prohibitively expensive when used directly with discrete solvers of high fidelity models, and approximation becomes necessary.

One popular approximation technique for the design of complex, multi-variable problems is the response surface approximation [3]. Response surfaces typically approximate quantities such as the lift and drag of the vehicle as a function of the design variables, *e.g.* geometric parameters, by simple functional forms which interpolate among a set of solutions. The solutions among which the response surface interpolates are obtained from more costly solvers such as high fidelity discrete solvers. An advantage of the response surface method is that both objective function and gradient evaluation are rapid. Furthermore, polynomial approximation of the objective function ensures that the gradients are continuous. This increases the efficiency of the numerical optimizer in the sense that fewer iterations may be needed to reach an optimum. Disadvantages of the response surface method include a potential lack of accuracy in capturing the system response by a simple function, a strong dependence of computational cost on the number of design variables, and loss of detailed flow field information unless the flow solutions from which the model was built are stored. While it is theoretically possible to construct response surfaces for flow quantities at multiple locations in the flow, it is difficult to implement in practice. Flow field information may be needed for design of a thermal protection system, for coupling with a structural code in static and aeroelastic design, for inverse vehicle design in sonic boom mitigation, acoustic or radar signature reduction, or for shock wave placement for efficient high speed propulsion.

A recently developed method which does yield detailed flow field information by solution of the governing equations such as the Euler or Navier-Stokes equations is the adjoint method [4, 5, 6] adopted from control theory [7]. This method is computationally efficient for gradient-based optimizers since objective function gradients with respect to an arbitrary number of design variables can be approximated by solving a single adjoint equation. Since the adjoint equation is of similar complexity as the governing equations, each iteration of the optimizer regardless of the number of design variables is equivalent in computational cost to two flow field solutions. The fact that the computational cost of the adjoint method does not increase with the number of design variables is a significant advantage over the response surface method whose computational cost increases with increasing number of design variables. Although still in development, the adjoint method appears to be promising as an accurate and efficient means of multidisciplinary, multi-variable optimal design. Nevertheless, the adjoint method has the disadvantage of requiring that a unique adjoint equation be derived and solved for each new design objective function that may be formulated. Since the adjoint equation is of similar complexity to the governing equations themselves, a discrete solver would be required which could yield accurate approximations to a range of various adjoint equations which the designer may wish to formulate.

Another approximation technique is the Karhunen-Loève (KL) method. This technique is a method of weighted residuals where the trial functions are eigenfunctions of the averaged auto-correlation of previous numerical flow-field solutions. It can be shown that the KL decomposition yields an optimal set of orthonormal basis functions in the sense that the fewest number of functions of all possible bases are required for a given level of accuracy in reconstructing the original set of data. Employing the KL modes as the trial functions of a Galerkin [8], orthogonal collo-

cation [9], or least-squares [10] method of weighted residuals, reduced dimension models have been developed which yield accurate solutions to partial differential equations for a computational cost several orders of magnitude lower than discrete solvers. Advantages of the KL method over response surfaces are the automatic generation of detailed flow field information in a straightforward manner, and a potential increase in accuracy. The KL method also has the advantage that the KL decomposition of the flow field solutions can also be used as a data compression strategy for the flow solutions by discarding higher order KL modes and thus reduce storage requirements. This could be particularly advantageous for multivariable design problems where a large number of flow field solutions are required to adequately sample the design space. The KL method also has advantages over the adjoint method in that the KL model is independent of the design problem formulation. This flexibility in specifying the design problem is an important attribute for an optimal design code [11]. Nevertheless, the computational cost of the KL method, unlike the adjoint method, increases with increasing number of design variables.

We next review some applications of the KL theory in optimization and modelling of thermo-fluid systems. The KL decomposition has been used in conjunction with the Galerkin method of weighted residuals to develop approximate models of turbulent fluid mechanical phenomena, *e.g.* Aubry, *et al.* [12], and Sirovich and Park [13, 14]. The first use of the KL method for a control application was by Chen and Chang [15] , where it was used to control spatiotemporal patterns on a catalytic wafer using experimentally determined KL modes. Independently, Park and Cho [16] developed a KL Galerkin model of a nonlinear heat equation for control or parameter estimation; more recently the KL Galerkin method has been used to approximate Navier-Stokes solutions for flow control [17, 18, 19], inverse con-

vection [20, 21, 22, 23, 24], and radiation [25] problems. Theodoropulou, *et al.* [9] successfully implemented what they called an "orthogonal collocation" method with KL modes for the optimization of rapid thermal chemical vapor deposition systems in one dimension.

The KL method has been applied to compressible flow problems by LeGresley and Alonso [10] who used a KL least-squares model of the Euler equations in a finite volume formulation to optimize the pressure distribution around an airfoil in subsonic flow and more recently extended the method via domain decomposition to include the high subsonic region with mild shocks, [26]. Lucia [27] developed KL models for one, and simple two dimensional geometries in supersonic flow by using a domain decomposition method to isolate the shock, and applying the KL method to only the smooth regions of the flow field. The region of the flow containing the shock is approximated via a shock capturing technique. A KL least-squares model for the supersonic flow over a blunt body using shock-fitting was developed by Brooks and Powers [28]. The KL model of the supersonic blunt body problem will be presented with more details in the current work.

We briefly review the literature on solutions to the supersonic flow over blunt body geometries. Rusanov [29] and Hayes and Probstein [30] have given thorough reviews of early contributions, of which a few will be mentioned. Two methodologies for calculating solutions to the supersonic flow about a blunt body are the direct and inverse methods. In the direct method the body shape is specified, and then the shock shape and flow field are calculated. In the inverse method the shock shape is specified, and the body shape which would support that shock shape is calculated. At first, studies concerning the inverse problem were based on series expansion of the governing equations in the vicinity of the shock wave [31]. Later, numerical solutions to the inverse, supersonic blunt body problem were performed

by Garabedian and Lieberstein [32] and Van Dyke [33]. Evans and Harlow [34] were the first to generate numerical solutions to the direct problem by integrating the unsteady Euler equations to a relaxed steady state solution. Moretti and Abbett [35] used finite differences and fitting of the shock to generate accurate solutions of the Euler equations about a blunt body; this laid the foundation for subsequent shock-fitting numerical schemes. Pseudospectral approximations to the Euler equations employing shock-fitting with spectral filtering were first performed by Hussaini, *et al.* [36] and without spectral filtering by Kopriva [37] and later by Brooks and Powers [38, 39], who extended the work of Kopriva to systematically cast the equations in a standardized form for numerical analysis.

The first step in generating a KL model is to develop a set of numerical solutions to the governing equations for a range of design variables or in this case, a single design variable. The shock-fitting, pseudospectral method described by Brooks and Powers [39] is employed for this step. The shock is fitted since approximation of discontinuous solutions with high order polynomials exhibit the Gibbs phenomenon in the form of global oscillations in the solution [40]. These oscillations can cause the numerical scheme to become unstable, and attempts to remove the oscillations by spectral filtering or by addition of artificial viscosity significantly reduces the accuracy of the numerical method. The more common alternative of shock capturing, while generally stable and non-oscillatory, yields only first order accuracy. The pseudospectral method is chosen since it has the advantage of an exponential grid convergence rate for sufficiently smooth solutions; consequently, relative to finite difference or finite element methods with polynomial convergence rates, pseudospectral methods can generally achieve the same absolute error with a smaller computational cost, or for the same computational effort, pseudospectral methods generate a more accurate solution than finite difference or finite element

methods. The pseudospectral method is chosen rather than a spectral method, such as a Galerkin method, which also exhibits exponential grid convergence rates, since the nonlinear terms in the governing equations and boundary conditions are much easier to approximate using the pseudospectral method. The high accuracy attainable by the pseudospectral method is important for assessing the accuracy of the KL least squares model and for proper resolution of high order KL modes. Since the magnitude of the KL modes decreases rapidly with increasing mode number, more high order modes can be reliably resolved from a pseudospectral method than from finite difference or finite volume methods. In addition, since the solution is known in terms of high order polynomials, the KL modes can also be expressed in terms of polynomials, and integration of the KL modes necessary for the least squares method can be performed exactly by means of Gaussian quadrature, thus maintaining the high accuracy of the method.

We briefly review pseudospectral methods. An early unified mathematical description of the theory of spectral and pseudospectral methods was given by Gottlieb and Orszag [40]. Significant advances occurred in the late 1970's and early 1980's and are well documented by Canuto, *et al.* [41], with particular application to fluid dynamics. For a more recent review, see Gottlieb and Hesthaven [42].

There does not appear to be complete consensus in the literature for the definition of pseudospectral; a definition is adopted here which we believe useful and consistent with that of Fornberg [43]. We define a pseudospectral method to be a collocation type of method of weighted residuals, as defined by Finlayson [44], in which the error in the solution to the governing equations is driven to zero at collocation points; the flow quantities are represented in terms of global interpolating polynomials defined at the collocation points. The spatial derivatives are approximated by taking derivatives of the interpolating polynomials and evaluating

the derivatives at the collocation points. The interpolating polynomials used in the current work are global Lagrange interpolating polynomials, where the algorithm for finding derivatives of these polynomials is taken from Fornberg [43]. A property of the pseudospectral method is that approximations to derivatives have global support in one dimension, making it equivalent to a finite difference scheme with a stencil that extends over the entire domain. As the number of points is increased, the size of the stencil grows, leading to solutions which converge at an ever faster rate. The pseudospectral method is easily extended to multiple dimensions by approximating the flow quantities as products of one dimensional interpolating polynomials.

The second step in the development of the KL model is to perform a KL decomposition on the characteristic solution set generated by the flow solver. The KL decomposition, also called Proper Orthogonal Decomposition (POD), appears to have been developed independently in the 1940's by several researchers including Karhunen [45] and Loève [46]. Lumley [47] proposed the KL decomposition as a rational procedure for the extraction of coherent structures in a turbulent flow field. The KL decomposition is also closely related to the singular value decomposition and principal component analysis used in data compression and image processing [48]. As originally introduced by Lumley, the KL decomposition was impractical for more than one spatial dimension. It was not until Sirovich [49] introduced the method of snapshots that the KL decomposition became practical for highly resolved, three dimensional flows.

The final step in the development of the KL model is to approximate the governing equations and boundary conditions in a series expansion of the KL modes and solve for the coefficients in the expansion via a least squares, Galerkin, or collocation method of weighted residuals. For the current work, a KL Galerkin model will be developed for a two-dimensional heat conduction problem and a KL least

squares model will be developed for the supersonic flow over a blunt body geometry. The least squares method was employed for the blunt body problem because the KL Galerkin model was not numerically stable when more than one mode was employed in the model.

In the remainder of this dissertation, we will give an overview for the development of the KL Galerkin and least-squares models including the fundamental equations. Next, a KL Galerkin model is developed for a two-dimensional heat conduction problem following the three steps just described above. The heat conduction problem will be posed with two different boundary conditions: an infinite mode boundary condition and a finite three-mode boundary condition. The finite mode boundary condition is constructed such that the exact separation of variables solution consists of only three terms in the series solution, while the infinite mode boundary condition has an exact separation of variables solution with an infinite number of terms in the series expansion of the solution. The infinite mode and finite mode boundary conditions were chosen in order to evaluate the efficiency of the KL Galerkin model of the heat conduction problem for problems with both few and multiple spatial scales. After presenting results of the accuracy and efficiency of the KL Galerkin model compared to both a second order finite difference and pseudospectral solvers, a single variable design problem is solved using both the KL Galerkin model and the pseudospectral solver.

Next, the supersonic blunt body problem is posed including the physical and computational grids, the primitive variable formulation of the governing equations and their transformation to generalized coordinates, the boundary conditions and the discretized form of the equations. After discretization the resulting system of differential-algebraic equations (DAEs) is cast into the form of a system of ordinary differential equations (ODEs) which can be solved using standard software packages.

Validation and verification results for the pseudospectral flow solver are presented. Next, ten pseudospectral solutions, are generated for ten different values of a single geometric variable, and the KL modes corresponding to these ten solutions are then presented. The KL least-squares model of the blunt body problem is subsequently presented along with error convergence plots with respect to the number of KL modes used in the model. The error in the KL model is measured against a highly resolved solution from the pseudospectral solver. Finally, a single-variable optimal design problem is posed and then solved using both the KL least-squares model and the pseudospectral solver. The accuracy of the KL model is compared to that of the pseudospectral solver for the single-variable optimal design problem.

Contributions of the current work include assessing the computational efficiency of the KL method in comparison with other discrete approximations such as a second order finite difference and pseudospectral method, and with response surfaces. The current work is also unique in evaluating the efficiency and accuracy of the KL method for different classes of problems: a linear problem, a nonlinear problem, a problem with an infinite mode boundary condition, and a problem with a finite mode boundary condition. Finally, the current work is novel in that it is the first work to use shock fitting with the KL method, and one of the first studies where a KL model has been developed for a geometry in a supersonic flow.

CHAPTER 2

KARHUNEN-LOÈVE DESIGN OPTIMIZATION STRATEGY

Here we give an overview of the three steps for developing a KL Galerkin or least-squares model. The design space is sampled using a discrete solver, pseudospectral solver in this case, then the KL decomposition is performed yielding a set of KL modes, and finally approximation of the governing equations and boundary conditions in terms of the KL modes leads to a reduced dimension model of the problem.

2.1 Design Space Sampling

The first step in developing a KL model for use in optimization is to generate a set of K characteristic solutions or snapshots which span the design space of interest in the problem. In the current study, the design space is parameterized by a single geometric variable, b for the blunt body problem and Γ for the heat conduction problem. The method is theoretically easy to extend to multivariable optimization problems. For the current work, the characteristic solutions are generated from a pseudospectral solver. Let us consider the following system of time-dependent partial differential equations, boundary conditions, and initial conditions in two space dimensions, ξ and η, defined over the domain

$$\Omega : \{\xi \in [0,1], \eta \in [0,1]\}, \tag{2.1}$$

and bounded by S,

$$\frac{\partial \mathbf{y}}{\partial \tau} + \mathbf{f}\left(\mathbf{y}, \frac{\partial \mathbf{y}}{\partial \xi}, \frac{\partial \mathbf{y}}{\partial \eta}, \frac{\partial^2 \mathbf{y}}{\partial \xi^2}, \frac{\partial^2 \mathbf{y}}{\partial \eta^2}\right) = \mathbf{0}, \tag{2.2}$$

$$\mathbf{g}\left(\mathbf{y}, \frac{\partial \mathbf{y}}{\partial \xi}, \frac{\partial \mathbf{y}}{\partial \eta}\right) = \mathbf{0}, \tag{2.3}$$

along with the initial conditions,

$$\mathbf{y}\left(\xi, \eta, 0\right) = \mathbf{y}_0\left(\xi, \eta\right), \tag{2.4}$$

For the heat conduction problem, $\mathbf{y}\left(\xi, \eta, \tau\right) : \mathbb{R}^3 \rightarrow \mathbb{R}^1$, and $\mathbf{f} : \mathbb{R}^3 \rightarrow \mathbb{R}^1$, and $\mathbf{g} : \mathbb{R}^3 \rightarrow \mathbb{R}^4$. For the blunt body problem [39], $\mathbf{y}\left(\xi, \eta, \tau\right) : \mathbb{R}^3 \rightarrow \mathbb{R}^{10}$, and $\mathbf{f} : \mathbb{R}^3 \rightarrow \mathbb{R}^{10}$, and $\mathbf{g} : \mathbb{R}^3 \rightarrow \mathbb{R}^{11}$, where the function $\mathbf{y}\left(\xi, \eta, \tau\right)$ consists of six terms, $y^q\left(\xi, \eta, \tau\right)$, $q = 1, ..., 6$, defined over Ω and four terms, $y^q\left(\xi, \eta, \tau\right)$, $q = 7, ..., 10$, defined over S. All of the algebraic constraints, Eq. (2.3), are boundary conditions and thus apply only on S. Although Eq. (2.2) is time-dependent, for the optimal design problem only steady state solutions are considered. Solving the time-dependent equation to a relaxed steady state is a convenient numerical solution technique and computationally easier than directly solving the formally steady problem, although less efficient.

The system of equations in Eqs. (2.2) and (2.3) along with initial conditions, Eq. (2.4) are solved for K distinct values of the geometric variable denoted now as b_k, $k = 1, ..., K$, at steady state. We make the following definition

$$X_k^q(\xi, \eta) = y^q(\xi, \eta, \tau \rightarrow \infty; b_k), \quad \begin{array}{l} q = 1, ..., Q, \\ k = 1, ..., K, \end{array} \tag{2.5}$$

where $Q = 1$ for the heat conduction problem and $Q = 6$ for the blunt body problem, and construct the following $K \times Q$ matrix of functions $\mathbf{X}\left(\boldsymbol{\xi}\right)$ where for this problem $\boldsymbol{\xi} \equiv (\xi, \eta)$,

$$\mathbf{X}\left(\boldsymbol{\xi}\right) = \begin{bmatrix} X_1^1(\boldsymbol{\xi}) & \cdots & X_K^1(\boldsymbol{\xi}) \\ \vdots & \ddots & \\ X_1^Q(\boldsymbol{\xi}) & & X_K^Q(\boldsymbol{\xi}) \end{bmatrix}. \tag{2.6}$$

The function $\mathbf{X}(\boldsymbol{\xi})$ contains a solution for a particular geometry b_k in each of its columns; the rows of $\mathbf{X}(\boldsymbol{\xi})$ are composed of a particular independent variable for the span of the geometries.

2.2 Karhunen-Loève Decomposition

The second step in the development of the KL model is to perform a separate KL decomposition on each row of $\mathbf{X}(\boldsymbol{\xi})$. Since there are six rows for the blunt body problem, the KL decomposition will be performed six times, while for the heat conduction problem the KL decomposition is performed only once since the problem consists of a single scalar equation. In Appendix A, we derive the KL decomposition using a more detailed and transparent process than often is given in the literature. It is shown that the eigenfunctions, $\varphi_k^q(\boldsymbol{\xi})$, $k = 1, ..., K$, of the kernel $\mathbf{R}^q(\boldsymbol{\xi},\boldsymbol{\xi}') = \frac{1}{K}\sum_{m=1}^{K} X_k^q(\boldsymbol{\xi}) X_k^q(\boldsymbol{\xi}')$, are orthonormal and form on average the most efficient linear basis, in a least-squares error sense, for constructing a truncated series approximation to any of the $X_k^q(\boldsymbol{\xi})$, $k = 1, ..., K$, where $q = 1, ..., Q$, denote the dependent variables of the problem.

2.3 Karhunen-Loève Galerkin Model

For the case of the heat conduction problem, the final step in developing a KL Galerkin model is a projection of the solution space of the differential equation onto the $\varphi_j(\boldsymbol{\xi})$. Let us approximate $\mathbf{y}(\xi, \eta, \tau)$ from Eqs. (2.2) and (2.3), or simply $y(\xi, \eta, \tau)$, since Eq. (2.2) is a scalar equation, by a series expansion in the KL eigenfunctions, $\varphi_k^1(\xi, \eta)$, *i.e.*

$$y(\xi, \eta, \tau) \approx \widetilde{y}(\xi, \eta, \tau) = \sum_{i=1}^{L} a_i^1(\tau)\, \varphi_i^1(\xi, \eta), \quad L \leq K. \tag{2.7}$$

The time varying coefficients $a_i^1(\tau)$, $i = 1, ..., L$, are to be determined. Substituting Eq. (2.7) into Eq. (2.2), we define the following residual function

$$e(\xi, \eta, \tau) = \frac{\partial \widetilde{y}}{\partial \tau} + \mathbf{f}\left(\widetilde{y}, \frac{\partial \widetilde{y}}{\partial \xi}, \frac{\partial \widetilde{y}}{\partial \eta}, \frac{\partial^2 \widetilde{y}}{\partial \xi^2}, \frac{\partial^2 \widetilde{y}}{\partial \eta^2}\right), \tag{2.8}$$

which we enforce to be orthogonal to each of the eigenfunctions, $\varphi_i^1(\xi, \eta)$, $i = 1, ..., L$, *i.e.*

$$\int_0^1 \int_0^1 e(\xi, \eta, \tau)\, \varphi_i^1(\xi, \eta) d\xi d\eta = 0, \quad i = 1, ..., L. \tag{2.9}$$

Substituting the expressions for the residual, $e(\xi, \eta, \tau)$, from Eq. (2.8) and $\widetilde{y}(\xi, \eta, \tau)$ from Eq. (2.7) into Eq. (2.9), and making use of the orthogonality of the $\varphi_i^1(\xi, \eta)$, we arrive at the following L equations for the L coefficients, $a_i^1(\tau)$, $i = 1, ..., L$:

$$\frac{d}{d\tau} a_i^1(\tau) + \int_0^1 \int_0^1 \mathbf{f}\left(a_i^1, \frac{\partial \varphi_i^1}{\partial \xi}, \frac{\partial \varphi_i^1}{\partial \eta}, \frac{\partial^2 \varphi_i^1}{\partial \xi^2}, \frac{\partial^2 \varphi_i^1}{\partial \eta^2}\right) \varphi_i^1(\xi, \eta) d\xi d\eta = 0, \quad i = 1, ..., L. \tag{2.10}$$

The boundary conditions from Eq. (2.3) are subsequently incorporated into the solution of Eq. (2.10) by an integration by parts procedure as described in the Appendix D.

2.4 Karhunen-Loève Least-Squares Model

For the case of the blunt body problem, the final step in developing a KL least-squares model is to expand the $y^q(\xi, \eta, \tau \to \infty; b)$, $q = 1, ..., 6$, defined over Ω in terms of the KL modes, $\varphi_k^q(\xi, \eta)$, $q = 1, ..., 6$, $k = 1, ..., K$, from step 2. Let us consider a steady state form of Eqs. (2.2) and (2.3), assuming that a unique, stable steady state solution exists,

$$\widehat{\mathbf{f}}\left(\widehat{\mathbf{y}}, \frac{\partial \widehat{\mathbf{y}}}{\partial \xi}, \frac{\partial \widehat{\mathbf{y}}}{\partial \eta}, \frac{\partial^2 \widehat{\mathbf{y}}}{\partial \xi^2}, \frac{\partial^2 \widehat{\mathbf{y}}}{\partial \eta^2}\right) = \mathbf{0}, \tag{2.11}$$

$$\widehat{\mathbf{g}}\left(\widehat{\mathbf{y}}, \frac{\partial \widehat{\mathbf{y}}}{\partial \xi}, \frac{\partial \widehat{\mathbf{y}}}{\partial \eta}\right) = \mathbf{0}, \tag{2.12}$$

where $\widehat{\mathbf{y}}(\xi,\eta)$ is of dimension six, corresponding to $y^q(\xi,\eta,\tau\rightarrow\infty;b)$, $q=1,...,6$, $\widehat{\mathbf{f}}$ is of dimension four also defined over Ω, and $\widehat{\mathbf{g}}$ is of dimension eight and defined over S. For the current supersonic blunt body problem, the six terms in $\widehat{\mathbf{y}}(\xi,\eta)$ are the density, pressure, two velocity components, and two physical grid coordinates, the four components of $\widehat{\mathbf{f}}$ are the steady-state form of the Euler equations, and the eight components of $\widehat{\mathbf{g}}$ are the appropriate nonlinear boundary conditions. The dimension of $\widehat{\mathbf{g}}$ is reduced from the dimension of $\mathbf{g}$ because linear boundary conditions are not included in $\widehat{\mathbf{g}}$ since they are automatically satisfied by the KL approximation as will be elaborated in a subsequent section. The reduction in the dimensions for $\widehat{\mathbf{y}}$ and $\widehat{\mathbf{f}}$ compared to $\mathbf{y}$ and $\mathbf{f}$ respectively is a result of eliminating the characteristic formulation for several time-dependent boundary conditions in favor of the Euler equations, and dropping the evolution equations for the physical grid coordinates over Ω in favor of algebraic expressions for the physical grid coordinates only at the body surface. Since the problem in Eqs. (2.11) and (2.12) consists of twelve equations and six unknowns, it is overconstrained, and as a consequence, the problem is solved in a least-squares sense. Each component of $\widehat{\mathbf{y}}(\xi,\eta)$, $\widehat{y}^q(\xi,\eta)$, $q=1,...,6$, in Eqs. (2.11) and (2.12) is approximated by a truncated series expansion in the KL eigenfunctions, $\varphi_k^q(\xi,\eta)$, *i.e.*

$$\widehat{y}^q(\xi,\eta)\approx\widetilde{y}^q(\xi,\eta)=\sum_{i=1}^{L}a_i^q\varphi_i^q(\xi,\eta),\qquad\begin{array}{c}q=1,...,6,\\ L\leq K,\end{array}\tag{2.13}$$

so that the a_i^q, $i=1,...,L$, $q=1,...,6$, are the unknowns to be determined. Substituting the approximation $\widetilde{y}^q(\xi,\eta)$ from Eq. (2.13) into Eqs. (2.11) and (2.12), we get the following residual error function for $\widehat{\mathbf{f}}$, $\mathbf{e}_f$,

$$\mathbf{e}_f=\widehat{\mathbf{f}}\left(\widetilde{\mathbf{y}},\frac{\partial\widetilde{\mathbf{y}}}{\partial\xi},\frac{\partial\widetilde{\mathbf{y}}}{\partial\eta},\frac{\partial^2\widetilde{\mathbf{y}}}{\partial\xi^2},\frac{\partial^2\widetilde{\mathbf{y}}}{\partial\eta^2}\right),\tag{2.14}$$

and the residual error function for $\widehat{\mathbf{g}}$, $\mathbf{e}_g$,

$$\mathbf{e}_g=\widehat{\mathbf{g}}\left(\widetilde{\mathbf{y}},\frac{\partial\widetilde{\mathbf{y}}}{\partial\xi},\frac{\partial\widetilde{\mathbf{y}}}{\partial\eta}\right),\tag{2.15}$$

where $\widetilde{\mathbf{y}} = [\widetilde{y}^1(\xi,\eta),...,\widetilde{y}^6(\xi,\eta)]^T$. We now integrate the absolute value of each component of both the residual error vector function $\mathbf{e}_f$ over the domain Ω, and the residual error vector function $\mathbf{e}_g$ over the boundary S, multiply each component by their respective weights and add them together to obtain a total residual error, e, *i.e.*

$$e = \sum_{q=1}^{4} \omega_f^q \int_\Omega \sqrt{e_f^q e_f^q} d\Omega + \sum_{q=1}^{8} \omega_g^q \int_S \sqrt{e_g^q e_g^q} dS, \tag{2.16}$$

where e_f^q, $q = 1,...,4$, are the components of $\mathbf{e}_f$, and e_g^q, $q = 1,...,8$, are the components of $\mathbf{e}_g$. The approximation coefficients a_i^q in Eq. (2.13) are chosen in order to minimize e in Eq. (2.16). The ω_f^q and ω_g^q in Eq. (2.16) are constant weights which are chosen empirically to enhance convergence to a global minimum for e. A method for choosing the weights which yield an optimal convergence to a global minimum is something which has not been considered. The problem of minimizing e is a multi-variable minimization problem which is solved using a standard Newton method. The IMSL routine, DUMINF is employed to minimize e in Eq. (2.16) for the current work.

CHAPTER 3

KARHUNEN-LOÈVE GALERKIN LINEAR HEAT TRANSFER OPTIMIZATION PROBLEM

In this chapter we present a two-dimensional, linear heat conduction equation for which a KL Galerkin model will be developed and the accuracy and efficiency of the model evaluated compared to a pseudospectral method and a second order finite difference method. Two different boundary conditions will be employed. One boundary condition corresponds to a separation of variables series solution with only three terms and the other with an infinite number of terms. After presentation of the efficiency results, a single variable design problem will be solved using both the KL Galerkin model and the pseudospectral solver.

3.1 Problem Description

The two-dimensional unsteady linear heat conduction equation defined over the domain $\Omega : \{\xi \in [0,1], \eta \in [0,1]\}$ in dimensionless form is

$$\frac{\partial T}{\partial \tau} = \frac{\partial^2 T}{\partial \xi^2} + \Gamma^2 \frac{\partial^2 T}{\partial \eta^2}, \tag{3.1}$$

where T is temperature, ξ and η are the two-dimensional spatial coordinates, τ is time and Γ is the aspect ratio of a plate as seen in Figure 3.1. The dimensional form for temperature, T^*, spatial coordinates ξ^* and η^*, and time τ^* is recovered

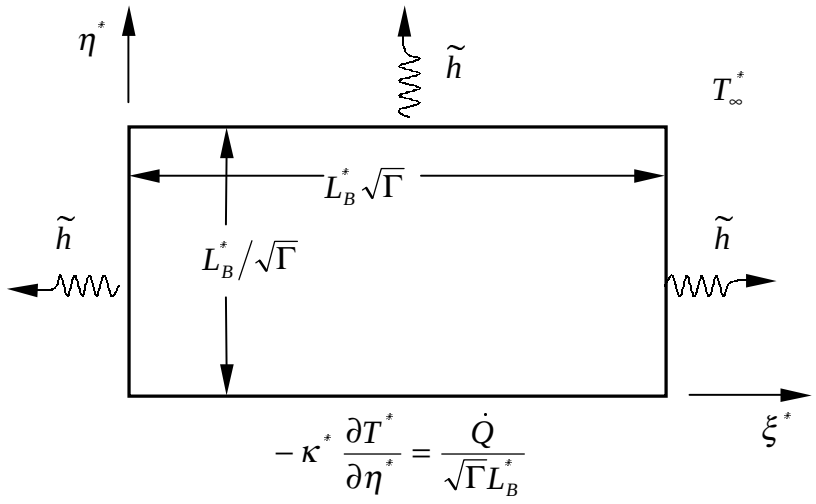

Figure 3.1. Schematic of heat conduction problem.

from the following equations

$$T^* = T\frac{\dot{Q}}{\kappa^*} + T_\infty^*, \quad \xi^* = \xi\sqrt{\Gamma}L_B^*, \quad \eta^* = \eta\frac{L_B^*}{\sqrt{\Gamma}}, \quad \tau^* = \tau\frac{\Gamma L_B^{*2}}{\alpha^*}, \tag{3.2}$$

where dimensional quantities are denoted by $*$, T_∞^* is the temperature of the surrounding medium, κ^* is the thermal conductivity of the solid, L_B^* is a characteristic length, $\dot{Q}$ is a constant heat flow rate per unit depth, and α^* is the coefficient of thermal diffusivity. The first set of boundary conditions which we will consider are a constant temperature gradient on the lower wall,

$$\frac{\partial T}{\partial \eta}(\xi, 0, \tau) = -\frac{1}{\Gamma}, \tag{3.3}$$

and convection on the other three sides,

$$\frac{\partial T}{\partial \eta}(\xi, 1, \tau) = -\frac{\beta}{\sqrt{\Gamma}}T\left(\xi, 1, \tau\right), \tag{3.4}$$

$$\frac{\partial T}{\partial \xi}(0, \eta, \tau) = \beta\sqrt{\Gamma}T(0, \eta, \tau), \tag{3.5}$$

$$\frac{\partial T}{\partial \xi}(1, \eta, \tau) = -\beta\sqrt{\Gamma}T(1, \eta, \tau), \tag{3.6}$$

where the Biot number, β defined as, $\beta = \widetilde{h}L_B^*/\kappa^*$, is set equal to unity for this problem and $\widetilde{h}$ is the coefficient of convection for the surrounding medium. Eq. (3.3) is consistent with Fourier's law of heat conduction,

$$\mathbf{q}^* = -\kappa^* \nabla T^*, \tag{3.7}$$

for a constant heat flow rate per unit depth, $\dot{Q}$, through the boundary, $\eta^* = 0$, where

$$\dot{Q} = \int_0^{\sqrt{\Gamma}L_B^*} q^*\left(\xi^*, 0, \tau^*\right) d\xi^* = q^*\left(\xi^*, 0, \tau^*\right)\sqrt{\Gamma}L_B^*, \tag{3.8}$$

$\mathbf{q}^*$ is the heat flux vector, and q^* is the component of $\mathbf{q}^*$ in the η direction, *i.e.*

$$q^* = -\kappa^* \frac{\partial T^*}{\partial \eta^*}. \tag{3.9}$$

Substituting the expression for $q^*\left(\xi^*, 0, \tau^*\right)$ from Eq. (3.8) , *i.e.* $q^*\left(\xi^*, 0, \tau^*\right) = \frac{\dot{Q}}{\sqrt{\Gamma}L_B^*}$, into Eq. (3.9) evaluated at $\eta^* = 0$ yields the following expression,

$$\left.\frac{\partial T^*}{\partial \eta^*}\right|_{(\xi^*, 0, \tau^*)} = -\frac{\dot{Q}}{\sqrt{\Gamma}\kappa^* L_B^*}, \tag{3.10}$$

which is the dimensional form of the boundary condition in Eq. (3.3) . For the second set of boundary conditions, we replace Eq. (3.3) with the following

$$\frac{\partial T}{\partial \eta}(\xi, 0, \tau) = -\frac{1}{\Gamma}\sum_{i=1}^{3}\left(\frac{\beta\sqrt{\Gamma}}{\sigma_i}\sin\sigma_i\xi + \cos\sigma_i\xi\right), \tag{3.11}$$

where the σ_i, $i = 1, 2, 3$, are eigenvalues of an appropriate Sturm-Liouville operator and can be found in Appendix C. There exists a separation of variables solution for the heat conduction problem with both the boundary conditions Eq. (3.3) and Eq. (3.11); this solution is also detailed in Appendix C. The difference in the separation of variables solution between the two types of boundary conditions is that the solution to the heat conduction problem with the boundary condition in Eq. (3.3) requires an infinite number of terms in the series expansion of the solution while the boundary condition in Eq. (3.11) requires only three terms in the series

expansion of the solution. For this reason, the boundary condition in Eq. (3.11) will be referred to as a finite mode boundary condition. In the series expansion of the solution to the first boundary condition, Eq. (3.3) , 750 terms are retained which was found to yield a maximum local error $L_\infty[\Omega]$ in $T(\xi, \eta, \tau \to \infty)$ of 1×10^{-9}.

Although the unsteady formulation of the heat conduction problem has been posed, we are only interested in the steady state temperature distribution. Solving the unsteady form of the heat conduction problem to a steady state is simpler than solving the steady form for both the pseudospectral and KL Galerkin methods. Since the steady state solution to the linear problem, Eqs. $(3.3 - 3.6)$ is unique and therefore independent of the initial conditions, we choose the following initial conditions

$$T(\xi, \eta, 0) = 1. \tag{3.12}$$

The optimization problem is to maximize the average temperature, $T_{avg}(\Gamma)$ over the domain as a function of the domain aspect ratio, Γ, *i.e.*

$$T_{avg}(\Gamma) = \int_0^1 \int_0^1 T(\xi, \eta, \tau \to \infty; \Gamma) d\xi d\eta, \tag{3.13}$$

where the boundary condition in Eq. (3.3) is used. The second boundary condition in Eq. (3.11) has been introduced for the efficiency tests only and is not employed in the optimal design problem.

3.2 Pseudospectral and Finite Difference Solutions

The first step in developing a KL Galerkin model of the heat conduction problem is the generation of a set of steady state characteristic solutions. The steady state solutions are found by integrating the unsteady equations to a long time steady state, where there is no further improvement in the error as measured against the steady state separation of variables solution. A pseudospectral method using global

Lagrange interpolating polynomials is employed. Since this problem is linear, instead of a pseudospectral method, we could have implemented another method of weighted residuals such as a Galerkin method. However, in preparation for the subsequent blunt body problem, a solver with the capability of easily handling nonlinearities is desired, so that the pseudospectral method is chosen. The temperature is approximated in terms of global Lagrange interpolating polynomials defined on the mesh ξ_n, $n = 0, ..., N$, η_m, $m = 0, ..., M$, *i.e.*

$$T(\xi, \eta, \tau) \approx I_{NM} T(\xi, \eta, \tau) = \sum_{i=0}^{N} \sum_{j=0}^{M} T(\xi_i, \eta_j, \tau) L_i^{(N)}(\xi) L_j^{(M)}(\eta), \tag{3.14}$$

where we chose the following Chebyshev distribution of nodes,

$$\begin{aligned} \xi_i &= \frac{1}{2}\left[1 - \cos\left(\frac{\pi}{N} i\right)\right], \quad i = 0, ..., N, \\ \eta_j &= \frac{1}{2}\left[1 - \cos\left(\frac{\pi}{M} j\right)\right], \quad j = 0, ..., M, \end{aligned} \tag{3.15}$$

which correspond to the location of the zeroes of a Chebyshev polynomial of order N and M respectively achieves a maximum. This choice of nodes is not unique and is made because global Lagrange polynomial approximations of general nonperiodic functions defined on this grid were found in Appendix B to yield a more uniform and overall lower error than a uniform grid. A 9×9 grid with the distribution defined by Eq. (3.15) is shown in Figure 3.2. The Lagrange interpolating polynomials are defined as

$$\begin{aligned} L_n^{(N)}(\xi) &= \frac{\prod_{l=0, l\neq n}^{N} (\xi - \xi_l)}{\prod_{l=0, l\neq n}^{N} (\xi_n - \xi_l)}, \quad n = 0, ..., N, \\ L_m^{(M)}(\eta) &= \frac{\prod_{l=0, l\neq m}^{M} (\eta - \eta_l)}{\prod_{l=0, l\neq m}^{M} (\eta_m - \eta_l)}, \quad m = 0, ..., M. \end{aligned} \tag{3.16}$$

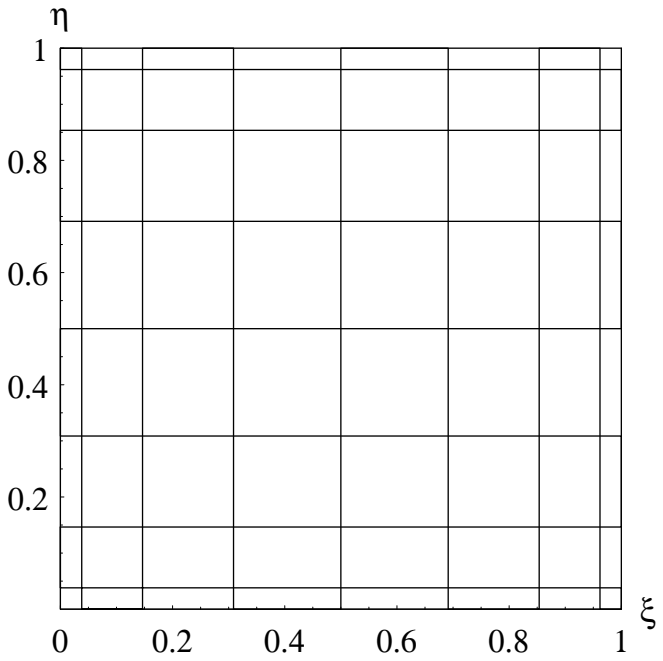

Figure 3.2. 9×9 computational grid for the pseudospectral solution to the heat conduction problem.

It is easily shown that the Lagrange interpolating polynomials, $L_n^{(N)}(\xi)$, and $L_m^{(M)}(\eta)$ have the values of unity at $\xi = \xi_n$ and $\eta = \eta_m$ and zero at the other collocation points, *i.e.*

$$L_n^{(N)}(\xi_i) = \delta_{ni} = \begin{cases} 0 & \text{if } n \neq i, \\ 1 & \text{if } n = i. \end{cases} \quad ; \quad L_m^{(M)}(\eta_j) = \delta_{mj} = \begin{cases} 0 & \text{if } m \neq j, \\ 1 & \text{if } m = j. \end{cases} \quad . \tag{3.17}$$

The first derivatives in Eqs. $(3.3 - 3.6)$, and the second derivatives in Eq. (3.1) are approximated by taking derivatives of Eq. (3.14). We choose to evaluate the derivatives on the grid, (ξ_i, η_j), chosen to be the same grid as that used to define the interpolating polynomial, *i.e.* $(\xi_i, \eta_j) \equiv (\xi_n, \eta_m)$, although this choice is not unique. Differentiating Eq. (3.14), and making use of Eq. (3.17), we have the

following approximation for the first derivatives

$$\left.\frac{\partial T}{\partial \xi}\right|_{(\xi_i,\eta_j)} \approx \sum_{n=0}^{N} T(\xi_n,\eta_j,\tau)\frac{dL_n}{d\xi}(\xi_i), \tag{3.18}$$
$$\left.\frac{\partial T}{\partial \eta}\right|_{(\xi_i,\eta_j)} \approx \sum_{m=0}^{M} T(\xi_i,\eta_m,\tau)\frac{dL_m}{d\eta}(\eta_j).$$

and for the second derivatives,

$$\left.\frac{\partial^2 T}{\partial \xi^2}\right|_{(\xi_i,\eta_j)} \approx \sum_{n=0}^{N} T(\xi_n,\eta_j,\tau)\frac{d^2L_n}{d\xi^2}(\xi_i), \tag{3.19}$$
$$\left.\frac{\partial^2 T}{\partial \eta^2}\right|_{(\xi_i,\eta_j)} \approx \sum_{m=0}^{M} T(\xi_i,\eta_m,\tau)\frac{d^2L_m}{d\eta^2}(\eta_j).$$

The terms $\frac{dL_n}{d\xi}(\xi_i)$ and $\frac{dL_m}{d\eta}(\eta_j)$ in Eq. (3.18) and the terms $\frac{d^2L_n}{d\xi^2}(\xi_i)$ and $\frac{d^2L_m}{d\eta^2}(\eta_j)$ in Eq. (3.19) are evaluated efficiently for an arbitrary grid using an algorithm developed by Fornberg [43]. The points which both define the Lagrange interpolating polynomials and at which derivatives are evaluated are chosen according to Eq. (3.15).

The boundary conditions in Eqs. $(3.3-3.6)$ are approximated on the mesh ξ_n, $n=0,...,N$, η_m, $m=0,...,M$, by employing Eq. (3.18) as follows

$$\frac{\partial T}{\partial \eta}(\xi_n,0,\tau) \approx \sum_{j=0}^{M} T(\xi_n,\eta_j,\tau)\frac{dL_j^{(M)}(0)}{d\eta} = -\frac{1}{\Gamma}, \quad n=0,...,N, \tag{3.20}$$

$$\frac{\partial T}{\partial \eta}(\xi_n,1,\tau) \approx \sum_{j=0}^{M} T(\xi_n,\eta_j,\tau)\frac{dL_j^{(M)}(1)}{d\eta} = -\frac{\beta}{\sqrt{\Gamma}}T\left(\xi_n,1\right), \quad n=0,...,N, \tag{3.21}$$

$$\frac{\partial T}{\partial \xi}(0,\eta_m,\tau) \approx \sum_{i=0}^{N} T(\xi_i,\eta_m,\tau)\frac{dL_i^{(N)}(0)}{d\xi} = \beta\sqrt{\Gamma}T(0,\eta_m), \quad m=0,...,M, \tag{3.22}$$

$$\frac{\partial T}{\partial \xi}(1,\eta_m,\tau) \approx \sum_{i=0}^{N} T(\xi_i,\eta_m,\tau)\frac{dL_i^{(N)}(1)}{d\xi} = -\beta\sqrt{\Gamma}T(1,\eta_m), \quad m=0,...,M. \tag{3.23}$$

From Eqs. $(3.20-3.23)$ we derive the following explicit expressions for the values

of $T(\xi,\eta,\tau)$ at the boundaries

$$T(\xi_n,0,\tau) = -\left(\frac{dL_0^{(M)}(1)}{d\eta}\right)^{-1}\left(T(\xi_n,1,\tau)\left(\frac{dL_M^{(M)}(1)}{d\eta}+\frac{\beta}{\sqrt{\Gamma}}\right)\right. \tag{3.24}$$
$$\left.+\sum_{j=1}^{M-1}T(\xi_n,\eta_j,\tau)\frac{dL_j^{(M)}(1)}{d\eta}\right),$$
$$n=0,...,N,$$

$$T(\xi_n,1,\tau) = \left(\frac{dL_M^{(M)}(0)}{d\eta}-\frac{dL_0^{(M)}(0)}{d\eta}\left(\frac{dL_0^{(M)}(1)}{d\eta}\right)^{-1}\left(\frac{dL_M^{(M)}(1)}{d\eta}+\frac{\beta}{\sqrt{\Gamma}}\right)\right)^{-1} \tag{3.25}$$
$$\left(\frac{dL_0^{(M)}(0)}{d\eta}\left(\frac{dL_0^{(M)}(1)}{d\eta}\right)^{-1}\sum_{j=1}^{M-1}T(\xi_n,\eta_j,\tau)\frac{dL_j^{(M)}(1)}{d\eta}\right.$$
$$\left.-\frac{1}{\Gamma}-\sum_{j=1}^{M-1}T(\xi_n,\eta_j,\tau)\frac{dL_j^{(M)}(0)}{d\eta}\right),$$
$$n=0,...,N,$$

$$T(0,\eta_m,\tau) = \left(\frac{dL_0^{(N)}(0)}{d\xi}-\beta\sqrt{\Gamma}-\left(\frac{dL_N^{(N)}(1)}{d\xi}+\beta\sqrt{\Gamma}\right)^{-1}\frac{dL_N^{(N)}(0)}{d\xi}\frac{dL_0^{(N)}(1)}{d\xi}\right)^{-1} \tag{3.26}$$
$$\frac{dL_N^{(N)}(0)}{d\xi}\left(\frac{dL_N^{(N)}(1)}{d\xi}+\beta\sqrt{\Gamma}\right)^{-1}\left(\sum_{i=1}^{N-1}T(\xi_i,\eta_m,\tau)\frac{dL_i^{(N)}(1)}{d\xi}\right.$$
$$\left.-\sum_{i=1}^{N-1}T(\xi_i,\eta_m,\tau)\frac{dL_i^{(N)}(0)}{d\xi}\right),$$
$$m=1,...,M-1,$$

$$T(1,\eta_m,\tau) = -\left(\frac{dL_N^{(N)}(1)}{d\xi}+\beta\sqrt{\Gamma}\right)^{-1}\sum_{i=0}^{N-1}T(\xi_i,\eta_m,\tau)\frac{dL_i^{(N)}(1)}{d\xi}, \tag{3.27}$$
$$m=1,...,M-1.$$

Employing Eqs. $(3.24 - 3.27)$ for $T(\xi, \eta, \tau)$ at the boundaries, the discretized form of Eq. (3.1) can be expressed as a system of ODEs of the following form

$$\left.\frac{dT}{d\tau}\right|_{(\xi_n, \eta_m, \tau)} = F\left(T\left(\xi_n, \eta_m, \tau\right); \Gamma\right), \quad \begin{matrix} n = 1, ..., N-1, \\ m = 1, ..., M-1, \end{matrix} \tag{3.28}$$

which is integrated in time to steady state using a second order Runge-Kutta method.

A second order central finite difference method was also implemented in order to compare the efficiencies of both the pseudospectral and KL Galerkin methods with a finite difference method. For the finite difference method, the boundary conditions are approximated by a second order accurate one-sided differencing scheme which permits explicit expressions for $T(\xi, \eta, \tau)$ to be obtained at the boundaries as a function of $T(\xi, \eta, \tau)$ in the interior of the domain. A system of (ODEs) of the same form as Eq. (3.28) is obtained and these equations are then integrated in time to steady state.

The temperature distribution for the separation of variables solution at $\Gamma = 1.5$ is shown in Figure 3.3 for the boundary condition Eq. (3.3). Figure 3.4 is the temperature distribution from the separation of variables solution for the boundary condition in Eq. (3.11), where the exact separation of variables solution contains three terms in the expansion. We see in both Figures 3.3 and 3.4 that the temperature is highest along the boundary $\eta = 0$ where the heat source is located and diminishes as $\eta = 1$ is approached due to heat loss via convection through the remaining boundaries. The temperature distribution in Figure 3.4 has a noticeable peak in the temperature near the corner $\{\xi = 0, \eta = 0\}$ which is not present in Figure 3.3 due to the finite mode boundary condition employed in Figure 3.4.

In order to verify the algorithm, a series of grid convergence tests were performed showing the $L_\infty[\Omega]$ error in $T(\xi, \eta, \tau \to \infty)$ measured against a separation of variables solution to the heat conduction problem as a function of number of

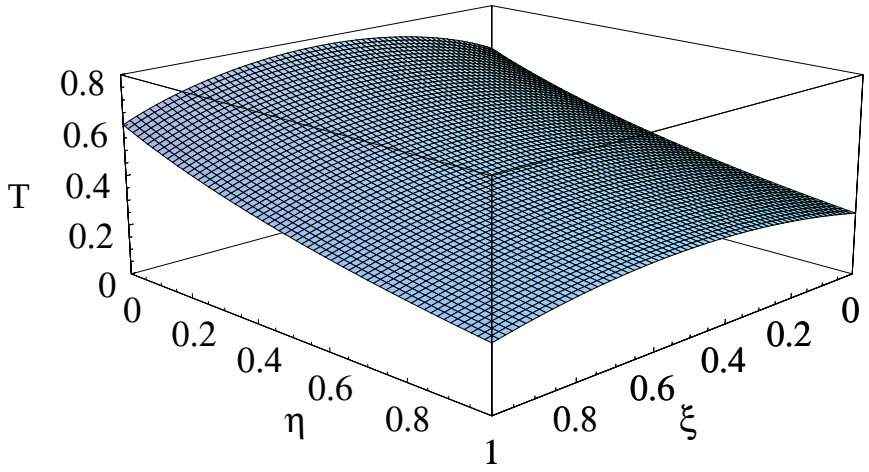

Figure 3.3. Sample temperature distribution for the infinite mode boundary condition (BC1) and $\Gamma = 1.5$.

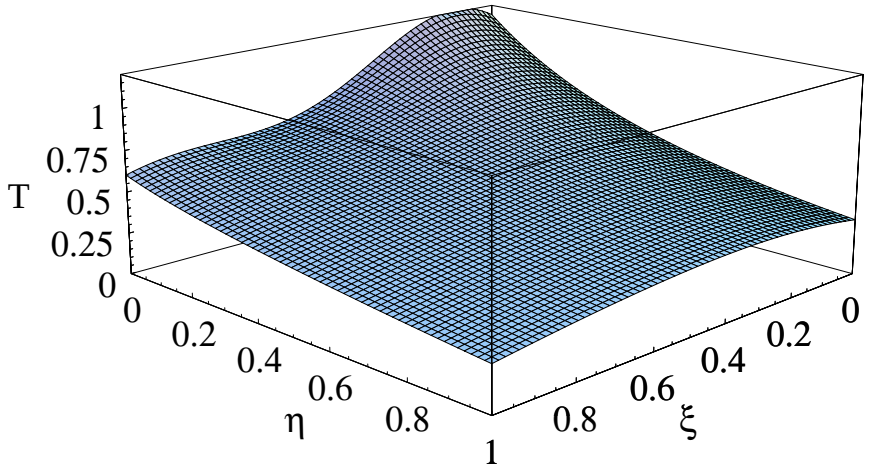

Figure 3.4. Sample temperature distribution for the finite mode boundary condition (BC2) and $\Gamma = 1.5$.

nodes. Figure 3.5 shows the grid convergence of the $L_\infty[\Omega]$ error in $T(\xi, \eta, \tau \to \infty)$ for both the pseudspectral solver and the finite difference solver with the infinite mode boundary condition, Eq. (3.3) denoted as BC1, and the finite mode boundary condition, Eq. (3.11) denoted as BC2. The convergence rate of the finite difference method for BC2 is seen to be significantly worse than that of the pseudospectral method for the the same boundary condition; however, the convergence rate of the finite difference method for BC1 is only slightly lower than that of the pseudospectral method for the same boundary condition. The convergence rate of the pseudospectral method is seen to be more sensitive to changes in the boundary conditions than the finite difference method for the two different boundary conditions considered here. Even though the convergence rate of the pseudospectral method is only slightly higher than the finite difference method for BC1, the magnitude of the error is one to two orders of magnitude lower for the same number of nodes than the finite difference method.

3.3 Karhunen-Loève Modes

The second step in developing a KL Galerkin model of the heat conduction problem is generating a set of KL modes from a set of characteristic solutions. For the current work, ten characteristic solutions are taken to be pseudospectral solutions to the heat conduction problem for the following ten values of aspect ratio $\Gamma = \{0.75, 1.0, 1.25, 1.5, 1.75, 2.0, 2.25, 2.5, 2.75, 3.0\}$. The ten KL eigenmodes generated from 35×25 grid pseudospectral for the heat conduction problem with the boundary condition in Eq. (3.3) are shown in Figure 3.6. The associated eigenvalues, λ, are shown in Figure 3.7. Other choices for the number of snapshots, values of Γ, and the grid resolution for the snapshots are possible and impact the accuracy in the resulting KL model.

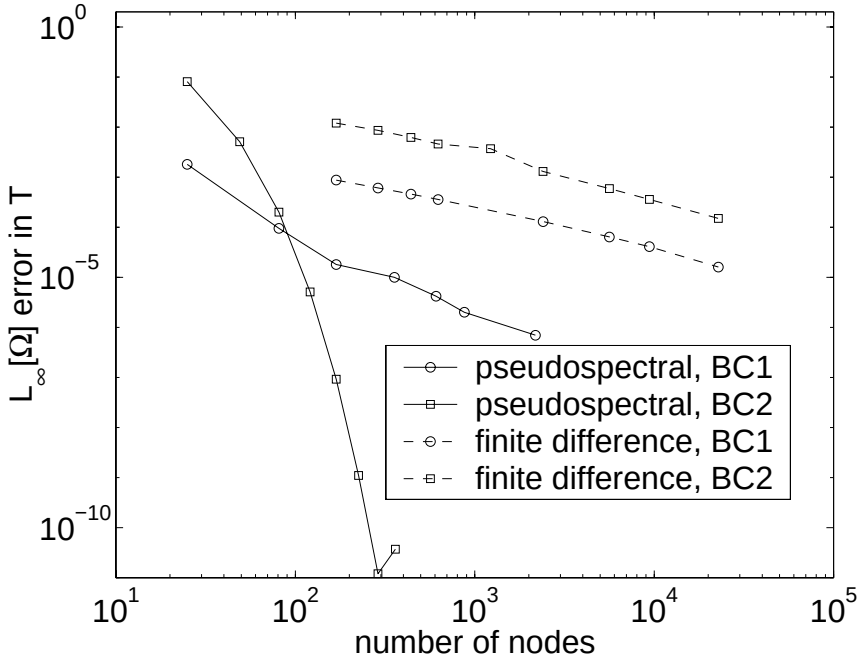

Figure 3.5. Grid convergence $L_\infty[\Omega]$ error in $T(\xi, \eta, \tau \to \infty)$ measured against a separation of variables solution for $\Gamma = 1.5$.

It can be seen in Figure 3.6, that the first two modes are most structurally similar to the temperature distribution in Figure 3.3 and the subsequent modes become increasingly structurally complex as the mode number increases. The magnitude of the eigenvalues in Figure 3.7 is seen to decrease rapidly with increasing mode number, until the roundoff precision of the computer is reached at the eighth mode.

3.4 Karhunen-Loève Galerkin Model

The final step to develop a KL Galerkin model is to employ the Galerkin method of weighted residuals with the KL modes from the previous step as the basis functions. The temperature distribution is approximated as a linear combination of the KL modes,

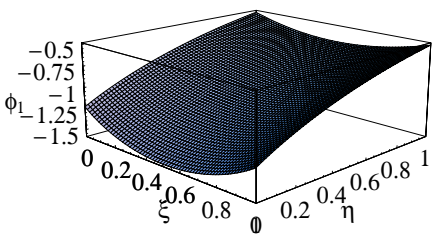

(a) $\lambda_1 = 0.225$

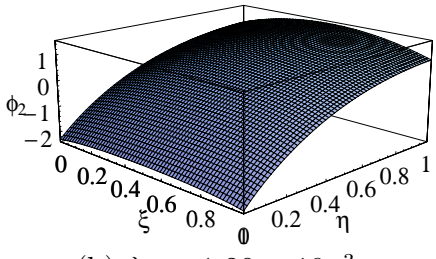

(b) $\lambda_2 = 1.29 \times 10^{-3}$

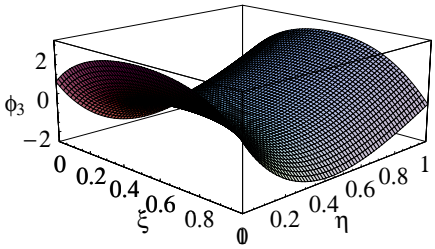

(c) $\lambda_3 = 2.7 \times 10^{-6}$

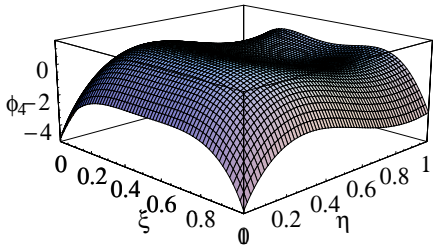

(d) $\lambda_4 = 1.19 \times 10^{-8}$

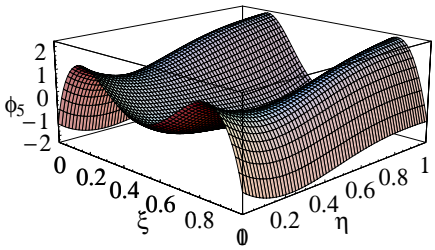

(e) $\lambda_5 = 2.8 \times 10^{-10}$

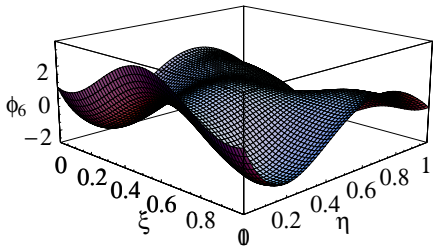

(f) $\lambda_6 = 2.4 \times 10^{-12}$

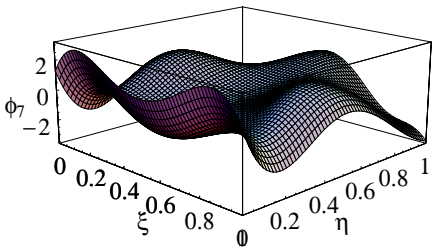

(g) $\lambda_7 = 1.0 \times 10^{-14}$

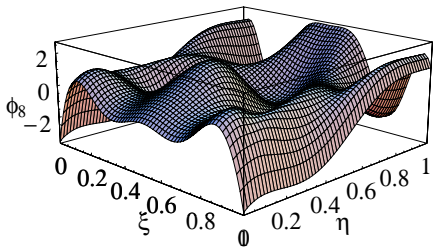

(h) $\lambda_8 = 5.0 \times 10^{-17}$

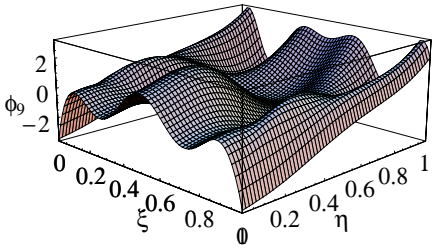

(i) $\lambda_9 = 2.5 \times 10^{-17}$

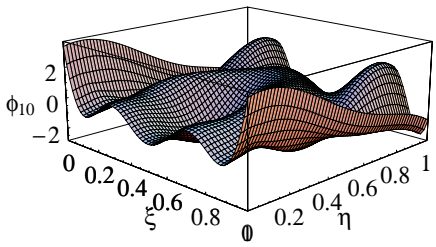

(j) $\lambda_{10} = 1.4 \times 10^{-17}$

Figure 3.6. Ten KL eigenmodes with associated eigenvalues built from ten uniform samples for $\Gamma \in [3/4, 3]$ on a 35×25 grid.

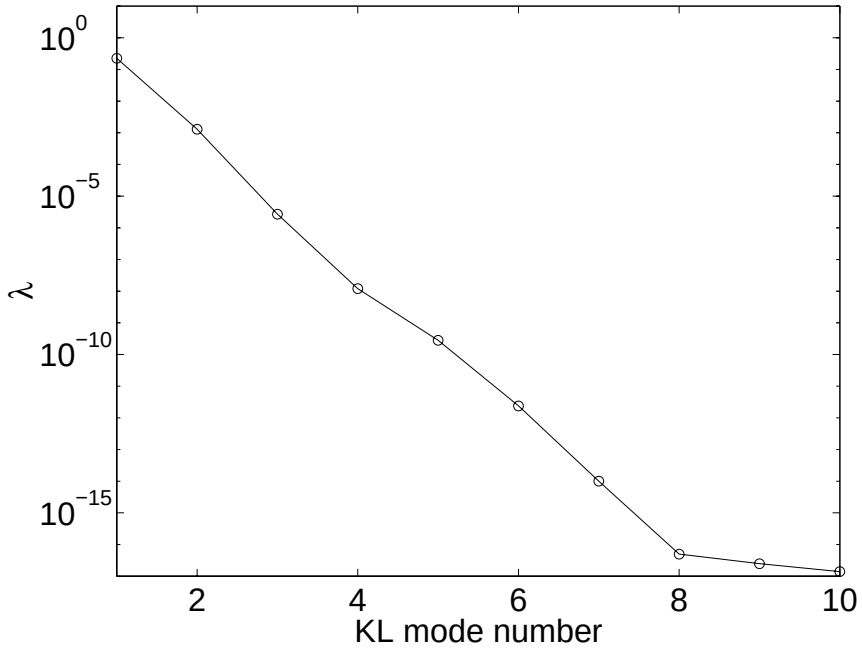

Figure 3.7. Eigenvalues, λ, for the KL model built from a uniform sampling of ten characteristic solutions $\Gamma \in [3/4, 3]$ on a 35×25 grid.

$$T(\xi,\eta,\tau) \approx \widetilde{T}(\xi,\eta,\tau) = \sum_{k=1}^{L} a_k(\tau)\varphi_k(\xi,\eta), \tag{3.29}$$

where $a_k(\tau)$, $k = 1, ..., K$, are the expansion coefficients. Substituting the approximation for $T(\xi,\eta,\tau)$ from Eq. (3.29) into Eq. (3.1) yields the following error function

$$e(\xi,\eta,\tau) = \frac{\partial \widetilde{T}}{\partial \tau} - \frac{\partial^2 \widetilde{T}}{\partial \xi^2} - \Gamma^2 \frac{\partial^2 \widetilde{T}}{\partial \eta^2}. \tag{3.30}$$

In the Galerkin method of weighted residuals, it is enforced that $e(\xi,\eta,\tau)$ be orthogonal to each of the basis functions, $\varphi_l(\xi,\eta)$, $l = 1, ..., L$, where L is the number of modes in the expansion.

$$\int_0^1 \int_0^1 e(\xi,\eta,\tau)\varphi_l(\xi,\eta)d\xi d\eta = 0, \quad l = 1, ..., L. \tag{3.31}$$

Substituting Eq. (3.30) into Eq. (3.31) yields

$$\begin{aligned} &\int_0^1 \int_0^1 \frac{\partial T}{\partial \tau}(\xi,\eta,\tau)\varphi_l(\xi,\eta)d\xi d\eta, \\ &= \int_0^1 \int_0^1 \frac{\partial^2 T}{\partial \xi^2}(\xi,\eta,\tau)\varphi_l(\xi,\eta)d\xi d\eta + \Gamma^2 \int_0^1 \int_0^1 \frac{\partial^2 T}{\partial \eta^2}(\xi,\eta,\tau)\varphi_l(\xi,\eta)d\xi d\eta, \\ &l = 1, ..., L. \end{aligned} \tag{3.32}$$

The two terms on the right-hand side of Eq. (3.32) can be expanded by integrating by parts, as in Appendix D, which yields the following

$$\begin{aligned} &\int_0^1 \int_0^1 \frac{\partial^2 T}{\partial \xi^2}(\xi,\eta,\tau)\varphi_l(\xi,\eta)d\xi d\eta \\ &= \int_0^1 \left(\frac{\partial T}{\partial \xi}(1,\eta)\,\varphi_l(1,\eta) - \frac{\partial T}{\partial \xi}(0,\eta)\,\varphi_l(0,\eta) \right) d\eta - \int_0^1 \int_0^1 \frac{\partial T}{\partial \xi}(\xi,\eta)\,\frac{\partial \varphi_l}{\partial \xi}(\xi,\eta)\,d\xi d\eta, \end{aligned} \tag{3.33}$$

$$\begin{aligned} &\int_0^1 \int_0^1 \frac{\partial^2 T}{\partial \eta^2}(\xi,\eta,\tau)\varphi_l(\xi,\eta)d\xi d\eta \\ &= \int_0^1 \left(\frac{\partial T}{\partial \eta}(\xi,1)\,\varphi_l(\xi,1) - \frac{\partial T}{\partial \eta}(\xi,0)\,\varphi_l(\xi,0) \right) d\xi - \int_0^1 \int_0^1 \frac{\partial T}{\partial \eta}(\xi,\eta)\,\frac{\partial \varphi_l}{\partial \eta}(\xi,\eta)\,d\xi d\eta. \end{aligned} \tag{3.34}$$

Making use of the boundary conditions from Eqs. $(3.3-3.6)$ or Eqs. (3.11) and $(3.4-3.6)$, Eqs. (3.33) and (3.34) can be rewritten as follows:

$$\int_0^1 \int_0^1 \frac{\partial^2 T}{\partial \xi^2}(\xi,\eta,\tau)\varphi_l(\xi,\eta)d\xi d\eta \tag{3.35}$$
$$= -\sqrt{\Gamma}\beta \int_0^1 \left(T\left(1,\eta\right)\varphi_l\left(1,\eta\right) + T\left(0,\eta\right)\varphi_l\left(0,\eta\right)\right)d\eta - \int_0^1 \int_0^1 \frac{\partial T}{\partial \xi}\left(\xi,\eta\right)\frac{\partial \varphi_l}{\partial \xi}\left(\xi,\eta\right)d\xi d\eta,$$

$$\int_0^1 \int_0^1 \frac{\partial^2 T}{\partial \eta^2}(\xi,\eta,\tau)\varphi_l(\xi,\eta)dxdy \tag{3.36}$$
$$= -\int_0^1 \left(\frac{\beta}{\sqrt{\Gamma}}T\left(\xi,1\right)\varphi_l\left(\xi,1\right) - \frac{\psi\left(\xi\right)}{\Gamma}\varphi_l\left(\xi,0\right)\right)d\xi - \int_0^1 \int_0^1 \frac{\partial T}{\partial \eta}\left(\xi,\eta\right)\frac{\partial \varphi_l}{\partial \eta}\left(\xi,\eta\right)d\xi d\eta,$$

where $\psi\left(\xi\right) = 1$ if Eq. (3.3) is used or $\psi\left(\xi\right) = \sum_{i=1}^{3}\left(\frac{\beta\sqrt{\Gamma}}{\sigma_i}\sin\sigma_i\xi + \cos\sigma_i\xi\right)$ if Eq. (3.11) is used. Substituting the approximation for $T(\xi,\eta,\tau)$ from Eq. (3.29) into the left-hand side of Eq. (3.32) yields the following

$$\begin{aligned}
&\int_0^1 \int_0^1 \frac{\partial T}{\partial \tau}(\xi,\eta,\tau)\varphi_l(\xi,\eta)d\xi d\eta \qquad (3.37)\\
&= \sum_{k=1}^{L}\frac{d}{d\tau}(a_k(\tau))\int_0^1\int_0^1 \varphi_k(\xi,\eta)\varphi_l(\xi,\eta)d\xi d\eta\\
&= \frac{d}{d\tau}(a_l(\tau)), \quad l = 1,...,L,
\end{aligned}$$

where we have made use of the fact that the basis functions $\varphi_l(\xi,\eta)$, $l = 1,...,L$, are orthonormal. Finally, we have the following form for Eq. (3.32) after making use of Eqs. $(3.35-3.37)$,

$$\begin{aligned}
\frac{d}{d\tau}(a_l(\tau)) = &-\int_0^1\int_0^1\left(\frac{\partial T}{\partial \xi}\frac{\partial \varphi_l}{\partial \xi} + \Gamma^2\frac{\partial T}{\partial \eta}\frac{\partial \varphi_l}{\partial \eta}\right)d\xi d\eta \qquad (3.38)\\
&- \beta\sqrt{\Gamma}\int_0^1\left(T\left(1,\eta\right)\varphi_l\left(1,\eta\right) + T\left(0,\eta\right)\varphi_l\left(0,\eta\right)\right)d\eta\\
&- \beta\Gamma^{3/2}\int_0^1 T\left(\xi,1\right)\varphi_l\left(\xi,1\right)d\xi + \Gamma\int_0^1\psi\left(\xi\right)\varphi_l\left(\xi,0\right)d\xi\\
l = 1,...,L.&
\end{aligned}$$

Once the ordinary differential equations in Eq. (3.38) have been solved to steady-state, the temperature distribution is recovered from Eq. (3.29). The integrals in

Eq. (3.38) are approximated by employing Gauss-Legendre quadrature as described in Appendix E.

3.5 Results for Karhunen-Loève Model

3.5.1 Karhunen-Loève Mode Convergence for Ten Snapshot KL Model, $\Gamma \in [3/4, 3]$, Infinite Mode Boundary Condition (BC1)

Convergence of the $L_\infty[\Omega]$ error in $T(\xi, \eta)$ as a function of the number of KL modes is shown in Figure 3.8 for a KL model built from ten snapshots for the heat conduction problem with the boundary condition in Eq. (3.3). The ten snapshots are uniformly distributed over the range $\Gamma \in [3/4, 3]$. The snapshots are generated using the pseudospectral solver on both a 35×25 grid and a 21×17 grid and all the snapshots have nominally the same level of accuracy. The error in both the pseudospectral and KL Galerkin model is assessed by comparison with a high accuracy separation of variables solution. After the sixth mode for the 35×25 grid KL model and after the fifth mode for the 21×17 grid KL model there is no further improvement in the accuracy of the model, since the KL model accuracy has reached the level of error in the samples as shown by the dark lines in Figure 3.8.

3.5.2 Karhunen-Loève Mode Convergence for Ten Snapshot KL Model, $\Gamma \in [3/4, 3]$, Finite Mode Boundary Condition (BC2)

Convergence of the $L_\infty[\Omega]$ error in $T(\xi, \eta)$ as a function of the number of KL modes is shown in Figure 3.9 for a KL model built from ten snapshots for the heat conduction problem with the boundary condition in Eq. (3.11). The ten snapshots are uniformly distributed over the range $\Gamma \in [3/4, 3]$. The snapshots are generated using the pseudospectral solver on both a 15×15 grid and a 11×11 grid and once again the error in all of the snapshots is nominally the same. The error in both the

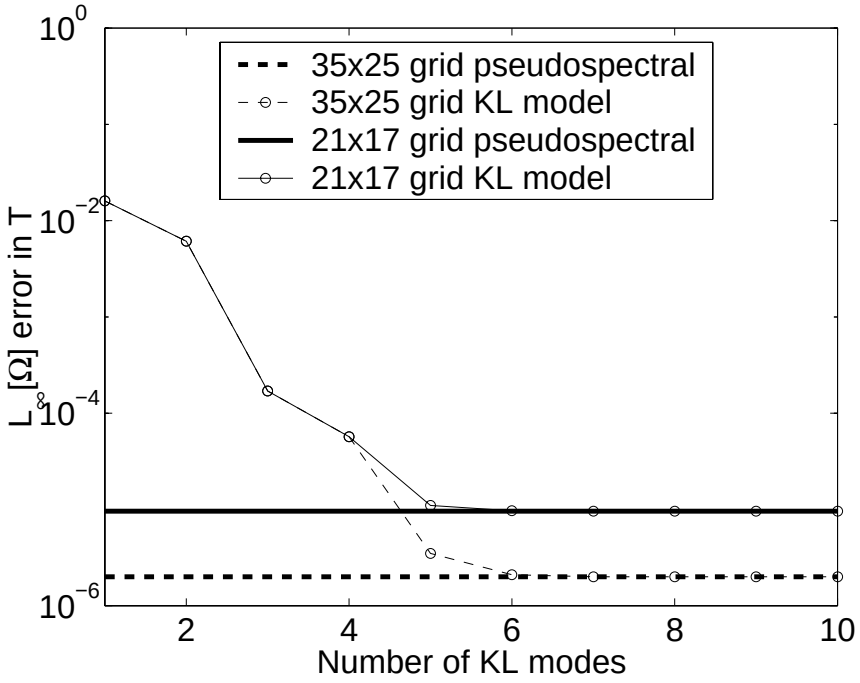

Figure 3.8. $L_\infty\,[\Omega]$ error in $T\,(\xi, \eta, \tau \to \infty)$ as a function of the number of KL modes for the infinite mode boundary condition (BC1), $\Gamma = 3/2$.

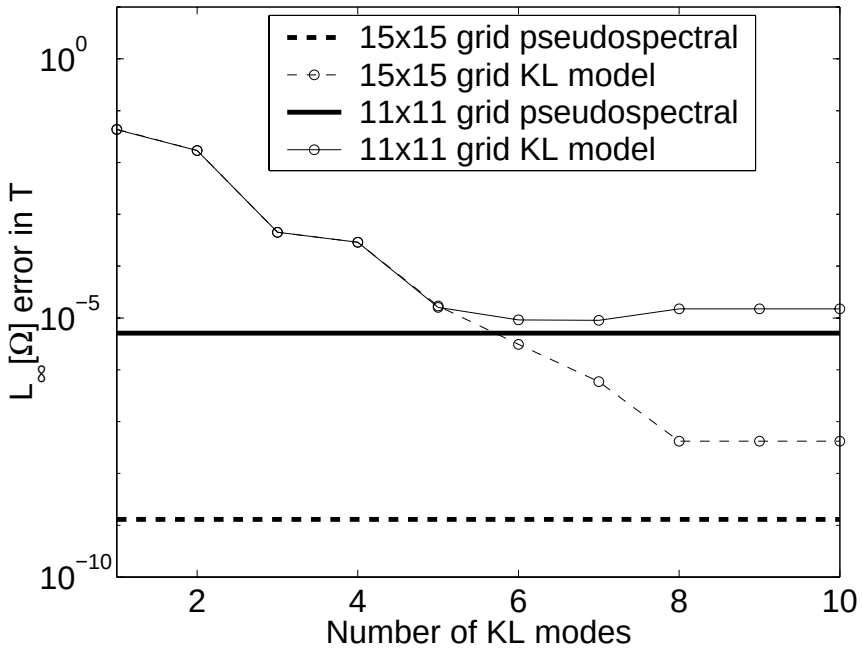

Figure 3.9. $L_\infty\,[\Omega]$ error in $T\,(\xi, \eta, \tau \to \infty)$ as a function of the number of KL modes for the finite mode boundary condition (BC2), $\Gamma = 3/2$.

pseudospectral and KL Galerkin model is assessed by comparison with the exact separation of variables solution. After the ninth mode for the 15×15 grid KL model and after the fifth mode for the 11×11 grid KL model there is no further improvement in the accuracy of the model. For the case of the 11×11 grid KL model the error reaches the level of the error in the snapshots; however, for the case of the 15×15 grid KL model the level of accuracy is about an order of magnitude higher than the level of accuracy in the snapshots as shown by the dark lines in Figure 3.9. It is not clear why the 15×15 grid KL model does not reach the level of accuracy in the snapshots and this something which requires further investigation.

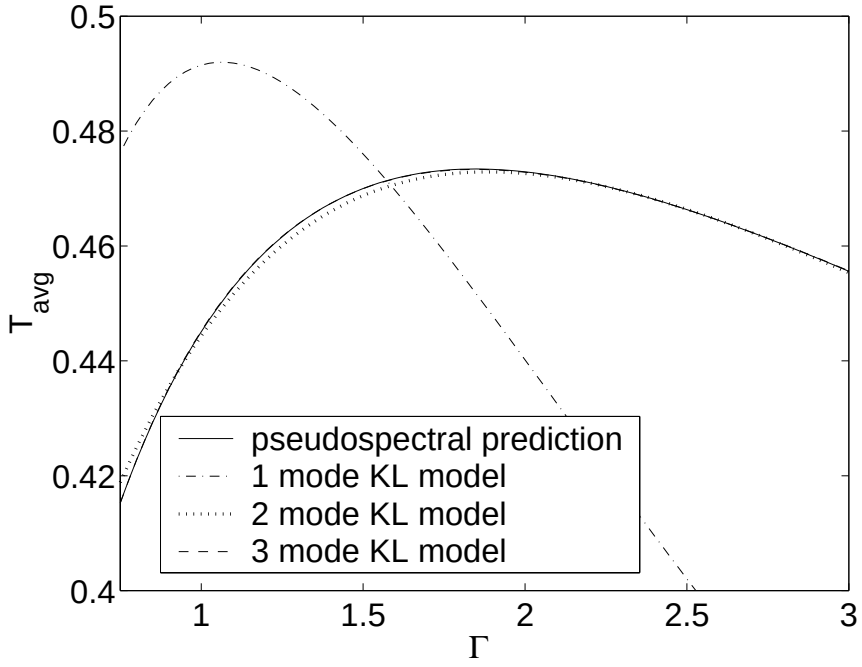

Figure 3.10. KL Galerkin model $T_{avg}(\Gamma)$ versus Γ built from 10 snapshots on a 35×25 grid.

3.5.3 Design Problem

In Figures 3.10 and 3.11, we show the plot of $T_{avg}(\Gamma)$ versus Γ for KL models using various numbers of KL modes compared to $T_{avg}(\Gamma)$ from a highly resolved pseudospectral solution. It is seen that for the KL model with one mode, the prediction is fairly poor, with the predicted value for the Γ yielding the maximum $T_{avg}(\Gamma)$ around 1.0 instead of the pseudospectral prediction for Γ at 1.85 . Including at least two KL modes in the model yields good agreement with the pseudospectral solution. As seen in Figure 3.11, the optimum value of Γ which yields the highest value of T_{avg} is $\Gamma = 1.85$, and the value of T_{avg} is 0.4734.

Now we develop a KL model taking only three snapshots at $\Gamma = 3/4$, $15/8$, and 3 from the pseudospectral solution on a 17×17 grid and compare the predictions for T_{avg} from the KL model to a quadratic polynomial fit of the three snapshots.

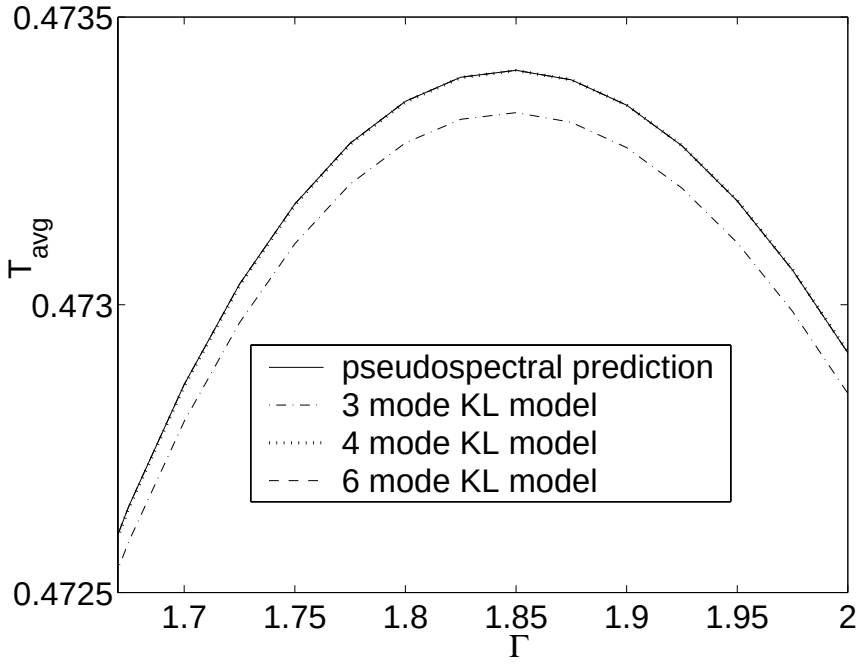

Figure 3.11. KL Galerkin model $T_{avg}(\Gamma)$ versus Γ magnified built from 10 snapshots on a 35×25 grid.

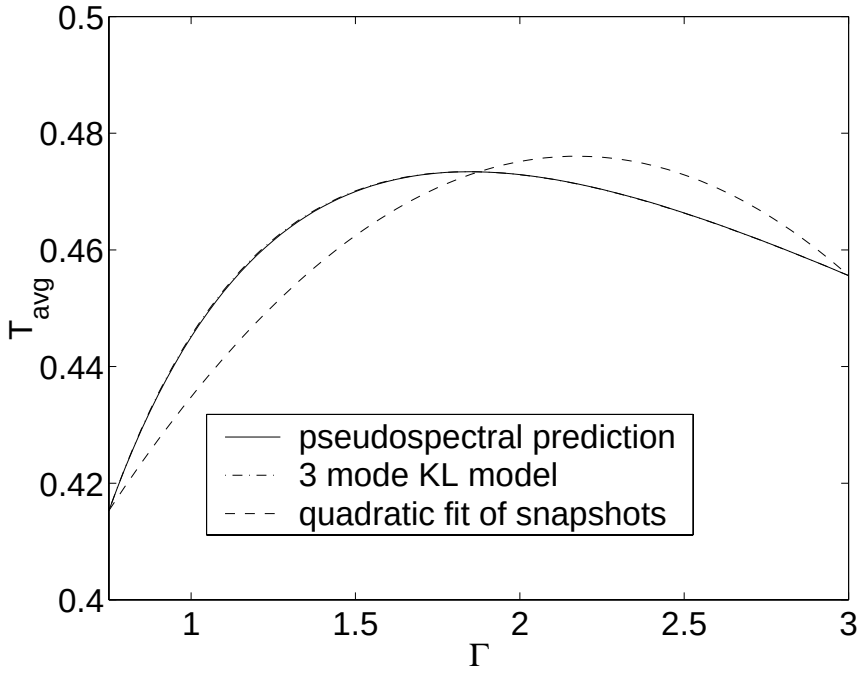

Figure 3.12. T_{avg} versus Γ for the KL model built from 3 snapshots on a 17×17 grid and a quadratic fit of T_{avg} from the same 3 snapshots.

The plot of T_{avg} versus Γ for the three mode KL model and the quadratic fit are shown in Figures 3.12 and 3.13 compared to T_{avg} from the pseudospectral solver on the same 17×17 grid. The equation for the quadratic fit of T_{avg} versus Γ is $T_{avg} = -0.029968574 + 0.130287875\Gamma + 0.334459475\Gamma^2$. It is seen that the dependence of T_{avg} on Γ is better approximated by the KL model than the quadratic fit.

3.5.4 Efficiency of Karhunen-Loève Galerkin Model

Figures 3.14 and 3.15 show the $L_\infty[\Omega]$ error in $T(\xi, \eta)$ versus CPU time in seconds for the KL Galerkin model, the pseudospectral solver, and the finite difference method for the boundary condition in Eq. (3.3) and the boundary condition in Eq. (3.11) respectively along with linear fits of the data points to make comparison easier. The various data points representing the pseudospectral and finite differ-

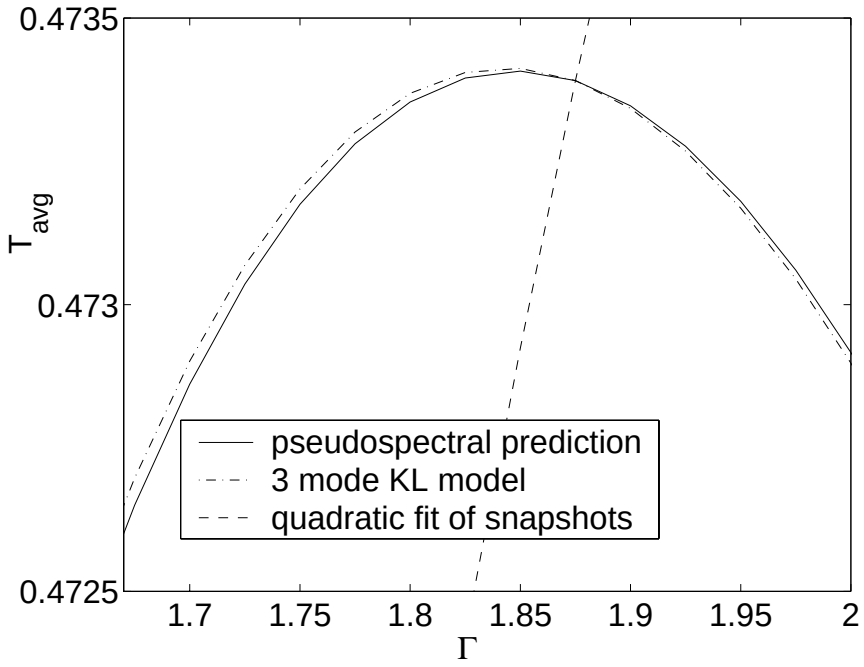

Figure 3.13. Magnification of T_{avg} versus Γ for the KL model built from 3 snapshots on a 17×17 grid and a quadratic fit of T_{avg} from the same 3 snapshots.

ence solutions are found by varying the number of grid points; finer grids yield more accurate results but also take longer to compute. The data points representing the KL model are all from KL models built with ten uniform snapshots over the range $\Gamma \in [3/4, 3]$ but with various levels of grid refinement and number of modes. The accuracy and computational cost for the KL model are functions of both the grid refinement in the snapshots and the number of modes used in the approximation; finer grid snapshots and more modes used in the KL model increase the accuracy of the predictions, but also the computational cost. In Figure 3.14 the slope of the line representing the error versus CPU time is significantly steeper for the KL model than for the pseudospectral method, so that the KL model requires nearly three orders of magnitude less CPU time at the lowest error level. In Figure 3.15 it is seen that the KL model and pseudospectral method predictions have roughly the same slope of error versus CPU time with the KL model at a slightly lower CPU time for the same level of accuracy. The finite difference method is significantly less efficient than either the pseudospectral or KL Galerkin methods. The efficiency results shown in this section do not take into consideration the computational cost of building the KL Galerkin model, although this is also an important consideration in deciding whether to use the KL method for a particular design problem.

Further understanding of the efficiency of the KL Galerkin method can be gained by examining the operation count per time step required in the computational algorithm as compared to the pseudospectral and finite difference methods. For the two-dimensional problem considered here, the KL Galerkin method requires $O(LNM)$ operations, where L is the number of modes in the KL model, and N and M are the number of nodes in spatial direction ξ and η respectively. The pseudospectral method requires $O(N^2M + M^2N)$ operations per time step when the spatial derivatives are evaluated by direct differentiation of the Lagrange inter-

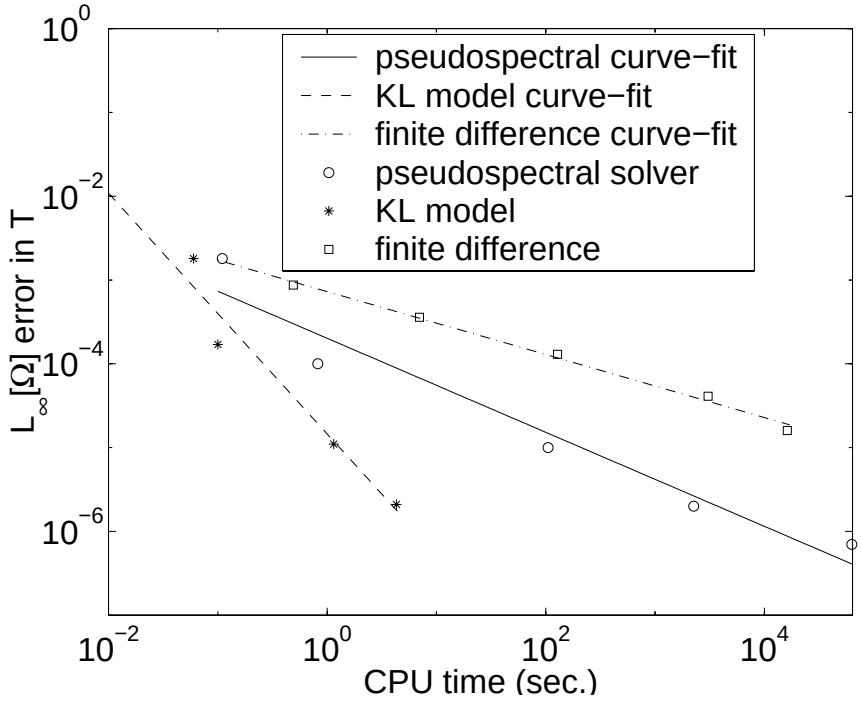

Figure 3.14. $L_\infty[\Omega]$ error in $T(\xi, \eta, \tau \to \infty)$ versus CPU time in seconds for the infinite mode boundary condition (BC1), $\Gamma = 3/2$.

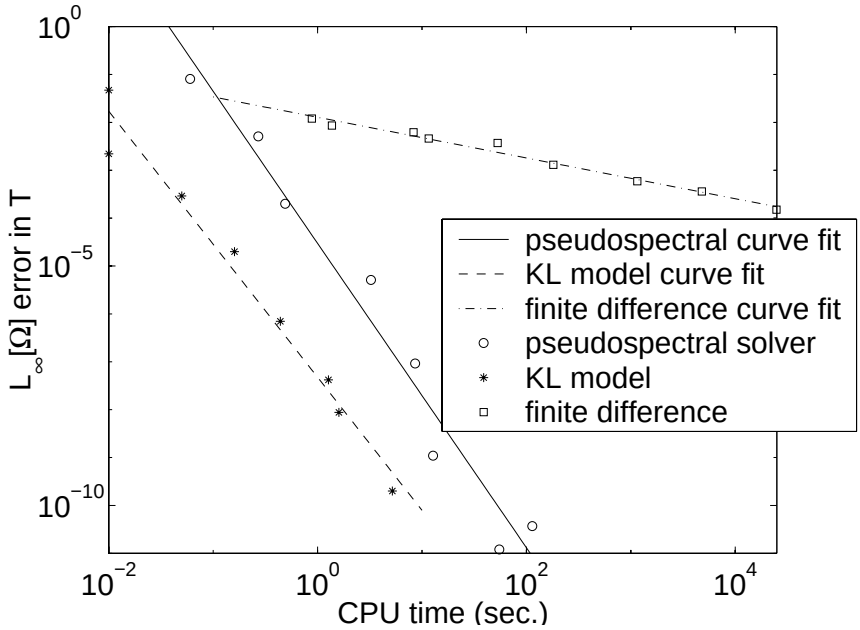

Figure 3.15. $L_\infty[\Omega]$ error in $T(\xi, \eta, \tau \to \infty)$ versus CPU time in seconds for the finite mode boundary condition (BC2), $\Gamma = 3/2$.

polating polynomials, and the finite difference method requires $O(NM)$ operations per time step, but requires a much larger N and M for the same level of accuracy as the pseudospectral method. Comparing the operation count per time step for the KL and pseudospectral methods, it is evident that when $L = N = M$, if both methods yield the same accuracy, then the pseudospectral method will have twice the operation count per time step as the KL method. For the heat conduction problem with the finite mode boundary condition, $L \approx N/3$, and $N = M$ yields the same level of accuracy for the KL and pseudospectral methods, so that the operation count per time step of the pseudospectral solver is about six times that of the KL Galerkin model. In addition, the KL method has a less restrictive time step requirement than the pseudospectral method since higher frequency information which tends to contribute to instability has been reduced by truncating the number of modes employed in the KL model. This explains why the total computational

cost of the pseudospectral method is approximately an order of magnitude greater than that of the KL Galerkin model for the finite mode case. On the other hand, for the case with the infinite mode boundary condition $L \approx N/6$ and $N \approx M$ for the same level of accuracy. For this reason, and due to the less restrictive time step requirement of the KL Galerkin model, which resulted in fewer time steps to reach a steady state solution, the computational cost of the pseudospectral method is nearly two orders of magnitude greater than that of the KL Galerkin model for the infinite mode boundary condition at an accuracy of 10^{-5}. The finite difference method has fewer operations per time step than either the KL Galerkin or pseudospectral methods, but the convergence rate is only second order rather than exponential, so that the efficiency is much lower.

Since the heat conduction problem is linear, it is possible to further reduce the number of operations per time step for the KL Galerkin method to $O(L^2)$. Similarly, a Galerkin method employing Chebyshev basis functions could be easily implemented with an operation count of $O(L^2)$ per time step, where L is the number of Chebyshev polynomials retained in the solution approximation, and a significant reduction in computational cost could be realized. This issue will be discussed further in the "Future Work" section of the conclusions.

CHAPTER 4

KARHUNEN-LOÈVE LEAST-SQUARES BLUNT BODY OPTIMAL DESIGN PROBLEM

4.1 Supersonic Blunt Body Flow and Pseudospectral Solver

4.1.1 Governing Equations

In this chapter we will develop a KL least-squares model for a two-dimensional, axisymmetric blunt body geometry in supersonic flow. The accuracy and efficiency of the KL model are compared to the accuracy and efficiency of a pseudospectral solver. A single variable design problem is solved using both the pseudospectral solver and the KL model and the results are compared.

The two-dimensional, axisymmetric Euler equations for a calorically perfect ideal gas are, in dimensionless form:

$$\frac{\partial \rho}{\partial t} + u\frac{\partial \rho}{\partial r} + w\frac{\partial \rho}{\partial z} + \rho\left(\frac{\partial u}{\partial r} + \frac{\partial w}{\partial z} + \frac{u}{r}\right) = 0, \tag{4.1}$$

$$\frac{\partial u}{\partial t} + u\frac{\partial u}{\partial r} + w\frac{\partial u}{\partial z} + \frac{1}{\rho}\frac{\partial p}{\partial r} = 0, \tag{4.2}$$

$$\frac{\partial w}{\partial t} + u\frac{\partial w}{\partial r} + w\frac{\partial w}{\partial z} + \frac{1}{\rho}\frac{\partial p}{\partial z} = 0, \tag{4.3}$$

$$\frac{\partial p}{\partial t} + u\frac{\partial p}{\partial r} + w\frac{\partial p}{\partial z} + \gamma p\left(\frac{\partial u}{\partial r} + \frac{\partial w}{\partial z} + \frac{u}{r}\right) = 0, \tag{4.4}$$

where ρ is density, p is pressure, u and w are the velocities in the radial and axial directions, respectively, r is the radial coordinate, z is the axial coordinate, t is time,

and γ is the ratio of specific heats. The dimensional form for pressure, p^*, density, ρ^*, and r^* and z^* components of velocity, u^* and w^*, respectively, are recovered from the following equations,

$$p^* = pp^*_\infty, \tag{4.5}$$

$$\rho^* = \rho\rho^*_\infty, \tag{4.6}$$

$$u^* = u\sqrt{p^*_\infty/\rho^*_\infty}, \quad w^* = w\sqrt{p^*_\infty/\rho^*_\infty}, \tag{4.7}$$

where dimensional quantities are denoted by a $*$, and freestream quantities are denoted by ∞. The dimensional space and time variables are

$$z^* = zL^*_B, \quad r^* = rL^*_B, \tag{4.8}$$

$$t^* = tL^*_B/\sqrt{p^*_\infty/\rho^*_\infty}, \tag{4.9}$$

where L^*_B is the length of the body. For this problem, we choose $z \in [-\infty, 1]$ and $r \in [0, \infty]$ and select the body geometry such that the body surface coordinates, R and Z, are in the domain $R \in [0, 1]$ and $Z \in [0, 1]$. The freestream flow is at zero angle of attack so that the component of freestream velocity in the r direction, $u_\infty = 0$. Since the dimensionless pressure, p_∞, and density, ρ_∞, are equal to unity, the component of freestream velocity in the z direction, w_∞, can be expressed as the following function of γ and the freestream Mach number, $\mathcal{M}_\infty$,

$$w_\infty = \sqrt{\gamma}\mathcal{M}_\infty. \tag{4.10}$$

Defining the entropy to be s, we have, for a calorically perfect ideal gas with zero freestream entropy,

$$s = \ln\left(\frac{p}{\rho^\gamma}\right), \tag{4.11}$$

where the entropy is non-dimensionalized by the specific heat at constant volume, c^*_v,

$$s^* = sc^*_v. \tag{4.12}$$

The following equation, which will prove useful, is an extended Crocco's theorem which is nothing more than a combination of the linear momentum principle coupled with some definitions from thermodynamics:

$$\frac{\partial \mathbf{v}}{\partial t} + \nabla h_o = T\nabla s + \mathbf{v} \times \boldsymbol{\omega}, \tag{4.13}$$

where $h_o = h + \frac{1}{2}\mathbf{v} \cdot \mathbf{v}$ is the total enthalpy, T is temperature, $\mathbf{v}$ is the velocity vector, and $\boldsymbol{\omega}$ is the vorticity vector. The dimensional temperature, T^*, total enthalpy, h_o^*, and vorticity, $\boldsymbol{\omega}^*$ can be found from the following relations

$$T^* = \frac{p_\infty^*}{c_v^* \rho_\infty^*} T, \quad h_o^* = \frac{p_\infty^*}{\rho_\infty^*} h_o, \quad \boldsymbol{\omega}^* = \frac{1}{L_B^*}\sqrt{\frac{p_\infty^*}{\rho_\infty^*}}\boldsymbol{\omega}. \tag{4.14}$$

The derivation of the extended Crocco's theorem is presented in Appendix F. In the steady state limit, the extended Crocco's theorem reduces to what is normally referred to as Crocco's theorem:

$$\nabla h_o = T\nabla s + \mathbf{v} \times \boldsymbol{\omega}. \tag{4.15}$$

We also show in Appendix F, that in the steady state limit, the total enthalpy is constant along a streamline. In addition, since the freestream flow is uniform, and since there is also no change in total enthalpy across a shock, the total enthalpy is constant everywhere for this inviscid, steady flow, which gives rise to

$$\nabla h_o = 0. \tag{4.16}$$

Thus the steady Crocco's theorem for the current problem becomes

$$T\nabla s = -\mathbf{v} \times \boldsymbol{\omega}. \tag{4.17}$$

We also present at this time, the vorticity transport equation appropriate for this unsteady, inviscid, compressible flow,

$$\frac{\partial}{\partial t}\left(\frac{\boldsymbol{\omega}}{\rho}\right) + (\mathbf{v} \cdot \nabla)\left(\frac{\boldsymbol{\omega}}{\rho}\right) = \left(\frac{\boldsymbol{\omega}}{\rho} \cdot \nabla\right)\mathbf{v} + \frac{1}{\rho^3}\nabla\rho \times \nabla p, \tag{4.18}$$

which is obtained by taking the curl of the linear momentum equation and making use of certain vector identities. We will make use of the vorticity transport equation for verification of the flow solver to be presented subsequently. Making use of the Gibbs equation in the form $T\nabla s = \nabla h - \frac{1}{\rho}\nabla p$, the vorticity transport equation can also be written in terms of temperature and entropy:

$$\frac{\partial}{\partial t}\left(\frac{\boldsymbol{\omega}}{\rho}\right) + (\mathbf{v}\cdot\nabla)\left(\frac{\boldsymbol{\omega}}{\rho}\right) = \left(\frac{\boldsymbol{\omega}}{\rho}\cdot\nabla\right)\mathbf{v} + \frac{1}{\rho}\nabla T\times\nabla s. \tag{4.19}$$

Details of the derivation of both forms of the vorticity transport equation can be found in Appendix F. For two-dimensional, steady flows the vorticity transport equation reduces to

$$(\mathbf{v}\cdot\nabla)\left(\frac{\boldsymbol{\omega}}{\rho}\right) = \frac{1}{\rho^3}\nabla\rho\times\nabla p, \tag{4.20}$$

or

$$(\mathbf{v}\cdot\nabla)\left(\frac{\boldsymbol{\omega}}{\rho}\right) = \frac{1}{\rho}\nabla T\times\nabla s. \tag{4.21}$$

From the definition for the ∇ operator in cylindrical coordinates, the vorticity transport equation, for the current two-dimensional, axisymmetric problem, reduces to the following scalar equation in the steady state limit

$$u\frac{\partial}{\partial r}\left(\frac{\omega_\theta}{\rho}\right) + w\frac{\partial}{\partial z}\left(\frac{\omega_\theta}{\rho}\right) = \frac{1}{\rho^3}\left(\frac{\partial\rho}{\partial z}\frac{\partial p}{\partial r} - \frac{\partial\rho}{\partial r}\frac{\partial p}{\partial z}\right) + \frac{u\omega_\theta}{r\rho}, \tag{4.22}$$

or

$$u\frac{\partial}{\partial r}\left(\frac{\omega_\theta}{\rho}\right) + w\frac{\partial}{\partial z}\left(\frac{\omega_\theta}{\rho}\right) = \frac{1}{\rho}\left(\frac{\partial T}{\partial z}\frac{\partial s}{\partial r} - \frac{\partial T}{\partial r}\frac{\partial s}{\partial z}\right) + \frac{u\omega_\theta}{r\rho}, \tag{4.23}$$

where the only nonzero component of vorticity, ω_θ, is in the direction normal to the $r-z$ plane.

To facilitate the solution to the Euler equations for time-varying geometry, Eqs. $(4.1-4.4)$ are rewritten in terms of a general body-fitted coordinate system,

$\xi(z,r,t)$, $\eta(z,r,t)$ and $\tau\,(z,r,t)$. Employing the chain rule of differentiation,

$$\begin{aligned}
\frac{\partial}{\partial z} &= \frac{\partial \xi}{\partial z}\frac{\partial}{\partial \xi} + \frac{\partial \eta}{\partial z}\frac{\partial}{\partial \eta} + \frac{\partial \tau}{\partial z}\frac{\partial}{\partial \tau}, \\
\frac{\partial}{\partial r} &= \frac{\partial \xi}{\partial r}\frac{\partial}{\partial \xi} + \frac{\partial \eta}{\partial r}\frac{\partial}{\partial \eta} + \frac{\partial \tau}{\partial r}\frac{\partial}{\partial \tau}, \\
\frac{\partial}{\partial t} &= \frac{\partial \xi}{\partial t}\frac{\partial}{\partial \xi} + \frac{\partial \eta}{\partial t}\frac{\partial}{\partial \eta} + \frac{\partial \tau}{\partial t}\frac{\partial}{\partial \tau},
\end{aligned} \tag{4.24}$$

and taking $\tau\,(z,r,t) = t$, the nondimensional form of Eqs. $(4.1 - 4.4)$ in generalized coordinates is

$$\frac{\partial \rho}{\partial \tau} + \widehat{u}\frac{\partial \rho}{\partial \xi} + \widehat{w}\frac{\partial \rho}{\partial \eta} + \rho\left(\frac{\partial \xi}{\partial r}\frac{\partial u}{\partial \xi} + \frac{\partial \xi}{\partial z}\frac{\partial w}{\partial \xi} + \frac{\partial \eta}{\partial r}\frac{\partial u}{\partial \eta} + \frac{\partial \eta}{\partial z}\frac{\partial w}{\partial \eta}\right) + \frac{\rho u}{r} = 0, \tag{4.25}$$

$$\frac{\partial u}{\partial \tau} + \widehat{u}\frac{\partial u}{\partial \xi} + \widehat{w}\frac{\partial u}{\partial \eta} + \frac{1}{\rho}\left(\frac{\partial \xi}{\partial r}\frac{\partial p}{\partial \xi} + \frac{\partial \eta}{\partial r}\frac{\partial p}{\partial \eta}\right) = 0, \tag{4.26}$$

$$\frac{\partial w}{\partial \tau} + \widehat{u}\frac{\partial w}{\partial \xi} + \widehat{w}\frac{\partial w}{\partial \eta} + \frac{1}{\rho}\left(\frac{\partial \xi}{\partial z}\frac{\partial p}{\partial \xi} + \frac{\partial \eta}{\partial z}\frac{\partial p}{\partial \eta}\right) = 0, \tag{4.27}$$

$$\frac{\partial p}{\partial \tau} + \widehat{u}\frac{\partial p}{\partial \xi} + \widehat{w}\frac{\partial p}{\partial \eta} + \gamma p\left(\frac{\partial \xi}{\partial r}\frac{\partial u}{\partial \xi} + \frac{\partial \xi}{\partial z}\frac{\partial w}{\partial \xi} + \frac{\partial \eta}{\partial r}\frac{\partial u}{\partial \eta} + \frac{\partial \eta}{\partial z}\frac{\partial w}{\partial \eta}\right) + \frac{\gamma p u}{r} = 0, \tag{4.28}$$

where the contravariant velocity components $\widehat{u}$ and $\widehat{w}$ are

$$\widehat{u} = \frac{\partial \xi}{\partial t} + u\frac{\partial \xi}{\partial r} + w\frac{\partial \xi}{\partial z}, \tag{4.29}$$

$$\widehat{w} = \frac{\partial \eta}{\partial t} + u\frac{\partial \eta}{\partial r} + w\frac{\partial \eta}{\partial z}. \tag{4.30}$$

The following standard relations between the metrics and inverse metrics will be necessary

$$\begin{aligned}
\frac{\partial \xi}{\partial z} &= \frac{1}{J}\frac{\partial r}{\partial \eta}, & \frac{\partial \eta}{\partial z} &= -\frac{1}{J}\frac{\partial r}{\partial \xi}, \\
\frac{\partial \xi}{\partial r} &= -\frac{1}{J}\frac{\partial z}{\partial \eta}, & \frac{\partial \eta}{\partial r} &= \frac{1}{J}\frac{\partial z}{\partial \xi}, \\
\frac{\partial \xi}{\partial t} &= \frac{\left(\frac{\partial r}{\partial \tau}\frac{\partial z}{\partial \eta} - \frac{\partial r}{\partial \eta}\frac{\partial z}{\partial \tau}\right)}{J}, & \frac{\partial \eta}{\partial t} &= \frac{\left(\frac{\partial r}{\partial \xi}\frac{\partial z}{\partial \tau} - \frac{\partial r}{\partial \tau}\frac{\partial z}{\partial \xi}\right)}{J}, \\
J &= \frac{\partial r}{\partial \eta}\frac{\partial z}{\partial \xi} - \frac{\partial r}{\partial \xi}\frac{\partial z}{\partial \eta},
\end{aligned} \tag{4.31}$$

where J is the determinant of the following metric Jacobian matrix, $\mathbf{J}$

$$\mathbf{J} = \begin{bmatrix} \frac{\partial z}{\partial \xi} & \frac{\partial z}{\partial \eta} & \frac{\partial z}{\partial \tau} \\ \frac{\partial r}{\partial \xi} & \frac{\partial r}{\partial \eta} & \frac{\partial r}{\partial \tau} \\ 0 & 0 & 1 \end{bmatrix}, \tag{4.32}$$

or for the more general case where t is a function of ξ, η, and τ

$$\mathbf{J} = \begin{bmatrix} \frac{\partial z}{\partial \xi} & \frac{\partial z}{\partial \eta} & \frac{\partial z}{\partial \tau} \\ \frac{\partial r}{\partial \xi} & \frac{\partial r}{\partial \eta} & \frac{\partial r}{\partial \tau} \\ \frac{\partial t}{\partial \xi} & \frac{\partial t}{\partial \eta} & \frac{\partial t}{\partial \tau} \end{bmatrix}. \tag{4.33}$$

4.1.2 Computational and Physical Coordinates

The physical domain of the blunt body problem, Fig. 4.1, is constructed such that the body surface lies along the computational boundary $(\xi, 0)$, the shock lies along the boundary $(\xi, 1)$, the symmetry axis is a third boundary at $(0, \eta)$, and the fourth boundary at $(1, \eta)$ is a supersonic outflow. The transformation between the physical coordinates (r, z) and computational coordinates (ξ, η) is taken to be

$$r(\xi, \eta, \tau) = R(\xi) + \frac{\eta \frac{dZ(\xi)}{d\xi} h(\xi, \tau)}{\sqrt{\left(\frac{dR(\xi)}{d\xi}\right)^2 + \left(\frac{dZ(\xi)}{d\xi}\right)^2}}, \tag{4.34}$$

$$z(\xi, \eta, \tau) = Z(\xi) - \frac{\eta \frac{dR(\xi)}{d\xi} h(\xi, \tau)}{\sqrt{\left(\frac{dR(\xi)}{d\xi}\right)^2 + \left(\frac{dZ(\xi)}{d\xi}\right)^2}}. \tag{4.35}$$

where the nonlinear function $h(\xi, \tau)$ must be specified to completely determine the mapping, and $R(\xi)$ and $Z(\xi)$ are known functions. After manipulation, the transformations in Eqs. (4.34) and (4.35) yield the following identity

$$h(\xi, \tau) = \sqrt{(z(\xi, 1, \tau) - z(\xi, 0, \tau))^2 + (r(\xi, 1, \tau) - r(\xi, 0, \tau))^2}, \tag{4.36}$$

from which it holds that the function $h(\xi, \tau)$ is the distance in $r - z$ space between the body surface, $\eta = 0$, and the shock, $\eta = 1$, along lines of constant ξ. The

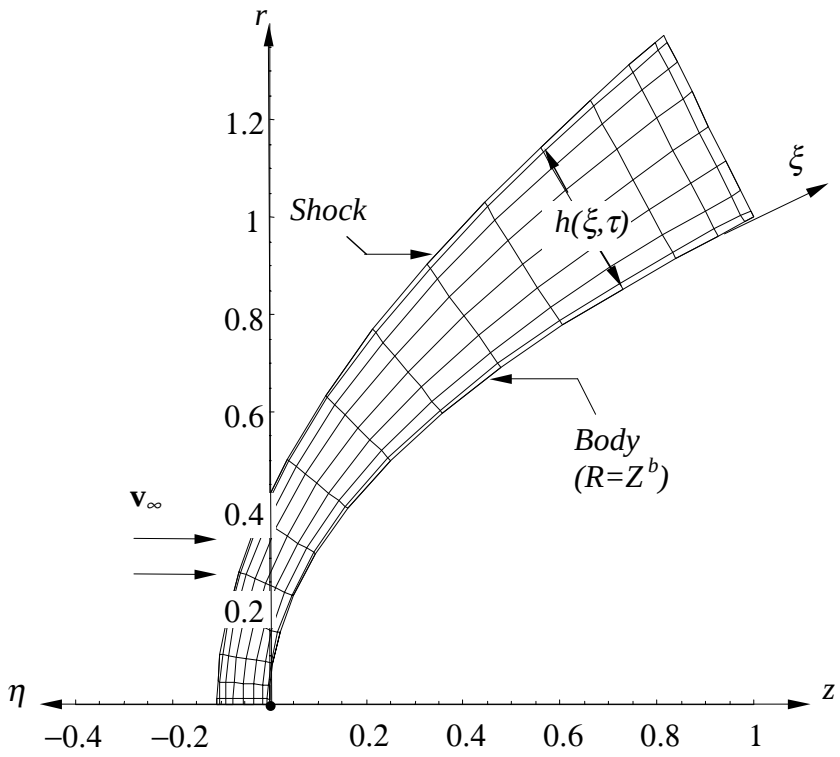

Figure 4.1. Schematic of shock-fitted high Mach number flow over an axisymmetric blunt body including computational (ξ, η) and physical (r, z) coordinates.

function $h(\xi,\tau)$ is subsequently referred to as the shock distance function. We thus see that Eqs. (4.34) and (4.35) form an implicit algebraic equation for the coordinate transformation. It is apparent from Eqs. (4.34) and (4.35) that the functions $R(\xi)$ and $Z(\xi)$ parameterize the blunt body surface, $\eta = 0$, *i.e.*

$$r(\xi,0,\tau) = R(\xi), \tag{4.37}$$
$$z(\xi,0,\tau) = Z(\xi),$$

and that the body surface is not a function of time. The transformations in Eqs. (4.34) and (4.35) have been constructed so that lines of constant ξ are normal to the body surface and have no curvature in $r-z$ space, *i.e.* the unit vector in the η direction, $\mathbf{e}_\eta$, is identical to the unit vector in the direction normal to the body surface, $\mathbf{e}_{BN}$, which is not necessarily normal to the shock except at $\eta = 0$. In order to demonstrate that $\mathbf{e}_\eta = \mathbf{e}_{BN}$, an expression for $\mathbf{e}_{BN}$ is first found by enforcing the following restriction,

$$\mathbf{e}_{BN} \cdot \mathbf{e}_{BT} = 0, \tag{4.38}$$

and employing the following definition for the unit vector in the direction tangent to the body, $\mathbf{e}_{BT}$,

$$\mathbf{e}_{BT} = \left. \frac{\frac{\partial r}{\partial \xi}\mathbf{e}_r + \frac{\partial z}{\partial \xi}\mathbf{e}_z}{\sqrt{\left(\frac{\partial r}{\partial \xi}\right)^2 + \left(\frac{\partial z}{\partial \xi}\right)^2}} \right|_{(\xi,0,\tau)}. \tag{4.39}$$

From Eqs. (4.38) and (4.39) the following expression for $\mathbf{e}_{BN}$ is obtained,

$$\mathbf{e}_{BN} = \left. \frac{\frac{\partial z}{\partial \xi}\mathbf{e}_r - \frac{\partial r}{\partial \xi}\mathbf{e}_z}{\sqrt{\left(\frac{\partial r}{\partial \xi}\right)^2 + \left(\frac{\partial z}{\partial \xi}\right)^2}} \right|_{(\xi,0,\tau)}. \tag{4.40}$$

The unit vector in the η direction is defined as

$$\mathbf{e}_\eta = \frac{\frac{\partial r}{\partial \eta}\mathbf{e}_r + \frac{\partial z}{\partial \eta}\mathbf{e}_z}{\sqrt{\left(\frac{\partial r}{\partial \eta}\right)^2 + \left(\frac{\partial z}{\partial \eta}\right)^2}}, \tag{4.41}$$

which for the transformations defined in Eqs. (4.34) and (4.35) becomes

$$\mathbf{e}_\eta = \frac{\frac{dZ(\xi)}{d\xi}\mathbf{e}_r - \frac{dR(\xi)}{d\xi}\mathbf{e}_z}{\sqrt{\left(\frac{dZ(\xi)}{d\xi}\right)^2 + \left(\frac{dR(\xi)}{d\xi}\right)^2}}. \tag{4.42}$$

Since it is apparent from Eqs. (4.34) and (4.35) that $\left.\frac{\partial z}{\partial \xi}\right|_{(\xi,0,\tau)} = \frac{dZ(\xi)}{d\xi}$ and $\left.\frac{\partial r}{\partial \xi}\right|_{(\xi,0,\tau)} = \frac{dR(\xi)}{d\xi}$, the expression for $\mathbf{e}_\eta$ in Eq. (4.42) is equivalent to $\mathbf{e}_{BN}$ in Eq. (4.40) .

Since the shock is attached to a boundary of the physical grid, the physical grid coordinates $r(\xi,\eta,\tau)$ and $z(\xi,\eta,\tau)$, will evolve in time except along the body surface, whose coordinates do not change; the body shape is fixed with respect to time. The time evolution equations for the physical grid $r(\xi,\eta,\tau)$, and $z(\xi,\eta,\tau)$ can be found by differentiating Eqs. (4.34) and (4.35) with respect to time as follows,

$$\frac{\partial}{\partial\tau} r\left(\xi,\eta,\tau\right) = \frac{\eta\frac{dZ(\xi)}{d\xi} v\left(\xi,\tau\right)}{\sqrt{\left(\frac{dR(\xi)}{d\xi}\right)^2 + \left(\frac{dZ(\xi)}{d\xi}\right)^2}}, \tag{4.43}$$

$$\frac{\partial}{\partial\tau} z\left(\xi,\eta,\tau\right) = -\frac{\eta\frac{dR(\xi)}{d\xi} v\left(\xi,\tau\right)}{\sqrt{\left(\frac{dR(\xi)}{d\xi}\right)^2 + \left(\frac{dZ(\xi)}{d\xi}\right)^2}}, \tag{4.44}$$

where the shock velocity function $v\left(\xi,\tau\right)$ is

$$v\left(\xi,\tau\right) = \frac{\partial}{\partial\tau} h\left(\xi,\tau\right). \tag{4.45}$$

For the current problem we have chosen the following functions to parameterize the blunt body surface

$$R(\xi) = \xi, \tag{4.46}$$

$$Z(\xi) = \xi^{1/b}, \tag{4.47}$$

where the domain for the geometric parameter b is restricted to $b \in (0, 2/3)$. Eliminating the parameter ξ, we see that the body surface is described by $R = Z^b$

4.1.3 Boundary Conditions

The kinematic boundary condition of no mass flux at the body surface requires that the velocity component normal to the body surface, $v_{BN}(\xi,\tau)$, be equal to zero, *i.e.*

$$v_{BN}(\xi,\tau) = \mathbf{v}|_{(\xi,0,\tau)} \cdot \mathbf{e}_{BN} = 0, \tag{4.48}$$

where $\mathbf{v}(\xi,\eta,\tau)$ is the velocity vector,

$$\mathbf{v}(\xi,\eta,\tau) = u(\xi,\eta,\tau)\,\mathbf{e}_r + w(\xi,\eta,\tau)\,\mathbf{e}_z. \tag{4.49}$$

Substituting the definition of $\mathbf{e}_{BN}$ from Eq. (4.40) into Eq. (4.48), the kinematic boundary condition at the body becomes

$$v_{BN}(\xi,\tau) = \left(u\frac{\partial z}{\partial \xi} - w\frac{\partial r}{\partial \xi}\right)\Big|_{(\xi,0,\tau)} = 0. \tag{4.50}$$

Employing the inverse metric relations from Eq. (4.31), Eq. (4.50) can also be written as

$$v_{BN}(\xi,\tau) = \left(u\frac{\partial \eta}{\partial r} + w\frac{\partial \eta}{\partial z}\right)\Big|_{(\xi,0,\tau)} = \widehat{w}(\xi,0,\tau) = 0. \tag{4.51}$$

In Eq. (4.51), the term $\frac{\partial \eta}{\partial t}\big|_{\eta=0}$ equals zero, which is apparent from the fact that $\frac{\partial z}{\partial \tau}\big|_{\eta=0} = \frac{\partial r}{\partial \tau}\big|_{\eta=0} = 0$ from Eqs. (4.34) and (4.35) and the transformation rules in Eq. (4.31).

In order to formulate a numerical boundary condition at the body for ρ, u, w, and p, Eqs. $(4.25 - 4.28)$ are written in the following form

$$\frac{\partial \mathbf{z}}{\partial \tau} + \mathbf{A}\frac{\partial \mathbf{z}}{\partial \xi} + \mathbf{B}\frac{\partial \mathbf{z}}{\partial \eta} + \mathbf{s} = \mathbf{0}, \tag{4.52}$$

where

$$\mathbf{z} = \begin{bmatrix} \rho \\ u \\ w \\ p \end{bmatrix}, \quad \mathbf{s} = \begin{bmatrix} \rho u/r \\ 0 \\ 0 \\ \gamma p u/r \end{bmatrix}, \tag{4.53}$$

$$\mathbf{A} = \begin{bmatrix} \widehat{u} & \rho\frac{\partial\xi}{\partial r} & \rho\frac{\partial\xi}{\partial z} & 0 \\ 0 & \widehat{u} & 0 & \frac{1}{\rho}\frac{\partial\xi}{\partial r} \\ 0 & 0 & \widehat{u} & \frac{1}{\rho}\frac{\partial\xi}{\partial z} \\ 0 & \gamma p\frac{\partial\xi}{\partial r} & \gamma p\frac{\partial\xi}{\partial z} & \widehat{u} \end{bmatrix}, \mathbf{B} = \begin{bmatrix} \widehat{w} & \rho\frac{\partial\eta}{\partial r} & \rho\frac{\partial\eta}{\partial z} & 0 \\ 0 & \widehat{w} & 0 & \frac{1}{\rho}\frac{\partial\eta}{\partial r} \\ 0 & 0 & \widehat{w} & \frac{1}{\rho}\frac{\partial\eta}{\partial z} \\ 0 & \gamma p\frac{\partial\eta}{\partial r} & \gamma p\frac{\partial\eta}{\partial z} & \widehat{w} \end{bmatrix}. \tag{4.54}$$

The flux Jacobian matrix $\mathbf{B}$ is then decomposed as,

$$\mathbf{B} = \mathbf{P}^{-1}\mathbf{\Lambda}_\eta\mathbf{P}, \tag{4.55}$$

where the square matrix, $\mathbf{P}$ contains the left eigenvectors of $\mathbf{B}$ in its rows; the diagonal matrix $\mathbf{\Lambda}_\eta$ contain the eigenvalues of $\mathbf{B}$ in its diagonal; and $\mathbf{P}^{-1}$ is the inverse of $\mathbf{P}$. Substituting Eq. (4.55) into Eq. (4.52) and premultiplying by $\mathbf{P}$ yields the following characteristic formulation [50, 51] of the governing equations,

$$\mathbf{P}\frac{\partial\mathbf{z}}{\partial\tau} + \mathbf{P}\mathbf{A}\frac{\partial\mathbf{z}}{\partial\xi} + \mathbf{\Lambda}_\eta\mathbf{P}\frac{\partial\mathbf{z}}{\partial\eta} + \mathbf{P}\mathbf{s} = \mathbf{0}. \tag{4.56}$$

The diagonal eigenvalue matrix, $\mathbf{\Lambda}_\eta$, and the left eigenvector matrix $\mathbf{P}$ are

$$\mathbf{\Lambda}_\eta = \begin{bmatrix} \widehat{w} & 0 & 0 & 0 \\ 0 & \widehat{w} & 0 & 0 \\ 0 & 0 & \widehat{w} - c\sqrt{\left(\frac{\partial\eta}{\partial z}\right)^2 + \left(\frac{\partial\eta}{\partial r}\right)^2} & 0 \\ 0 & 0 & 0 & \widehat{w} + c\sqrt{\left(\frac{\partial\eta}{\partial z}\right)^2 + \left(\frac{\partial\eta}{\partial r}\right)^2} \end{bmatrix}, \tag{4.57}$$

$$\mathbf{P} = \begin{bmatrix} 0 & -\frac{\frac{\partial\eta}{\partial z}\frac{\partial\eta}{\partial r}}{\left(\frac{\partial\eta}{\partial z}\right)^2+\left(\frac{\partial\eta}{\partial r}\right)^2} & \frac{\left(\frac{\partial\eta}{\partial r}\right)^2}{\left(\frac{\partial\eta}{\partial z}\right)^2+\left(\frac{\partial\eta}{\partial r}\right)^2} & 0 \\ 1 & 0 & 0 & -\frac{1}{c^2} \\ 0 & -\frac{\rho c\frac{\partial\eta}{\partial r}}{2\sqrt{\left(\frac{\partial\eta}{\partial z}\right)^2+\left(\frac{\partial\eta}{\partial r}\right)^2}} & -\frac{\rho c\frac{\partial\eta}{\partial z}}{2\sqrt{\left(\frac{\partial\eta}{\partial z}\right)^2+\left(\frac{\partial\eta}{\partial r}\right)^2}} & \frac{1}{2} \\ 0 & \frac{\rho c\frac{\partial\eta}{\partial r}}{2\sqrt{\left(\frac{\partial\eta}{\partial z}\right)^2+\left(\frac{\partial\eta}{\partial r}\right)^2}} & \frac{\rho c\frac{\partial\eta}{\partial z}}{2\sqrt{\left(\frac{\partial\eta}{\partial z}\right)^2+\left(\frac{\partial\eta}{\partial r}\right)^2}} & \frac{1}{2} \end{bmatrix}, \tag{4.58}$$

where $c = \sqrt{\gamma p/\rho}$ is the dimensionless acoustic speed. Since $\widehat{w}$ is everywhere negative and since $\|\widehat{w}\| < \|c\sqrt{\left(\frac{\partial\eta}{\partial z}\right)^2 + \left(\frac{\partial\eta}{\partial r}\right)^2}\|$ at $\eta = 0$, only the first three of the equations in Eq. (4.56) can be used in formulating numerical boundary conditions

since they are associated with negative eigenvalues, $\mathbf{\Lambda}_\eta$. The fourth equation in Eq. (4.56) is associated with a positive eigenvalue and thus describes information propagation from inside the body which must therefore be discarded as nonphysical; in its place the physical boundary condition, Eq. (4.51) , is employed. The three differential equations from Eq. (4.56) to be solved at the body surface, $\eta = 0$, are

$$\begin{aligned}&\left(\frac{\partial\eta}{\partial z}\frac{\partial u}{\partial\tau} - \frac{\partial\eta}{\partial r}\frac{\partial w}{\partial\tau} + \widehat{u}\left(\frac{\partial\eta}{\partial z}\frac{\partial u}{\partial\xi} - \frac{\partial\eta}{\partial r}\frac{\partial w}{\partial\xi}\right)\right. \\ &\left.+\widehat{w}\left(\frac{\partial\eta}{\partial z}\frac{\partial u}{\partial\eta} - \frac{\partial\eta}{\partial r}\frac{\partial w}{\partial\eta}\right) + \frac{1}{\rho}\left(\frac{\partial\eta}{\partial z}\frac{\partial\xi}{\partial r} - \frac{\partial\eta}{\partial r}\frac{\partial\xi}{\partial z}\right)\frac{\partial p}{\partial\xi}\right)\Bigg|_{(\xi,0,\tau)} \\ &= 0,\end{aligned} \tag{4.59}$$

$$\left(\frac{\partial\rho}{\partial\tau} - \frac{1}{c^2}\frac{\partial p}{\partial\tau} + \widehat{u}\left(\frac{\partial\rho}{\partial\xi} - \frac{1}{c^2}\frac{\partial p}{\partial\xi}\right) + \widehat{w}\left(\frac{\partial\rho}{\partial\eta} - \frac{1}{c^2}\frac{\partial p}{\partial\eta}\right)\right)\Bigg|_{(\xi,0,\tau)} = 0, \tag{4.60}$$

$$\begin{aligned}&\left(\frac{\partial p}{\partial\tau} - \frac{\rho c\left(\frac{\partial\eta}{\partial r}\frac{\partial u}{\partial\tau} + \frac{\partial\eta}{\partial z}\frac{\partial w}{\partial\tau}\right)}{\sqrt{\left(\frac{\partial\eta}{\partial z}\right)^2 + \left(\frac{\partial\eta}{\partial r}\right)^2}} + \rho c^2\left(\frac{\partial\xi}{\partial r}\frac{\partial u}{\partial\xi} + \frac{\partial\xi}{\partial z}\frac{\partial w}{\partial\xi}\right)\right. \\ &- \frac{\rho c\widehat{u}\left(\frac{\partial\eta}{\partial r}\frac{\partial u}{\partial\xi} + \frac{\partial\eta}{\partial z}\frac{\partial w}{\partial\xi}\right)}{\sqrt{\left(\frac{\partial\eta}{\partial z}\right)^2 + \left(\frac{\partial\eta}{\partial r}\right)^2}} + \left(\widehat{u} - \frac{c\left(\frac{\partial\eta}{\partial z}\frac{\partial\xi}{\partial z} + \frac{\partial\eta}{\partial r}\frac{\partial\xi}{\partial r}\right)}{\sqrt{\left(\frac{\partial\eta}{\partial z}\right)^2 + \left(\frac{\partial\eta}{\partial r}\right)^2}}\right)\frac{\partial p}{\partial\xi} \\ &\left.+\left(\widehat{w} - c\sqrt{\left(\frac{\partial\eta}{\partial z}\right)^2 + \left(\frac{\partial\eta}{\partial r}\right)^2}\right)\left(\frac{\partial p}{\partial\eta} - \frac{\rho c\left(\frac{\partial\eta}{\partial r}\frac{\partial u}{\partial\eta} + \frac{\partial\eta}{\partial z}\frac{\partial w}{\partial\eta}\right)}{\sqrt{\left(\frac{\partial\eta}{\partial z}\right)^2 + \left(\frac{\partial\eta}{\partial r}\right)^2}}\right) + \frac{\rho c^2 u}{r}\right)\Bigg|_{(\xi,0,\tau)} \\ &= 0,\end{aligned} \tag{4.61}$$

which are obtained from the first three equations in Eq. (4.56) .

Eqs. $(4.59 - 4.61)$ are not in the same form as Eq. (2.2), and so we will proceed to put them into that form. Taking the derivative of Eq. (4.50) with respect to time yields

$$\left(\frac{\partial}{\partial\tau}\left(u\frac{\partial z}{\partial\xi} - w\frac{\partial r}{\partial\xi}\right) = \frac{\partial z}{\partial\xi}\frac{\partial u}{\partial\tau} - \frac{\partial r}{\partial\xi}\frac{\partial w}{\partial\tau} + u\frac{\partial}{\partial\tau}\left(\frac{\partial z}{\partial\xi}\right) - w\frac{\partial}{\partial\tau}\left(\frac{\partial r}{\partial\xi}\right)\right)\Bigg|_{(\xi,0,\tau)} = 0, \tag{4.62}$$

or since the body surface is fixed in time, the terms $\frac{\partial}{\partial\tau}\left(\frac{\partial z}{\partial\xi}\right)$ and $\frac{\partial}{\partial\tau}\left(\frac{\partial r}{\partial\xi}\right)$ are equal to zero, and we have

$$\left(\frac{\partial z}{\partial\xi}\frac{\partial u}{\partial\tau}-\frac{\partial r}{\partial\xi}\frac{\partial w}{\partial\tau}\right)\Bigg|_{(\xi,0,\tau)}=0, \tag{4.63}$$

or in terms of the inverse metrics

$$\left(\frac{\partial\eta}{\partial r}\frac{\partial u}{\partial\tau}+\frac{\partial\eta}{\partial z}\frac{\partial w}{\partial\tau}\right)\Bigg|_{(\xi,0,\tau)}=0. \tag{4.64}$$

At the body surface, the velocity component tangent to the body surface is defined as

$$v_{BT}\left(\xi,\tau\right)=\mathbf{v}|_{(\xi,0,\tau)}\cdot\mathbf{e}_{BT}, \tag{4.65}$$

where

$$\mathbf{v}|_{(\xi,0,\tau)}\cdot\mathbf{e}_{BT}=\left.\frac{u\frac{\partial r}{\partial\xi}+w\frac{\partial z}{\partial\xi}}{\sqrt{\left(\frac{\partial r}{\partial\xi}\right)^{2}+\left(\frac{\partial z}{\partial\xi}\right)^{2}}}\right|_{(\xi,0,\tau)}. \tag{4.66}$$

Differentiating Eq. (4.66) with respect to time yields

$$\begin{aligned}\frac{\partial}{\partial\tau}v_{BT}\left(\xi,\tau\right)&=\frac{\partial}{\partial\tau}\left.\left(\frac{u\frac{\partial r}{\partial\xi}+w\frac{\partial z}{\partial\xi}}{\sqrt{\left(\frac{\partial r}{\partial\xi}\right)^{2}+\left(\frac{\partial z}{\partial\xi}\right)^{2}}}\right)\right|_{(\xi,0,\tau)} \qquad (4.67)\\ &=\left.\left(\frac{\frac{\partial r}{\partial\xi}\frac{\partial u}{\partial\tau}+\frac{\partial z}{\partial\xi}\frac{\partial w}{\partial\tau}+u\frac{\partial^{2}r}{\partial\tau\partial\xi}+w\frac{\partial^{2}z}{\partial\tau\partial\xi}}{\sqrt{\left(\frac{\partial r}{\partial\xi}\right)^{2}+\left(\frac{\partial z}{\partial\xi}\right)^{2}}}-\frac{\left(\frac{\partial r}{\partial\xi}\frac{\partial^{2}r}{\partial\tau\partial\xi}+\frac{\partial z}{\partial\xi}\frac{\partial^{2}z}{\partial\tau\partial\xi}\right)\left(u\frac{\partial r}{\partial\xi}+w\frac{\partial z}{\partial\xi}\right)}{\left(\left(\frac{\partial r}{\partial\xi}\right)^{2}+\left(\frac{\partial z}{\partial\xi}\right)^{2}\right)^{3/2}}\right)\right|_{(\xi,0,\tau)},\end{aligned}$$

or since the terms $\frac{\partial^2 z}{\partial\tau\partial\xi}$ and $\frac{\partial^2 r}{\partial\tau\partial\xi}$ are equal to zero at $\eta=0$, the evolution equation for $v_{BT}\left(\xi,\tau\right)$ is defined as

$$\frac{\partial}{\partial\tau}v_{BT}\left(\xi,\tau\right)=\left.\left(\frac{\frac{\partial r}{\partial\xi}\frac{\partial u}{\partial\tau}+\frac{\partial z}{\partial\xi}\frac{\partial w}{\partial\tau}}{\sqrt{\left(\frac{\partial r}{\partial\xi}\right)^{2}+\left(\frac{\partial z}{\partial\xi}\right)^{2}}}\right)\right|_{(\xi,0,\tau)}=\left.\left(\frac{-\frac{\partial\eta}{\partial z}\frac{\partial u}{\partial\tau}+\frac{\partial\eta}{\partial r}\frac{\partial w}{\partial\tau}}{\sqrt{\left(\frac{\partial\eta}{\partial z}\right)^{2}+\left(\frac{\partial\eta}{\partial r}\right)^{2}}}\right)\right|_{(\xi,0,\tau)}. \tag{4.68}$$

Substituting Eq. (4.68) into Eq. (4.59) and making use of Eq. (4.51) yields the following evolution equation for $v_{BT}(\xi,\tau)$,

$$\frac{\partial}{\partial\tau}v_{BT}(\xi,\tau)=\left.\frac{\left(\widehat{u}\left(\frac{\partial\eta}{\partial r}\frac{\partial w}{\partial\xi}-\frac{\partial\eta}{\partial z}\frac{\partial u}{\partial\xi}\right)+\frac{1}{\rho}\left(\frac{\partial\eta}{\partial r}\frac{\partial\xi}{\partial z}-\frac{\partial\eta}{\partial z}\frac{\partial\xi}{\partial r}\right)\frac{\partial p}{\partial\xi}\right)}{\sqrt{\left(\frac{\partial\eta}{\partial z}\right)^2+\left(\frac{\partial\eta}{\partial r}\right)^2}}\right|_{(\xi,0,\tau)}. \tag{4.69}$$

Substituting Eq. (4.64) into Eq. (4.61) and making use of the fact that $\widehat{w}(\xi,0,\tau)=0$ yields the following evolution equation for p at $\eta=0$

$$\left(\frac{\partial p}{\partial\tau}=\frac{\rho c\widehat{u}\left(\frac{\partial\eta}{\partial r}\frac{\partial u}{\partial\xi}+\frac{\partial\eta}{\partial z}\frac{\partial w}{\partial\xi}\right)+c\left(\frac{\partial\eta}{\partial r}\frac{\partial\xi}{\partial r}+\frac{\partial\eta}{\partial z}\frac{\partial\xi}{\partial z}\right)\frac{\partial p}{\partial\xi}}{\sqrt{\left(\frac{\partial\eta}{\partial z}\right)^2+\left(\frac{\partial\eta}{\partial r}\right)^2}}\right. \tag{4.70}$$
$$-\rho c^2\left(\frac{\partial\xi}{\partial r}\frac{\partial u}{\partial\xi}+\frac{\partial\xi}{\partial z}\frac{\partial w}{\partial\xi}+\frac{\partial\eta}{\partial r}\frac{\partial u}{\partial\eta}+\frac{\partial\eta}{\partial z}\frac{\partial w}{\partial\eta}\right)$$
$$\left.+c\sqrt{\left(\frac{\partial\eta}{\partial z}\right)^2+\left(\frac{\partial\eta}{\partial r}\right)^2}\frac{\partial p}{\partial\eta}-\widehat{u}\frac{\partial p}{\partial\xi}-\frac{\rho c^2u}{r}\right)\Bigg|_{(\xi,0,\tau)}.$$

Substituting Eq. (4.51) into Eq. (4.60) yields the following equation for ρ at $\eta=0$

$$\left.\left(\frac{\partial\rho}{\partial\tau}=\frac{1}{c^2}\frac{\partial p}{\partial\tau}-\widehat{u}\left(\frac{\partial\rho}{\partial\xi}-\frac{1}{c^2}\frac{\partial p}{\partial\xi}\right)\right)\right|_{(\xi,0,\tau)}, \tag{4.71}$$

where in place of the term $\frac{\partial p}{\partial\tau}$ in Eq. (4.71) the right-hand side of Eq. (4.70) is employed. The velocity components $u(\xi,0,\tau)$ and $w(\xi,0,\tau)$ can be easily found from Eqs. (4.50) and (4.66), as a function of $v_{BT}(\xi,\tau)$, and the result is the following,

$$u(\xi,0,\tau)=\left.\frac{\frac{\partial r}{\partial\xi}v_{BT}(\xi,\tau)}{\sqrt{\left(\frac{\partial r}{\partial\xi}\right)^2+\left(\frac{\partial z}{\partial\xi}\right)^2}}\right|_{(\xi,0,\tau)},\quad w(\xi,0,\tau)=\left.\frac{\frac{\partial z}{\partial\xi}v_{BT}(\xi,\tau)}{\sqrt{\left(\frac{\partial r}{\partial\xi}\right)^2+\left(\frac{\partial z}{\partial\xi}\right)^2}}\right|_{(\xi,0,\tau)}. \tag{4.72}$$

At the shock boundary, the Rankine-Hugoniot relations are solved along with a compatibility equation. Specifically, the Rankine-Hugoniot relations are

$$\mathbf{v}_\infty\cdot\mathbf{e}_{ST}|_{(\xi,1,\tau)}=\mathbf{v}\cdot\mathbf{e}_{ST}|_{(\xi,1,\tau)}, \tag{4.73}$$

$$\delta_S(\xi,\tau)=\frac{\gamma-1}{\gamma+1}\delta_\infty(\xi,\tau)+\frac{2\gamma}{(\gamma+1)\,\delta_\infty(\xi,\tau)}, \tag{4.74}$$

$$p\left(\xi,1,\tau\right)=\frac{2}{\gamma+1}\delta_{\infty}^{2}\left(\xi,\tau\right)-\frac{\gamma-1}{\gamma+1}, \tag{4.75}$$

$$\rho\left(\xi,1,\tau\right)=\frac{\delta_{\infty}\left(\xi,\tau\right)}{\delta_{S}\left(\xi,\tau\right)}, \tag{4.76}$$

where δ_S and δ_∞ are the component of fluid velocity normal to the shock in the shock-attached reference frame on the downstream and freestream sides of the shock respectively, *i.e.*

$$\begin{aligned}\delta_{S}\left(\xi,\tau\right)&=\mathbf{v}\cdot\mathbf{e}_{SN}|_{(\xi,1,\tau)}-v_{SN}\left(\xi,\tau\right),\\&=\mathbf{v}\cdot\mathbf{e}_{SN}|_{(\xi,1,\tau)}-\left(\mathbf{e}_{\eta}\cdot\mathbf{e}_{SN}\right)v\left(\xi,\tau\right),\end{aligned} \tag{4.77}$$

$$\delta_{\infty}\left(\xi,\tau\right)=\mathbf{v}_{\infty}\cdot\mathbf{e}_{SN}|_{(\xi,1,\tau)}-\left(\mathbf{e}_{\eta}\cdot\mathbf{e}_{SN}\right)v\left(\xi,\tau\right), \tag{4.78}$$

and the nondimensional freestream velocity vector $\mathbf{v}_\infty$, is

$$\mathbf{v}_{\infty}=\sqrt{\gamma}\mathcal{M}_{\infty}\mathbf{e}_{z}. \tag{4.79}$$

In Eqs. $(4.73-4.77)$, $\mathbf{e}_{ST}$ is a unit vector in the direction tangent to the shock wave, $\mathbf{e}_{SN}$ is a unit vector in the direction normal to the shock wave, and $v_{SN}\left(\xi,\tau\right)$ and $v\left(\xi,\tau\right)$ are the velocities of the shock in the, $\mathbf{e}_{SN}$, and, $\mathbf{e}_{\eta}$, directions respectively. Quantities denoted with a subscript of ∞ are freestream quantities, and those with no subscripts are post shock quantities. The unit vectors $\mathbf{e}_{ST}$ and $\mathbf{e}_{SN}$, are in terms of the inverse metrics

$$\mathbf{e}_{ST}=\left.\frac{-\frac{\partial\eta}{\partial z}\mathbf{e}_{r}+\frac{\partial\eta}{\partial r}\mathbf{e}_{z}}{\sqrt{\left(\frac{\partial\eta}{\partial z}\right)^{2}+\left(\frac{\partial\eta}{\partial r}\right)^{2}}}\right|_{(\xi,1,\tau)}, \tag{4.80}$$

$$\mathbf{e}_{SN}=\left.\frac{\frac{\partial\eta}{\partial r}\mathbf{e}_{r}+\frac{\partial\eta}{\partial z}\mathbf{e}_{z}}{\sqrt{\left(\frac{\partial\eta}{\partial z}\right)^{2}+\left(\frac{\partial\eta}{\partial r}\right)^{2}}}\right|_{(\xi,1,\tau)}. \tag{4.81}$$

In order to solve the Rankine-Hugoniot equations, an expression for the shock velocity, $v\left(\xi,\tau\right)$, is needed. Differentiating Eqs. (4.74) and (4.75) with respect to time yields

$$\frac{\partial}{\partial\tau}\delta_{S}\left(\xi,\tau\right)=A_{1}\left(\xi,\tau\right)\frac{\partial}{\partial\tau}\delta_{\infty}\left(\xi,\tau\right), \tag{4.82}$$

$$\frac{\partial}{\partial\tau}p\left(\xi,1,\tau\right)=A_2\left(\xi,\tau\right)\frac{\partial}{\partial\tau}\delta_\infty\left(\xi,\tau\right), \tag{4.83}$$

where

$$A_1\left(\xi,\tau\right)=\frac{\gamma-1}{\gamma+1}-\frac{2\gamma}{\left(\gamma+1\right)\delta_\infty^2\left(\xi,\tau\right)},\quad A_2\left(\xi,\tau\right)=\frac{4\delta_\infty\left(\xi,\tau\right)}{\gamma+1}. \tag{4.84}$$

The terms $\frac{\partial}{\partial\tau}\delta_S\left(\xi,\tau\right)$ and $\frac{\partial}{\partial\tau}\delta_\infty\left(\xi,\tau\right)$ in Eqs. (4.82) and (4.83) are found by differentiating Eqs. (4.77) and (4.78) respectively to yield the following,

$$\frac{\partial}{\partial\tau}\delta_S\left(\xi,\tau\right)=\left(\frac{\partial\mathbf{v}}{\partial\tau}\cdot\mathbf{e}_{SN}+\mathbf{v}\cdot\frac{\partial\mathbf{e}_{SN}}{\partial\tau}-\left(\mathbf{e}_\eta\cdot\mathbf{e}_{SN}\right)\frac{\partial v}{\partial\tau}-v\mathbf{e}_\eta\cdot\frac{\partial\mathbf{e}_{SN}}{\partial\tau}\right)\Bigg|_{(\xi,1,\tau)}, \tag{4.85}$$

$$\frac{\partial}{\partial\tau}\delta_\infty\left(\xi,\tau\right)=\left(\frac{\partial\mathbf{v}_\infty}{\partial\tau}\cdot\mathbf{e}_{SN}+\mathbf{v}_\infty\cdot\frac{\partial\mathbf{e}_{SN}}{\partial\tau}-\left(\mathbf{e}_\eta\cdot\mathbf{e}_{SN}\right)\frac{\partial v}{\partial\tau}-v\mathbf{e}_\eta\cdot\frac{\partial\mathbf{e}_{SN}}{\partial\tau}\right)\Bigg|_{(\xi,1,\tau)}. \tag{4.86}$$

Multiplying Eq. (4.82) by ρc and adding it to Eq. (4.83), and replacing the term $\frac{\partial}{\partial\tau}\delta_S\left(\xi,\tau\right)$ by Eq. (4.85) and the term $\frac{\partial}{\partial\tau}\delta_\infty\left(\xi,\tau\right)$ by (4.86), we arrive at the following equation for the shock acceleration $\frac{\partial}{\partial\tau}v\left(\xi,\tau\right)$,

$$\frac{\partial}{\partial\tau}v\left(\xi,\tau\right)=\frac{\left(\left(A_2+\rho cA_1\right)\left(\mathbf{v}_\infty-v\mathbf{e}_\eta\right)-\rho c\left(\mathbf{v}-v\mathbf{e}_\eta\right)\right)\cdot\frac{\partial\mathbf{e}_{SN}}{\partial\tau}-\rho c\frac{\partial\mathbf{v}}{\partial\tau}\cdot\mathbf{e}_{SN}-\frac{\partial p}{\partial\tau}}{\left(\mathbf{e}_\eta\cdot\mathbf{e}_{SN}\right)\left(A_2+\rho c\left(A_1-1\right)\right)}\Bigg|_{(\xi,1,\tau)}. \tag{4.87}$$

The terms $\frac{\partial p}{\partial\tau}$ and $\rho c\frac{\partial\mathbf{v}}{\partial\tau}\cdot\mathbf{e}_{SN}$ must be specified by a compatibility equation which is the characteristic equation associated with the wave propagating from the body to the shock along the normal direction. This compatibility equation is in the same form as the fourth compatibility equation in Eq. (4.56) only written in shock coordinates instead of the body coordinate system (ξ,η,τ). After some simplification, the following shock acceleration equation is obtained

$$\frac{\partial}{\partial\tau}v\left(\xi,\tau\right)=\frac{\left(A_2+\rho cA_1\right)\left(\mathbf{v}_\infty-v\mathbf{e}_\eta\right)\cdot\frac{\partial\mathbf{e}_{SN}}{\partial\tau}-\rho c\left(\mathbf{v}-v\mathbf{e}_\eta\right)\cdot\frac{\partial\mathbf{e}_{SN}}{\partial\tau}+A_3}{\left(\mathbf{e}_\eta\cdot\mathbf{e}_{SN}\right)\left(A_2+\rho c\left(A_1-1\right)\right)}\Bigg|_{(\xi,1,\tau)}, \tag{4.88}$$

where

$$A_3 = \widehat{u}\frac{\partial p}{\partial \xi} + \widehat{w}\frac{\partial p}{\partial \eta} + \gamma p\left(\frac{\partial \xi}{\partial z}\frac{\partial w}{\partial \xi} + \frac{\partial \eta}{\partial z}\frac{\partial w}{\partial \eta} + \frac{\partial \xi}{\partial r}\frac{\partial u}{\partial \xi} + \frac{\partial \eta}{\partial r}\frac{\partial u}{\partial \eta}\right) \tag{4.89}$$

$$\rho c\left(\frac{\frac{\partial z}{\partial \xi}}{\sqrt{\left(\frac{\partial z}{\partial \xi}\right)^2 + \left(\frac{\partial r}{\partial \xi}\right)^2}}\left(\widehat{u}\frac{\partial u_r}{\partial \xi} + \widehat{w}\frac{\partial u}{\partial \eta} + \frac{1}{\rho}\left(\frac{\partial \xi}{\partial r}\frac{\partial p}{\partial \xi} + \frac{\partial \eta}{\partial r}\frac{\partial p}{\partial \eta}\right)\right)\right.$$

$$\left. - \frac{\frac{\partial r}{\partial \xi}}{\sqrt{\left(\frac{\partial z}{\partial \xi}\right)^2 + \left(\frac{\partial r}{\partial \xi}\right)^2}}\left(\widehat{u}\frac{\partial w}{\partial \xi} + \widehat{w}\frac{\partial w}{\partial \eta} + \frac{1}{\rho}\left(\frac{\partial \xi}{\partial z}\frac{\partial p}{\partial \xi} + \frac{\partial \eta}{\partial z}\frac{\partial p}{\partial \eta}\right)\right)\right) + \frac{\gamma p u}{r}.$$

The time derivative of the normal unit vector, $\frac{\partial \mathbf{e}_{SN}}{\partial \tau}$, is found by taking the time derivative of Eq. (4.81) with the metrics from Eq. (4.31) in place of the inverse metrics to yield,

$$\frac{\partial \mathbf{e}_{SN}}{\partial \tau} = \frac{\left(\frac{\partial r}{\partial \xi}\frac{\partial^2 z}{\partial \tau \partial \xi} - \frac{\partial z}{\partial \xi}\frac{\partial^2 r}{\partial \tau \partial \xi}\right)\left(\frac{\partial z}{\partial \xi}\mathbf{e}_z + \frac{\partial r}{\partial \xi}\mathbf{e}_r\right)}{\left(\left(\frac{\partial z}{\partial \xi}\right)^2 + \left(\frac{\partial r}{\partial \xi}\right)^2\right)^{3/2}}. \tag{4.90}$$

Since there is a geometric singularity in Eq. (4.89) at $r = 0$, an alternate expression for $v(0, \tau)$ is needed. Taking the derivative of Eq. (4.35) with respect to ξ yields

$$\frac{\partial}{\partial \xi} z(\xi, \eta, \tau) = \frac{dZ(\xi)}{d\xi} - \frac{\eta \frac{d^2 R(\xi)}{d\xi^2} h(\xi, \tau)}{\sqrt{\left(\frac{dR(\xi)}{d\xi}\right)^2 + \left(\frac{dZ(\xi)}{d\xi}\right)^2}} - \frac{\eta \frac{dR(\xi)}{d\xi}\frac{d}{d\xi} h(\xi, \tau)}{\sqrt{\left(\frac{dR(\xi)}{d\xi}\right)^2 + \left(\frac{dZ(\xi)}{d\xi}\right)^2}} \tag{4.91}$$

$$+ \frac{\eta \frac{dR(\xi)}{d\xi} h(\xi, \tau)\left(\frac{dR(\xi)}{d\xi}\frac{d^2 R(\xi)}{d\xi^2} + \frac{dZ(\xi)}{d\xi}\frac{d^2 Z(\xi)}{d\xi^2}\right)}{\left(\left(\frac{dR(\xi)}{d\xi}\right)^2 + \left(\frac{dZ(\xi)}{d\xi}\right)^2\right)^{3/2}},$$

and since for our problem

$$\frac{dR(\xi)}{d\xi} = 1, \tag{4.92}$$

$$\frac{dZ(\xi)}{d\xi} = \frac{1}{b}\xi^{\frac{1}{b}-1}, \tag{4.93}$$

$$\frac{d^2 R(\xi)}{d\xi^2} = 0, \tag{4.94}$$

$$\frac{d^2 Z(\xi)}{d\xi^2} = \frac{1-b}{b^2}\xi^{\frac{1}{b}-2}, \tag{4.95}$$

Eq. (4.91) becomes

$$\frac{\partial}{\partial\xi} z(\xi,\eta,\tau) = \frac{1}{b}\xi^{\frac{1}{b}-1} - \frac{\eta\frac{\partial}{\partial\xi}h(\xi,\tau)}{\sqrt{1+\frac{1}{b^2}\xi^{\frac{2}{b}-2}}} + \frac{(1-b)\,\eta h(\xi,\tau)\,\xi^{\frac{2}{b}-3}}{b^3\left(1+\frac{1}{b^2}\xi^{\frac{2}{b}-2}\right)^{3/2}}. \tag{4.96}$$

Evaluating Eq. (4.96) at $\xi = 0$ yields for $b \in (0, 2/3)$,

$$\left.\frac{\partial z}{\partial\xi}\right|_{(0,\eta,\tau)} = -\eta \left.\frac{\partial h}{\partial\xi}\right|_{(0,\tau)}. \tag{4.97}$$

At the centerline, $\xi = 0$, the shock is taken to be normal to the z axis so that

$$\left.\frac{\partial z}{\partial\xi}\right|_{(0,1,\tau)} = 0, \tag{4.98}$$

which from Eq. (4.97) yields

$$\left.\frac{\partial h}{\partial\xi}\right|_{(0,\tau)} = 0, \tag{4.99}$$

and consequently from Eq. (4.45), we have the following expression for $v(0,\tau)$,

$$\frac{\partial}{\partial\xi} v(0,\tau) = 0. \tag{4.100}$$

Applying Eq. (4.99), to Eq. (4.97) at the boundary $\xi = 0$, the following expression holds,

$$\left.\frac{\partial z}{\partial\xi}\right|_{(0,\eta,\tau)} = 0. \tag{4.101}$$

We impose the following appropriate boundary conditions on the centerline, $\xi = 0$, in computational coordinates

$$\left.\frac{\partial w}{\partial\xi}\right|_{(0,\eta,\tau)} = 0, \tag{4.102}$$

$$\left.\frac{\partial p}{\partial\xi}\right|_{(0,\eta,\tau)} = 0, \tag{4.103}$$

$$u(0,\eta,\tau) = 0, \tag{4.104}$$

$$\rho(0,\eta,\tau) = \rho(0,1,\tau)\left(\frac{p(0,\eta,\tau)}{p(0,1,\tau)}\right)^{1/\gamma}, \tag{4.105}$$

where use has been made of Eq. (4.101) and the transformation rules from Eq. (4.24) to transform the boundary conditions in $r-z$ space, $\frac{\partial w}{\partial r}\big|_{(0,z,t)} = \frac{\partial p}{\partial r}\big|_{(0,z,t)} = 0$ to $\xi - \eta$ space. The boundary condition in Eq. (4.105) comes from casting the energy equation, Eq. (4.4) , in terms of the non-dimensional entropy, s,

$$\frac{\partial s}{\partial t} + u\frac{\partial s}{\partial r} + w\frac{\partial s}{\partial z} = 0. \tag{4.106}$$

Enforcing steady state, $\frac{\partial s}{\partial t} = 0$, and zero velocity in the r direction, $u\left(0,\eta,\tau\right) = 0$, Eq. (4.106) reduces to $\frac{\partial s}{\partial z}\big|_{(0,\eta,\tau)} = 0$. Thus $s\left(0,\eta,\tau\right)$ is constant and equal to $s\left(0,1,\tau\right)$, the nondimensional value of the entropy downstream of the shock. Substituting $s\left(0,\eta,\tau\right) = \ln\left(\frac{p(0,1,\tau)}{\rho(0,1,\tau)^{\gamma}}\right)$ into the equation for entropy, Eq. (4.11) , and simplifying gives the boundary condition in Eq. (4.105). We note that the enforcement of steady state for entropy is artificial and potentially precludes some classes of unsteady behavior.

At the supersonic outflow boundary, $\xi = 1$, no physical boundary conditions are required as all waves are exiting the domain. Here the governing equations are solved in exactly the same manner as in the interior.

4.1.4 Summary of Governing Equations and Boundary Conditions

The governing equations and boundary conditions can be written in terms of the system of time-dependent partial differential and algebraic equations in Eqs. $(2.2 - 2.4)$

in the two space dimensions, ξ and η, where

$$\mathbf{y}\left(\xi,\eta,\tau\right)=\left[\begin{array}{c}\rho\left(\xi,\eta,\tau\right)\\ u\left(\xi,\eta,\tau\right)\\ w\left(\xi,\eta,\tau\right)\\ p\left(\xi,\eta,\tau\right)\\ r\left(\xi,\eta,\tau\right)\\ z\left(\xi,\eta,\tau\right)\\ v_{BT}\left(\xi,\tau\right)\\ \rho\left(\xi,0,\tau\right)\\ p\left(\xi,0,\tau\right)\\ v\left(\xi,\tau\right)\end{array}\right], \tag{4.107}$$

$$\mathbf{f}=\left[\begin{array}{ll}-\widehat{u}\frac{\partial u}{\partial\xi}-\widehat{w}\frac{\partial u}{\partial\eta}-\frac{1}{\rho}\left(\frac{\partial\xi}{\partial r}\frac{\partial p}{\partial\xi}+\frac{\partial\eta}{\partial r}\frac{\partial p}{\partial\eta}\right) & \text{Eq. (4.25)}\\ -\widehat{u}\frac{\partial w}{\partial\xi}-\widehat{w}\frac{\partial w}{\partial\eta}-\frac{1}{\rho}\left(\frac{\partial\xi}{\partial z}\frac{\partial p}{\partial\xi}+\frac{\partial\eta}{\partial z}\frac{\partial p}{\partial\eta}\right) & \text{Eq. (4.26)}\\ -\widehat{u}\frac{\partial p}{\partial\xi}-\widehat{w}\frac{\partial p}{\partial\eta}-\gamma p\left(\frac{\partial\xi}{\partial r}\frac{\partial u}{\partial\xi}+\frac{\partial\xi}{\partial z}\frac{\partial w}{\partial\xi}+\frac{\partial\eta}{\partial r}\frac{\partial u}{\partial\eta}+\frac{\partial\eta}{\partial z}\frac{\partial w}{\partial\eta}\right)-\frac{\gamma pu}{r} & \text{Eq. (4.27)}\\ -\widehat{u}\frac{\partial\rho}{\partial\xi}-\widehat{w}\frac{\partial\rho}{\partial\eta}-\rho\left(\frac{\partial\xi}{\partial r}\frac{\partial u}{\partial\xi}+\frac{\partial\xi}{\partial z}\frac{\partial w}{\partial\xi}+\frac{\partial\eta}{\partial r}\frac{\partial u}{\partial\eta}+\frac{\partial\eta}{\partial z}\frac{\partial w}{\partial\eta}\right)-\frac{\rho u}{r} & \text{Eq. (4.28)}\\ \frac{\eta\frac{\partial Z(\xi)}{\partial\xi}v(\xi,\tau)}{\sqrt{\left(\frac{\partial R(\xi)}{\partial\xi}\right)^2+\left(\frac{\partial Z(\xi)}{\partial\xi}\right)^2}} & \text{Eq. (4.43)}\\ -\frac{\eta\frac{\partial R(\xi)}{\partial\xi}v(\xi,\tau)}{\sqrt{\left(\frac{\partial R(\xi)}{\partial\xi}\right)^2+\left(\frac{\partial Z(\xi)}{\partial\xi}\right)^2}} & \text{Eq. (4.44)}\\ \left.-\frac{\left(\widehat{u}\left(\frac{\partial\eta}{\partial r}\frac{\partial w}{\partial\xi}-\frac{\partial\eta}{\partial z}\frac{\partial u}{\partial\xi}\right)+\frac{1}{\rho}\left(\frac{\partial\eta}{\partial r}\frac{\partial\xi}{\partial z}-\frac{\partial\eta}{\partial z}\frac{\partial\xi}{\partial r}\right)\frac{\partial p}{\partial\xi}\right)}{\sqrt{\left(\frac{\partial\eta}{\partial z}\right)^2+\left(\frac{\partial\eta}{\partial r}\right)^2}}\right|_{(\xi,0,\tau)} & \text{Eq. (4.69)}\\ \left.\left(-\frac{1}{c^2}\frac{\partial p}{\partial\tau}+\widehat{u}\left(\frac{\partial\rho}{\partial\xi}-\frac{1}{c^2}\frac{\partial p}{\partial\xi}\right)\right)\right|_{(\xi,0,\tau)} & \text{Eq. (4.71)}\\ \left.\begin{array}{r}-\left(\frac{\rho c\widehat{u}\left(\frac{\partial\eta}{\partial r}\frac{\partial u}{\partial\xi}+\frac{\partial\eta}{\partial z}\frac{\partial w}{\partial\xi}\right)+c\left(\frac{\partial\eta}{\partial r}\frac{\partial\xi}{\partial r}+\frac{\partial\eta}{\partial z}\frac{\partial\xi}{\partial z}\right)\frac{\partial p}{\partial\xi}}{\sqrt{\left(\frac{\partial\eta}{\partial z}\right)^2+\left(\frac{\partial\eta}{\partial r}\right)^2}}\right.\\ -\rho c^2\left(\frac{\partial\xi}{\partial r}\frac{\partial u}{\partial\xi}+\frac{\partial\xi}{\partial z}\frac{\partial w}{\partial\xi}+\frac{\partial\eta}{\partial r}\frac{\partial u}{\partial\eta}+\frac{\partial\eta}{\partial z}\frac{\partial w}{\partial\eta}\right)\\ \left.+c\sqrt{\left(\frac{\partial\eta}{\partial z}\right)^2+\left(\frac{\partial\eta}{\partial r}\right)^2}\frac{\partial p}{\partial\eta}-\widehat{u}\frac{\partial p}{\partial\xi}-\frac{\rho c^2u}{r}\right)\end{array}\right|_{(\xi,0,\tau)} & \text{Eq. (4.70)}\\ -\left.\left(\frac{(A_2+\rho cA_1)(\mathbf{v}_\infty-v\mathbf{e}_\eta)\cdot\frac{\partial\mathbf{e}_{SN}}{\partial\tau}-\rho c(\mathbf{v}-v\mathbf{e}_\eta)\cdot\frac{\partial\mathbf{e}_{SN}}{\partial\tau}+A_3}{(\mathbf{e}_\eta\cdot\mathbf{e}_{SN})(A_2+\rho c(A_1-1))}\right)\right|_{(\xi,1,\tau)} & \text{Eq. (4.88)}\end{array}\right], \tag{4.108}$$

$$\mathbf{g} = \begin{bmatrix} \left.\begin{matrix} \left(u - \frac{v_{BT}\frac{\partial r}{\partial \xi}}{\sqrt{\left(\frac{\partial r}{\partial \xi}\right)^2+\left(\frac{\partial z}{\partial \xi}\right)^2}} \right)\Big|_{(\xi,0,\tau)} \\ \left(w - \frac{v_{BT}\frac{\partial z}{\partial \xi}}{\sqrt{\left(\frac{\partial r}{\partial \xi}\right)^2+\left(\frac{\partial z}{\partial \xi}\right)^2}} \right)\Big|_{(\xi,0,\tau)} \end{matrix} \right\} \text{Eq. (4.72)} \\ \rho\left(\xi,1,\tau\right) - \frac{\delta_\infty(\xi,\tau)}{\delta_S(\xi,\tau)} \quad \text{Eq. (4.76)} \\ \left(\mathbf{v}_\infty \cdot \mathbf{e}_{ST} - \mathbf{v}\cdot\mathbf{e}_{ST}\right)|_{(\xi,1,\tau)} \quad \text{Eq. (4.73)} \\ \delta_S\left(\xi,\tau\right) - \frac{\gamma-1}{\gamma+1}\delta_\infty\left(\xi,\tau\right) + \frac{2\gamma}{(\gamma+1)\delta_\infty(\xi,\tau)} \quad \text{Eq. (4.74)} \\ p\left(\xi,1,\tau\right) - \frac{2}{\gamma+1}\delta_\infty^2\left(\xi,\tau\right) - \frac{\gamma-1}{\gamma+1} \quad \text{Eq. (4.75)} \\ \rho\left(0,\eta,\tau\right) - \rho\left(0,1,\tau\right)\left(\frac{p(0,\eta,\tau)}{p(0,1,\tau)}\right)^{1/\gamma} \quad \text{Eq. (4.105)} \\ u\left(0,\eta,\tau\right) \quad \text{Eq. (4.104)} \\ \left.\frac{\partial w}{\partial \xi}\right|_{(0,\eta,\tau)} \quad \text{Eq. (4.102)} \\ \left.\frac{\partial p}{\partial \xi}\right|_{(0,\eta,\tau)} \quad \text{Eq. (4.103)} \\ \left.\frac{\partial v}{\partial \xi}\right|_{(0,\tau)} \quad \text{Eq. (4.100)} \end{bmatrix}. \tag{4.109}$$

In Eqs. $(4.107 - 4.109)$ $\mathbf{y}\left(\xi,\eta,\tau\right) : \mathbb{R}^3 \rightarrow \mathbb{R}^{10}$ and $\mathbf{f}$:$\mathbb{R}^3 \rightarrow \mathbb{R}^{10}$ while $\mathbf{g}$:$\mathbb{R}^3 \rightarrow \mathbb{R}^{11}$. The functions $\mathbf{y}\left(\xi,\eta,\tau\right)$ and $\mathbf{f}$ contain six components which are time-dependent functions over the domain Ω with the remaining four components time-dependent functions defined for on S only. The equation $\frac{\partial \mathbf{y}}{\partial \tau} + \mathbf{f} = \mathbf{0}$ represents ten partial differential equations with ten unknowns and $\mathbf{g} = \mathbf{0}$ represents appropriate boundary conditions.

4.1.5 Numerical Solution Technique

In order to convert the system of partial differential and algebraic equations to a system of (DAEs), it is necessary to approximate the spatial derivatives $\frac{\partial \mathbf{y}}{\partial \xi}$, and $\frac{\partial \mathbf{y}}{\partial \eta}$ at grid points $\left(\xi_i,\eta_j\right)$, $i = 0,...,N$, $j = 0,...,M$. We choose to specify the grid in the computational domain, Fig. 4.2, according to the following Gauss-Lobatto

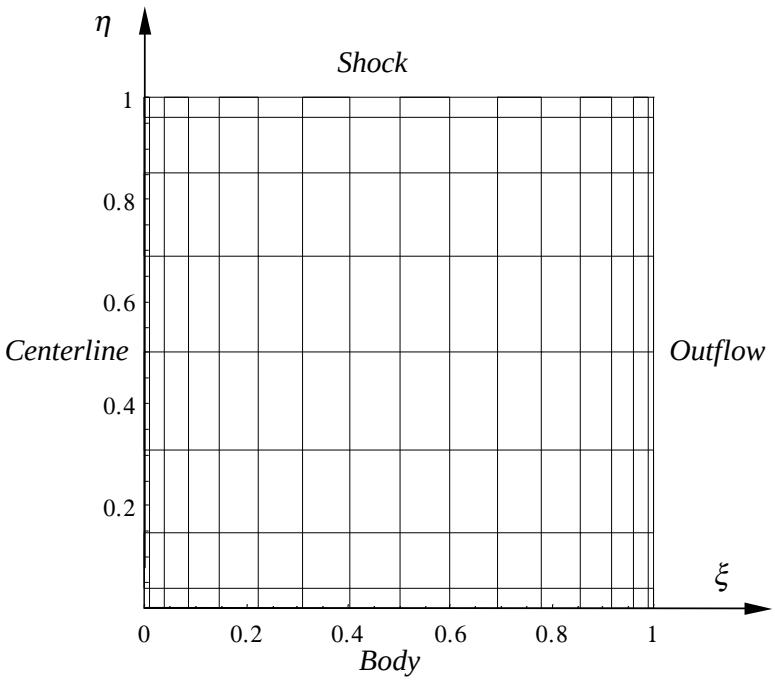

Figure 4.2. Gauss-Lobatto Chebyshev computational grid for the shock-fitted blunt body.

Chebyshev distribution

$$\xi_i = \frac{1}{2}\left(1 - \cos\left(\frac{\pi}{N}i\right)\right), \qquad i = 0, ..., N, \tag{4.110}$$
$$\eta_j = \frac{1}{2}\left(1 - \cos\left(\frac{\pi}{M}j\right)\right), \qquad j = 0, ..., M.$$

The functions $\mathbf{y}(\xi, \eta, \tau)$ are approximated in terms of a double Lagrange global interpolating polynomial defined on the mesh ξ_n, $n = 0, ..., N$, η_m, $m = 0, ..., M$, *i.e.*

$$\mathbf{y}(\xi, \eta, \tau) \approx \sum_{n=0}^{N}\sum_{m=0}^{M} \mathbf{y}(\xi_n, \eta_m, \tau) L_n^{(N)}(\xi) L_m^{(M)}(\eta). \tag{4.111}$$

Derivatives of $\mathbf{y}(\xi, \eta, \tau; b)$ are evaluated by differentiating Eq. (4.111). Evaluating these derivatives on the grid, (ξ_i, η_j), chosen to be the same grid as that used to define the interpolating polynomial, *i.e.* $(\xi_i, \eta_j) \equiv (\xi_n, \eta_m)$, and making use of

Eq. (3.17) yields the following approximations for the spatial derivatives of $\mathbf{y}$,

$$\left.\frac{\partial \mathbf{y}}{\partial \xi}\right|_{(\xi_i,\eta_j)} \approx \sum_{n=0}^{N} \mathbf{y}(\xi_n,\eta_j,\tau)\frac{dL_n}{d\xi}(\xi_i), \tag{4.112}$$
$$\left.\frac{\partial \mathbf{y}}{\partial \eta}\right|_{(\xi_i,\eta_j)} \approx \sum_{m=0}^{M} \mathbf{y}(\xi_i,\eta_m,\tau)\frac{dL_m}{d\eta}(\eta_j).$$

The metrics $\frac{\partial^2 z}{\partial \tau \partial \xi}$ and $\frac{\partial^2 r}{\partial \tau \partial \xi}$ in Eq. (4.90) are specified by differentiating Eq. (4.112) with respect to time, *i.e.*

$$\frac{\partial^2 z(\xi_i,\eta_j,\tau)}{\partial \tau \partial \xi} = \sum_{n=0}^{N} \frac{\partial}{\partial \tau} z(\xi_n,\eta_j,\tau)\frac{dL_n}{d\xi}(\xi_i), \tag{4.113}$$
$$\frac{\partial^2 r(\xi_i,\eta_j,\tau)}{\partial \tau \partial \xi} = \sum_{n=0}^{N} \frac{\partial}{\partial \tau} r(\xi_n,\eta_j,\tau)\frac{dL_n}{d\xi}(\xi_i).$$

After spatial discretization of Eqs. $(4.107 - 4.109)$ on an $(N+1)\times(M+1)$ grid, the equations reduce to the following system of P_2 (DAEs)

$$\frac{dy_p(\tau)}{d\tau} = f_p(y_1,...,y_{P_2},), \quad p = 1,...,P_1, \tag{4.114}$$

$$0 = g_p(y_1,...,y_{P_2}), \quad p = P_1+1,...,P_2, \tag{4.115}$$

with initial conditions

$$y_p(0) = y_{0p}, \quad p = 1,...,P_1, \tag{4.116}$$

consisting of $P_2 = 6(NM+N+M)+5$ total equations and equal number of unknowns. The system is composed of $P_1 = 6NM+2M$ ODEs and $P_2 - P_1 = 6N+4M+5$ algebraic equations, where the primary variables, $y_p(\tau)$, $p = 1,...,P_1$,

taken to be those whose time derivative explicitly appears in Eq. (4.114) are

$$y_p(\tau) = \begin{bmatrix} \left.\begin{matrix} \rho(\xi_i,\eta_j,\tau) \\ u(\xi_i,\eta_j,\tau) \\ w(\xi_i,\eta_j,\tau) \\ p(\xi_i,\eta_j,\tau) \end{matrix}\right\} \begin{matrix} i=1,...,N, \\ j=1,...,M-1, \end{matrix} \\ \left.\begin{matrix} r(\xi_i,\eta_j,\tau) \\ z(\xi_i,\eta_j,\tau) \end{matrix}\right\} \begin{matrix} i=0,...,N, \\ j=1,...,M, \end{matrix} \\ \left.\begin{matrix} v_{BT}(\xi_i,\tau) \\ \rho(\xi_i,0,\tau) \\ p(\xi_i,0,\tau) \\ v(\xi_i,\tau) \end{matrix}\right\} i=1,...,N, \end{bmatrix}, \; p=1,...,P_1, \tag{4.117}$$

and the secondary variables $y_p(\tau)$, $p = P_1+1,...,P_2$ are

$$y_p(\tau) = \begin{bmatrix} \left.\begin{matrix} u(\xi_i,0,\tau) \\ w(\xi_i,0,\tau) \\ \rho(\xi_i,1,\tau) \\ u(\xi_i,1,\tau) \\ w(\xi_i,1,\tau) \\ p(\xi_i,1,\tau) \end{matrix}\right\} i=1,...,N, \\ \left.\begin{matrix} \rho(0,\eta_j,\tau) \\ u(0,\eta_j,\tau) \\ w(0,\eta_j,\tau) \\ p(0,\eta_j,\tau) \end{matrix}\right\} j=0,...,M, \\ v(0,\tau) \end{bmatrix}, \; p=P_1+1,...,P_2. \tag{4.118}$$

The functions $f_p\left(y_1,...,y_{P_2}\right),\quad p=1,...,P_1$, are

$$f_p=\left[\begin{array}{c}
\left.\begin{array}{c}
\left(-\widehat{u}\frac{\partial\rho}{\partial\xi}-\widehat{w}\frac{\partial\rho}{\partial\eta}-\rho\left(\frac{\partial\xi}{\partial r}\frac{\partial u}{\partial\xi}+\frac{\partial\xi}{\partial z}\frac{\partial w}{\partial\xi}+\frac{\partial\eta}{\partial r}\frac{\partial u}{\partial\eta}+\frac{\partial\eta}{\partial z}\frac{\partial w}{\partial\eta}\right)-\frac{\rho u}{r}\right)\Big|_{(\xi_i,\eta_j,\tau)}\\
\left(-\widehat{u}\frac{\partial u}{\partial\xi}-\widehat{w}\frac{\partial u}{\partial\eta}-\frac{1}{\rho}\left(\frac{\partial\xi}{\partial r}\frac{\partial p}{\partial\xi}+\frac{\partial\eta}{\partial r}\frac{\partial p}{\partial\eta}\right)\right)\Big|_{(\xi_i,\eta_j,\tau)}\\
\left(-\widehat{u}\frac{\partial w}{\partial\xi}-\widehat{w}\frac{\partial w}{\partial\eta}-\frac{1}{\rho}\left(\frac{\partial\xi}{\partial z}\frac{\partial p}{\partial\xi}+\frac{\partial\eta}{\partial z}\frac{\partial p}{\partial\eta}\right)\right)\Big|_{(\xi_i,\eta_j,\tau)}\\
\left(-\widehat{u}\frac{\partial p}{\partial\xi}-\widehat{w}\frac{\partial p}{\partial\eta}-\gamma p\left(\frac{\partial\xi}{\partial r}\frac{\partial u}{\partial\xi}+\frac{\partial\xi}{\partial z}\frac{\partial w}{\partial\xi}+\frac{\partial\eta}{\partial r}\frac{\partial u}{\partial\eta}+\frac{\partial\eta}{\partial z}\frac{\partial w}{\partial\eta}\right)-\frac{\gamma pu}{r}\right)\Big|_{(\xi_i,\eta_j,\tau)}
\end{array}\right\}\ {\scriptstyle i=1,...,N,\ j=1,...,M-1,}\\
\left.\begin{array}{c}
\left.\frac{\eta\frac{dZ(\xi)}{d\xi}v(\xi,\tau)}{\sqrt{\left(\frac{dR(\xi)}{d\xi}\right)^2+\left(\frac{dZ(\xi)}{d\xi}\right)^2}}\right|_{(\xi_i,\eta_j,\tau)}\\
-\left.\frac{\eta\frac{dR(\xi)}{d\xi}v(\xi,\tau)}{\sqrt{\left(\frac{dR(\xi)}{d\xi}\right)^2+\left(\frac{dZ(\xi)}{d\xi}\right)^2}}\right|_{(\xi_i,\eta_j,\tau)}
\end{array}\right\}\ {\scriptstyle i=0,...,N,\ j=1,...,M,}\\
\left.\begin{array}{c}
-\left.\frac{\left(\widehat{u}\left(\frac{\partial\eta}{\partial r}\frac{\partial w}{\partial\xi}-\frac{\partial\eta}{\partial z}\frac{\partial u}{\partial\xi}\right)+\frac{1}{\rho}\left(\frac{\partial\eta}{\partial r}\frac{\partial\xi}{\partial z}-\frac{\partial\eta}{\partial z}\frac{\partial\xi}{\partial r}\right)\frac{\partial p}{\partial\xi}\right)}{\sqrt{\left(\frac{\partial\eta}{\partial z}\right)^2+\left(\frac{\partial\eta}{\partial r}\right)^2}}\right|_{(\xi_i,0,\tau)}\\
\left(-\frac{1}{c^2}\frac{\partial p}{\partial\tau}+\widehat{u}\left(\frac{\partial\rho}{\partial\xi}-\frac{1}{c^2}\frac{\partial p}{\partial\xi}\right)\right)\Big|_{(\xi_i,0,\tau)}\\
-\left(\frac{\rho c\widehat{u}\left(\frac{\partial\eta}{\partial r}\frac{\partial u}{\partial\xi}+\frac{\partial\eta}{\partial z}\frac{\partial w}{\partial\xi}\right)+c\left(\frac{\partial\eta}{\partial r}\frac{\partial\xi}{\partial r}+\frac{\partial\eta}{\partial z}\frac{\partial\xi}{\partial z}\right)\frac{\partial p}{\partial\xi}}{\sqrt{\left(\frac{\partial\eta}{\partial z}\right)^2+\left(\frac{\partial\eta}{\partial r}\right)^2}}\right.\\
-\rho c^2\left(\frac{\partial\xi}{\partial r}\frac{\partial u}{\partial\xi}+\frac{\partial\xi}{\partial z}\frac{\partial w}{\partial\xi}+\frac{\partial\eta}{\partial r}\frac{\partial u}{\partial\eta}+\frac{\partial\eta}{\partial z}\frac{\partial w}{\partial\eta}\right)\\
\left.+c\sqrt{\left(\frac{\partial\eta}{\partial z}\right)^2+\left(\frac{\partial\eta}{\partial r}\right)^2}\frac{\partial p}{\partial\eta}-\widehat{u}\frac{\partial p}{\partial\xi}-\frac{\rho c^2u}{r}\right)\Big|_{(\xi_i,0,\tau)}\\
-\left.\left(\frac{(A_2+\rho cA_1)(\mathbf{v}_\infty-v\mathbf{e}_\eta)\cdot\frac{\partial\mathbf{e}_{SN}}{\partial\tau}-\rho c(\mathbf{v}-v\mathbf{e}_\eta)\cdot\frac{\partial\mathbf{e}_{SN}}{\partial\tau}+A_3}{(\mathbf{e}_\eta\cdot\mathbf{e}_N)(A_2+\rho c(A_1-1))}\right)\right|_{(\xi_i,1,\tau)}
\end{array}\right\}\ i=1,...,N,
\end{array}\right]\tag{4.119}$$

and the functions $g_p\left(y_1,...,y_{P_2}\right),\quad p=P_1+1,...,P_2$, are

$$g_p=\left[\begin{array}{c}
\left.\left(u-\frac{v_{BT}\frac{\partial r}{\partial\xi}}{\sqrt{\left(\frac{\partial r}{\partial\xi}\right)^2+\left(\frac{\partial z}{\partial\xi}\right)^2}}\right)\right|_{(\xi_i,0,\tau)}\\
\left.\left(w-\frac{v_{BT}\frac{\partial z}{\partial\xi}}{\sqrt{\left(\frac{\partial r}{\partial\xi}\right)^2+\left(\frac{\partial z}{\partial\xi}\right)^2}}\right)\right|_{(\xi_i,0,\tau)}\\
\rho\left(\xi_i,1,\tau\right)-\frac{\delta_\infty(\xi_i,\tau)}{\delta_S(\xi_i,\tau)}\\
\left(\mathbf{v}_\infty\cdot\mathbf{e}_{ST}-\mathbf{v}\cdot\mathbf{e}_{ST}\right)\big|_{(\xi_i,1,\tau)}\\
\delta_S\left(\xi_i,\tau\right)-\frac{\gamma-1}{\gamma+1}\delta_\infty\left(\xi_i,\tau\right)+\frac{2\gamma}{(\gamma+1)\delta_\infty(\xi_i,\tau)}\\
p\left(\xi_i,1,\tau\right)-\frac{2}{\gamma+1}\delta_\infty^2\left(\xi_i,\tau\right)-\frac{\gamma-1}{\gamma+1}
\end{array}\right\}\ i=1,...,N,$$

$$\left.\begin{array}{c}
\rho\left(0,\eta_j,\tau\right)-\rho\left(0,1,\tau\right)\left(\frac{p(0,\eta_j,\tau)}{p(0,1,\tau)}\right)^{1/\gamma}\\
u\left(0,\eta_j,\tau\right)\\
\left.\frac{\partial w}{\partial\xi}\right|_{(0,\eta_j,\tau)}\\
\left.\frac{\partial p}{\partial\xi}\right|_{(0,\eta_j,\tau)}
\end{array}\right\}\ j=0,...,M,$$

$$\begin{array}{c}
\frac{\partial}{\partial\xi}v\left(0,\tau\right)
\end{array}\Bigg]\tag{4.120}$$

There are no equations for the grid points on the body since these are fixed in time, nor is there an equation for the tangential velocity on the body at the centerline since this quantity is redundant, the velocity components, $u(0,\eta_j,\tau)$, $w(0,\eta_j,\tau)$, already being specified by Eqs. (4.102) and (4.104).

As a final step Eq. (4.120) is now written such that the secondary variables y_p, $p=P_1+1,...,P_2$, can be solved explicitly as a function of the primary variables y_p, $p=1,...,P_1$, *i.e.*

$$y_p\left(\tau\right)=\widehat{g}_p\left(y_1,...,y_{P_1}\right),\quad p=P_1+1,...,P_2.\tag{4.121}$$

Making use of Eq. (4.112) yields the following expression for $w\left(0,\eta_j,\tau\right)$,

$$w\left(0,\eta_j,\tau\right)=\frac{\sum_{n=1}^{N}w(\xi_n,\eta_j,\tau)\frac{dL_n}{d\xi}(0)}{\frac{dL_0}{d\xi}(0)};\tag{4.122}$$

similar expressions are found for $p\left(0,\eta_j,\tau\right)$, and $v\left(0,\tau\right)$. Eqs. (4.73) and (4.74) are reformulated into the following two equations for the quantities $u\left(\xi_i,1,\tau\right)$ and $w\left(\xi_i,1,\tau\right)$, $i=1,...,N$,

$$u\left(\xi_i,1,\tau\right)=\left.\left(\frac{\frac{\partial z}{\partial\xi}\frac{\partial r}{\partial\xi}\sqrt{\gamma}\mathcal{M}_\infty}{\left(\frac{\partial z}{\partial\xi}\right)^2+\left(\frac{\partial r}{\partial\xi}\right)^2}+\frac{\frac{\partial z}{\partial\xi}\left(\delta_S+\left(\mathbf{e}_\eta\cdot\mathbf{e}_{SN}\right)v\right)}{\sqrt{\left(\frac{\partial z}{\partial\xi}\right)^2+\left(\frac{\partial r}{\partial\xi}\right)^2}}\right)\right|_{(\xi_i,1,\tau)}, \tag{4.123}$$

$$w\left(\xi_i,1,\tau\right)=\left.\left(\frac{\left(\frac{\partial z}{\partial\xi}\right)^2\sqrt{\gamma}\mathcal{M}_\infty}{\left(\frac{\partial z}{\partial\xi}\right)^2+\left(\frac{\partial r}{\partial\xi}\right)^2}-\frac{\frac{\partial r}{\partial\xi}\left(\delta_S+\left(\mathbf{e}_\eta\cdot\mathbf{e}_{SN}\right)v\right)}{\sqrt{\left(\frac{\partial z}{\partial\xi}\right)^2+\left(\frac{\partial r}{\partial\xi}\right)^2}}\right)\right|_{(\xi_i,1,\tau)}.$$

Once the quantities, $w\left(0,\eta_j,\tau\right)$, $p\left(0,\eta_j,\tau\right)$, $z\left(0,\eta_j,\tau\right)$, and $v\left(0,\tau\right)$ are found from Eq. (4.122) and $u\left(\xi_i,1,\tau\right)$ and $w\left(\xi_i,1,\tau\right)$ are found from Eq. (4.123), all the secondary variables can be expressed as explicit functions of the primary variables

where

$$\widehat{g}_p = \left[\begin{array}{c}
\left.\left(\frac{v_{BT}\frac{\partial r}{\partial \xi}}{\sqrt{\left(\frac{\partial r}{\partial \xi}\right)^2+\left(\frac{\partial z}{\partial \xi}\right)^2}}\right)\right|_{(\xi_i,0,\tau)} \\
\left.\left(\frac{v_{BT}\frac{\partial z}{\partial \xi}}{\sqrt{\left(\frac{\partial r}{\partial \xi}\right)^2+\left(\frac{\partial z}{\partial \xi}\right)^2}}\right)\right|_{(\xi_i,0,\tau)} \\
\frac{\delta_\infty(\xi_i,\tau)}{\delta_S(\xi_i,\tau)} \\
\left.\left(\frac{\frac{\partial z}{\partial \xi}\frac{\partial r}{\partial \xi}\sqrt{\gamma}\mathcal{M}_\infty}{\left(\frac{\partial z}{\partial \xi}\right)^2+\left(\frac{\partial r}{\partial \xi}\right)^2}+\frac{\frac{\partial z}{\partial \xi}(\delta_S+(\mathbf{e}_\eta\cdot\mathbf{e}_{SN})v)}{\sqrt{\left(\frac{\partial z}{\partial \xi}\right)^2+\left(\frac{\partial r}{\partial \xi}\right)^2}}\right)\right|_{(\xi_i,1,\tau)} \\
\left.\left(\frac{\left(\frac{\partial z}{\partial \xi}\right)^2\sqrt{\gamma}\mathcal{M}_\infty}{\left(\frac{\partial z}{\partial \xi}\right)^2+\left(\frac{\partial r}{\partial \xi}\right)^2}-\frac{\frac{\partial r}{\partial \xi}(\delta_S+(\mathbf{e}_\eta\cdot\mathbf{e}_{SN})v)}{\sqrt{\left(\frac{\partial z}{\partial \xi}\right)^2+\left(\frac{\partial r}{\partial \xi}\right)^2}}\right)\right|_{(\xi_i,1,\tau)} \\
\frac{2}{\gamma+1}\delta_\infty^2(\xi_i,\tau)+\frac{\gamma-1}{\gamma+1}
\end{array}\right\} i=1,...,N,$$

$$\left.\begin{array}{c}
\left.\left(\rho(0,1,\tau)\left(\frac{\sum_{n=1}^N p(\xi_n,\eta_j,\tau)\frac{dL_n}{d\xi}(0)}{p(0,1,\tau)\frac{dL_0}{d\xi}(0)}\right)^{1/\gamma}\right)\right|_{(0,\eta_j,\tau)} \\
0 \\
\frac{\sum_{n=1}^N w(\xi_n,\eta_j,\tau)\frac{dL_n}{d\xi}(0)}{\frac{dL_0}{d\xi}(0)} \\
\frac{\sum_{n=1}^N p(\xi_n,\eta_j,\tau)\frac{dL_n}{d\xi}(0)}{\frac{dL_0}{d\xi}(0)} \\
\frac{\sum_{n=1}^N v(\xi_n,\tau)\frac{dL_n}{d\xi}(0)}{\frac{dL_0}{d\xi}(0)}
\end{array}\right\} j=0,...,M, \quad (4.124)$$

where $\delta_S(\xi_i,\tau) = \frac{\gamma-1}{\gamma+1}\delta_\infty(\xi_i,\tau) - \frac{2\gamma}{(\gamma+1)\delta_\infty(\xi_i,\tau)}$. The system of DAEs in Eqs. (4.114) and (4.115) are converted into the following system of P_1 ODEs,

$$\frac{dx_p(\tau)}{d\tau} = h_p(x_1,...,x_{P_1}), \quad p=1,...,P_1, \quad (4.125)$$

where

$$h_p(x_1,...,x_{P_1}) \equiv f_p(y_1,...,y_{P_1},\widehat{g}_q(y_1,...,y_{P_1})), \quad \begin{array}{c} p=1,...,P_1, \\ q=P_1+1,...,P_2, \end{array} \quad (4.126)$$

and

$$x_p(\tau) = y_p(\tau), \quad p=1,...,P_1. \quad (4.127)$$

The system of Eqs. (4.114) and (4.115) can finally be expressed in the standard form for a system of ODEs,

$$\frac{d\mathbf{x}}{d\tau} = \mathbf{h}\left(\mathbf{x}\right), \tag{4.128}$$

with accompanying initial conditions

$$\mathbf{x}\left(0\right) = \mathbf{x}_0, \tag{4.129}$$

where

$$\mathbf{x}_0 = \left(x_1\left(0\right), ..., x_{P_1}\left(0\right)\right)^T. \tag{4.130}$$

The initial conditions for the shock distance, $h\left(\xi_i, \tau\right)$, are taken to be constant, *i.e.*, $h\left(\xi_i, \tau\right) = h\left(0, \tau\right) = 0.25$, $i = 1, ..., N$, which is sufficient to set initial conditions for the remainder of the physical grid coordinates, $r(\xi_i, \eta_j, \tau)$, $z(\xi_i, \eta_j, \tau)$, $i = 0, ..., N$, $j = 0, ..., M$, by making use of Eqs. (4.34) and (4.35). The shock velocity, $v(\xi_i, \tau)$, $i = 0, ..., N$, is initially set to zero. The initial values for the variables, $\rho\left(\xi_i, \eta_j, \tau\right)$, $u\left(\xi_i, \eta_j, \tau\right)$, $w\left(\xi_i, \eta_j, \tau\right)$, $p\left(\xi_i, \eta_j, \tau\right)$, $i = 1, ..., N$, $j = 1, ..., M$, $\rho(\xi_i, 0, \tau)$, $u(\xi_i, 0, \tau)$, and $p(\xi_i, 0, \tau)$, $i = 1, ..., N$, are set equal to the value behind the shock at $(\eta = 1)$ for the corresponding ξ coordinate line, *e.g.* $\rho(\xi_i, \eta_j, 0) = \rho(\xi_i, 1, 0)$. The initial values for $u(\xi_i, 0, \tau)$, $i = 1, ..., N$, are chosen so that the boundary condition at $\eta = 0$, Eq. (4.50) is satisfied exactly, and the initial values for $\rho\left(0, \eta_j, \tau\right)$, $u\left(0, \eta_j, \tau\right)$, $w\left(0, \eta_j, \tau\right)$, $p\left(0, \eta_j, \tau\right)$, $j = 0, ..., M$, are chosen so that the boundary conditions at $\xi = 0$, Eqs. $(4.102 - 4.105)$ are satisfied exactly. The initial values for the variables $v_{BT}(\xi_i, \tau)$ $i = 1, ..., N$, are prescribed once the values for $r(\xi_i, 0, \tau)$, $z(\xi_i, 0, \tau)$, $u(\xi_i, 0, \tau)$ and $w(\xi_i, 0, \tau)$ have been specified.

Solutions have been obtained for the system of ODEs, Eqs. (4.125), with the standard ODE solver LSODA, [52, 53], which automatically adjusts the time step and order of accuracy of the method to achieve a specified level of accuracy. It also automatically switches between an explicit method and implicit method depending

on the stiffness of the problem. Because the bulk of our problems have been stable, it was possible to use a simple Runge-Kutta technique with a CFL number of 0.3, so as to resolve the fastest acoustic time scales. In general, however, the CFL criteria is not sufficient for maintaining stability of the numerical solution. The criteria for determining that steady state has been reached is when the change in the variables y_p, $p = 1, ..., P_1$, from one time step to the next drops below a threshold level of 10^{-15} or ceases to show any further decrease in error over a period of $\tau = 1$.

4.2 Pseudospectral Flow Solver Verification and Validation

4.2.1 Supersonic Cone Flow

The solution to supersonic flow over a cone, or Taylor-Maccoll solution [54], will be used to verify the code described in the previous section. Details of the derivation can be found in Appendix G. A highly accurate ODE solver was used to generate solutions to the Taylor-Maccoll flow, which will be subsequently referred to as the exact solution. The only modification to the blunt body problem formulation to generate pseudospectral approximations to the Taylor-Maccoll flow is a replacement of the centerline boundary condition at $\xi = 0$ with a Dirichlet boundary condition containing the values of ρ, u, w, p, r, and z from the exact solution in order to avoid the problem of the geometric singularity at $\xi = 0$. A schematic of a 40 degree cone in $\mathcal{M}_\infty = 3.5$ flow including the physical and computational coordinates is shown in Figure 4.3 for a 5×5 grid. For the initial conditions, ρ, u, w, p, r, and z are taken from the exact solution with a sinusoidal perturbation in the shock velocity, *i.e.* $v(\xi, 0) = 0.1 \sin(2\pi\xi)$. Figure 4.4, is the time history of the $L_\infty[\Omega]$ error in $\rho(\xi, \eta)$ over the domain, Ω, for the pseudospectral prediction measured against the exact solution for a $\mathcal{M}_\infty = 3.5$ flow over a 40 degree cone solved on a 5×17 grid. The figure demonstrates a rapid relaxation to the exact solution.

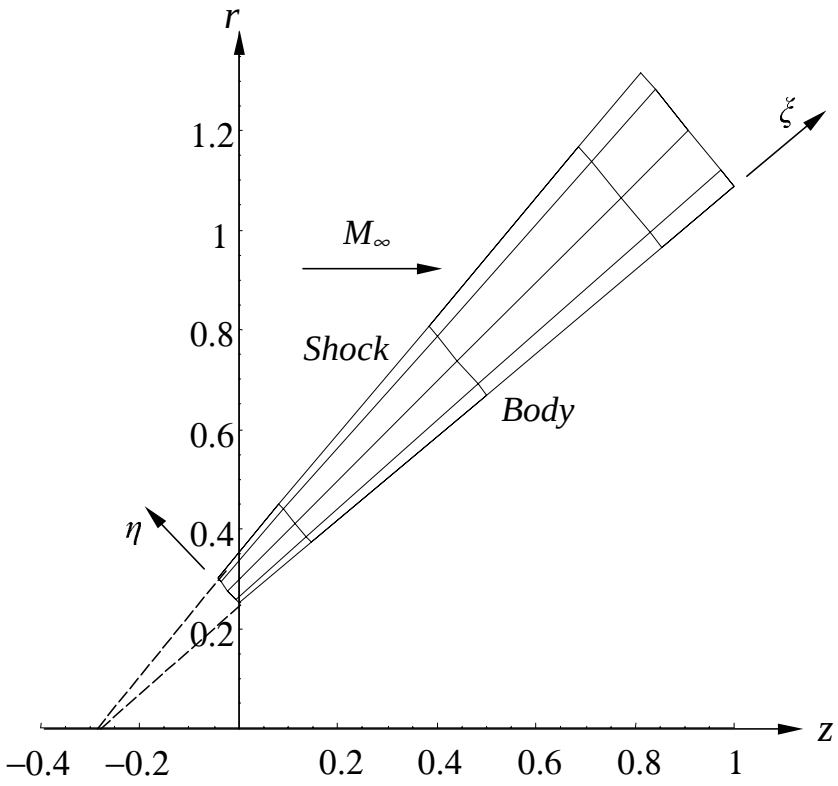

Figure 4.3. Schematic of the physical (r, z) and computational (ξ, η) grids for the Taylor-Maccoll problem.

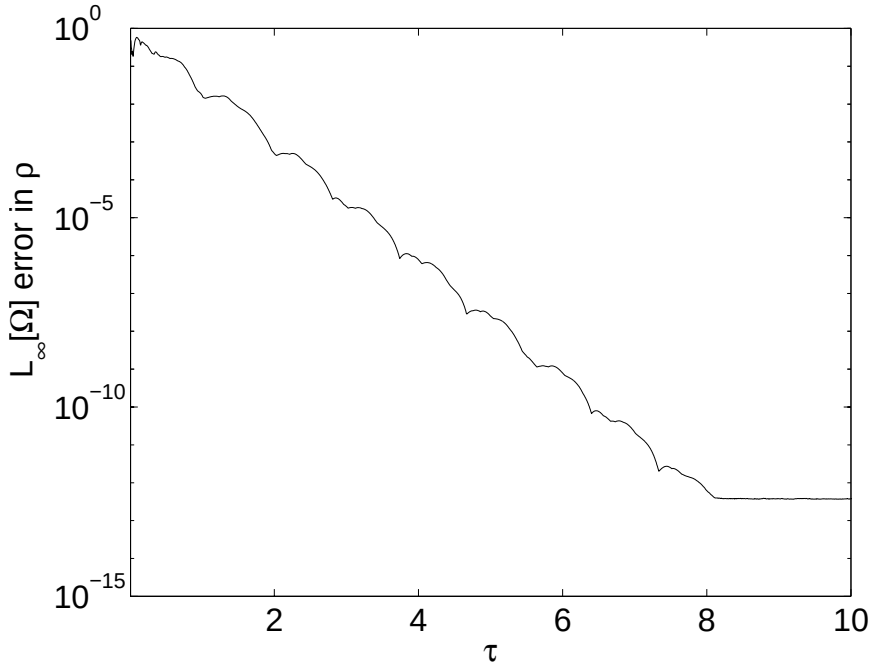

Figure 4.4. Single 5×17 grid $L_\infty[\Omega]$ residual error in $\rho\,(\xi,\eta)$ measured against Taylor-Maccoll similarity solution as a function of time, τ, for a 40^o cone at $\mathcal{M}_\infty = 3.5$ and $\Delta t = 0.0005$.

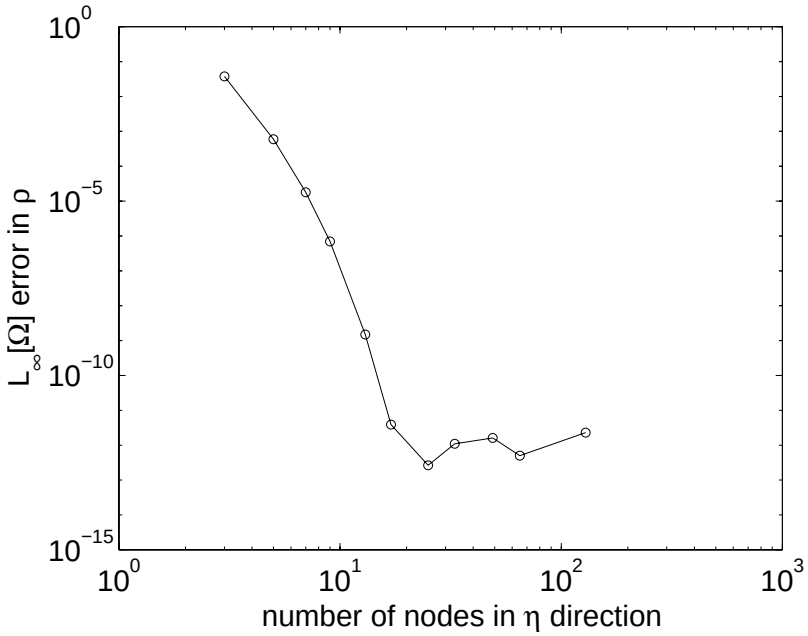

Figure 4.5. $L_\infty[\Omega]$ error in $\rho\,(\xi,\eta)$ measured against a Taylor-Maccoll similarity solution for a 40^o cone in $\mathcal{M}_\infty = 3.5$ flow as grid is refined in the η direction.

A grid convergence test for the pseudospectral prediction of the Taylor-Maccoll flow is conducted by refining the grid in the $\eta-$ direction for a fixed number of five nodes in the $\xi-$direction. The accuracy of the method is unaffected by grid refinement in the $\xi-$ direction since all derivatives are zero in that direction. As we can see from Figure 4.5, there is a rapid decrease in the error until about 10^{-12} when the error flattens probably due to roundoff error. Note the spectral nature of the grid convergence, that is the slope of the error curve continues to steepen with increasing number of nodes, at least until the roundoff limit is reached, and does not reach a constant value for the slope as would be the case for a method with a fixed order of accuracy.

4.2.2 Supersonic Blunt Body Flow

Further verification and validation of the pseudospectral solver is performed by generating approximate solutions to the blunt body problem. Contours of Mach number, pressure, entropy with the velocity vector field, and the single nonzero component of vorticity, ω_θ, are shown in Figs. 4.6-4.9 for the case of $\mathcal{M}_\infty = 3.5$, generated on a 17×9 grid. The sonic line, $\mathcal{M} = 1$, can be identified in Fig. 4.6, and it is observed that the outflow velocity is indeed supersonic as required in the derivation of the outflow boundary condition. In the plot of contours of pressure, Fig. 4.7, pressure at the stagnation point is seen to be more than sixteen times the freestream pressure at $\mathcal{M}_\infty = 3.5$, and the jump in pressure across the normal shock at the centerline is over thirteen times the freestream pressure. Despite such a large discontinuity in pressure, the flow field is accurately resolved by the shock fitting method. The entropy contour plot, Fig. 4.8, shows generation of entropy at the shock where the entropy jump across the shock is a function of the shock angle with respect to the freestream flow. The maximum change in entropy occurs at the centerline where the shock is normal to the freestream flow. The velocity field is overlaid on the entropy contours to show that the entropy is constant along streamlines since the curved shock is the only mechanism for entropy generation in this problem. A grid refinement study was performed to verify that the entropy remained constant along streamlines downstream of the shock and it was found that as the grid was refined $\mathbf{v} \cdot \nabla s \rightarrow 0$, which is consistent with the inviscid form of the entropy equation, Eq. (F.20), in the limit of steady state. The contour plot of vorticity, Figure 4.9, shows that the vorticity is not zero throughout the flow field. Vorticity is generated at the shock boundary due to the curvature of the shock and then convected downstream. The vorticity undergoes a change along streamlines via compressibility effects and non-barotropic effects according to Eq. (4.20).

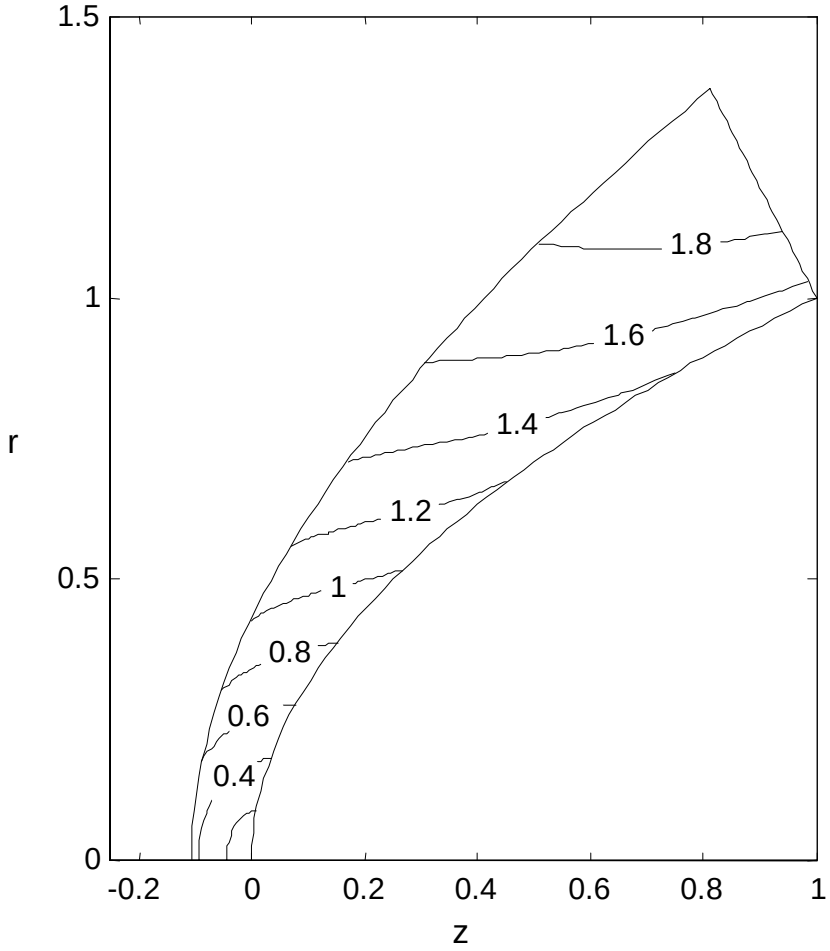

Figure 4.6. Contours of Mach number for flow over the blunt body for $b = 0.5$, $\mathcal{M}_\infty = 3.5$, 17×9 grid.

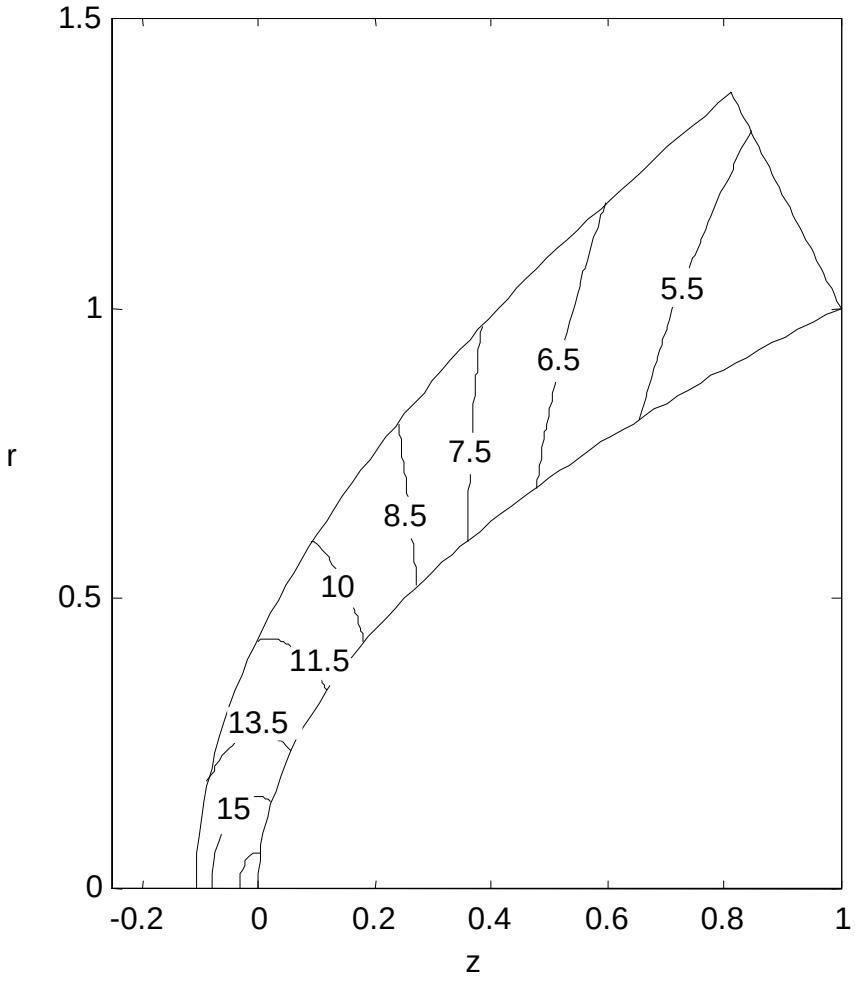

Figure 4.7. Contours of pressure for flow over the blunt body for $b = 0.5$, $\mathcal{M}_\infty = 3.5$, 17×9 grid.

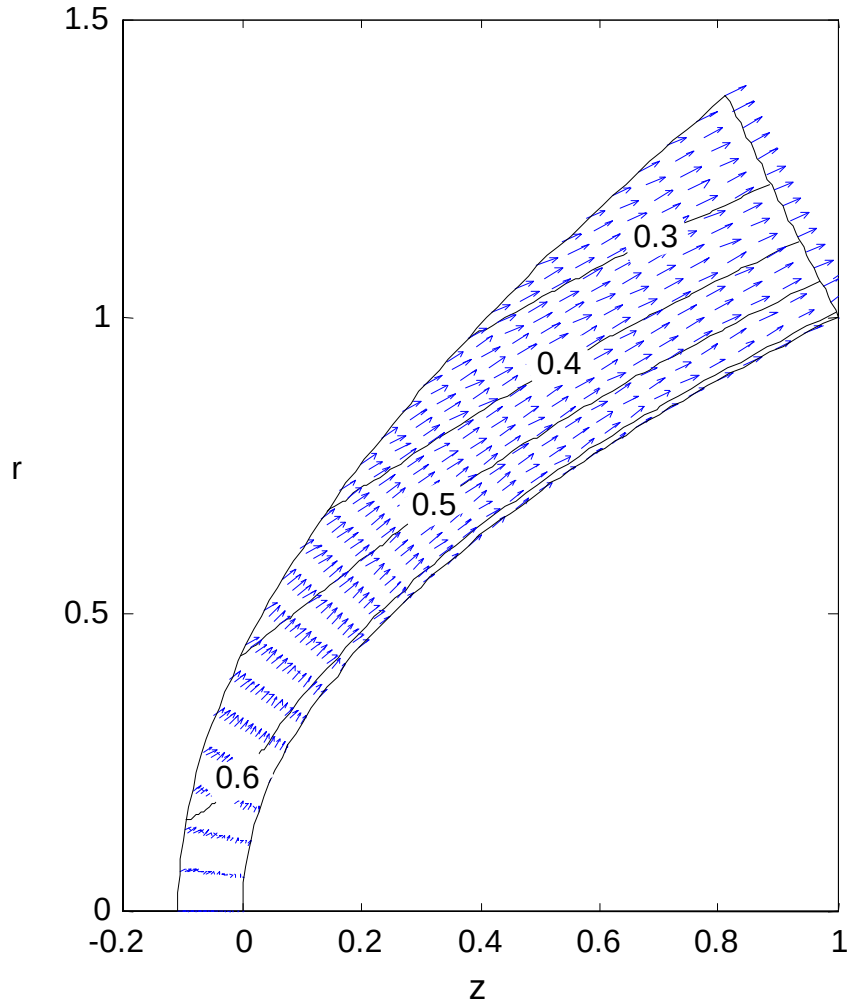

Figure 4.8. Contours of entropy with velocity vectors for flow over the blunt body for $b = 0.5$, $\mathcal{M}_\infty = 3.5$, 17×9 grid.

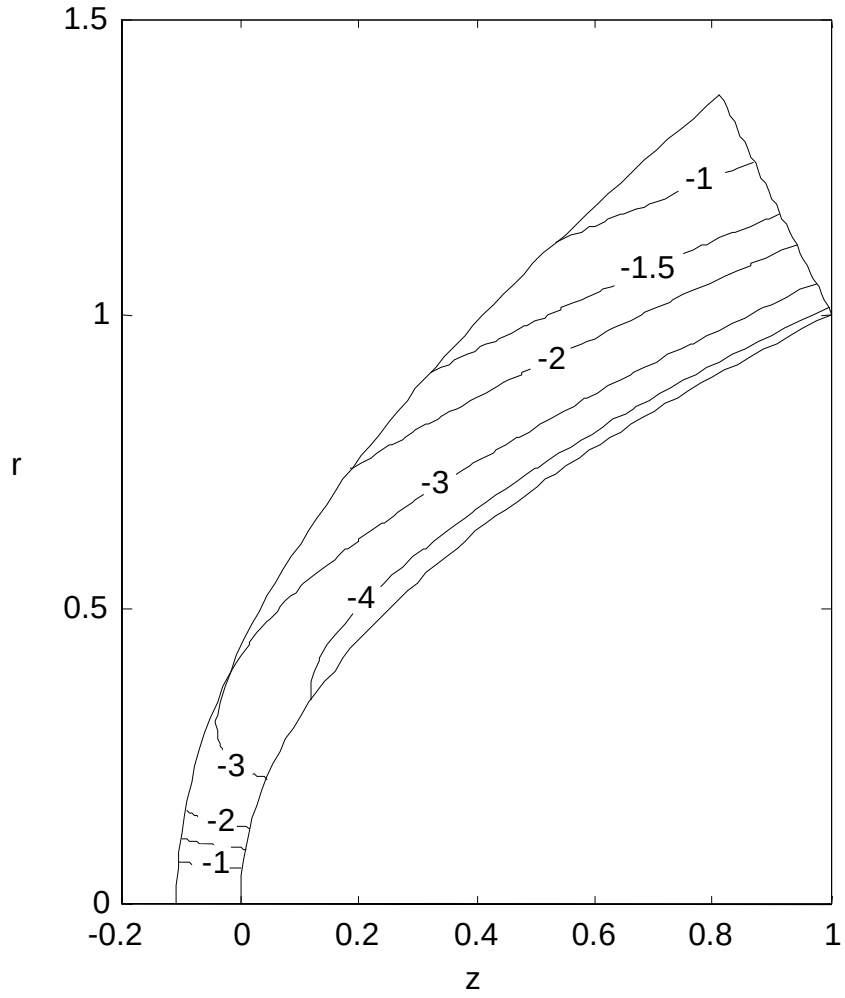

Figure 4.9. Contours of vorticity for flow over the blunt body for $b = 0.5$, $\mathcal{M}_\infty = 3.5$, 17×9 grid.

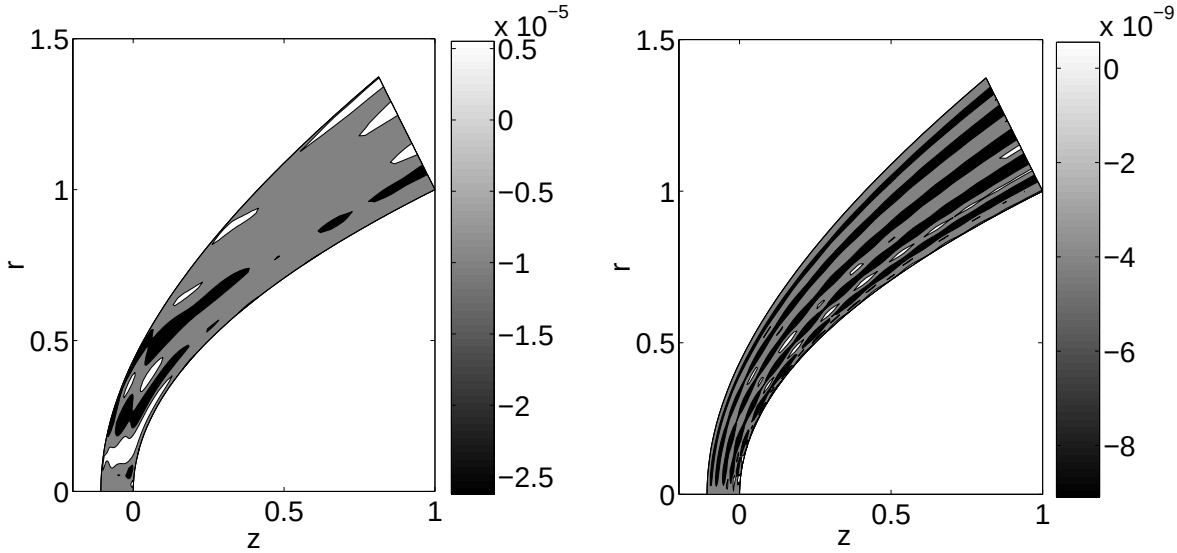

(a) 17×9 grid (b) 29×15 grid

Figure 4.10. Contours of $h_o - h_{o\infty}$ for flow over the blunt body for $b = 0.5$, $\mathcal{M}_\infty = 3.5$, and two grid resolutions: 17×9 and 29×15.

Grid refinement tests verified that the pseudospectral flow solutions satisfied the condition of constant stagnation enthalpy. Contours of $h_o - h_{o\infty}$ for a 17×9 grid and a 29×15 grid solution are shown in Fig. 4.10, from which it is evident that $(h_o - h_{o\infty}) \to 0$ as the grid is refined, where $h_{o\infty}$ is the freestream stagnation enthalpy. Grid refinement tests also verified that both Crocco's theorem, Eq. 4.17, and the steady state form of the vorticity transport equation, Eqs. 4.22 and 4.23, were satisfied.

As a means of code validation for the blunt body, a comparison is made between the numerical results for the pressure distribution on the body with that of the modified Newtonian [55] sine squared law,

$$C_p|_{Newtonian} = C_{po} \sin^2 \phi, \tag{4.131}$$

where C_{po} is the pressure coefficient at the body stagnation point and ϕ is the local surface inclination angle measured with respect to the z axis. The pressure

coefficient, C_p is defined as

$$C_p = \frac{p^* - p^*_\infty}{\frac{1}{2}\rho^*_\infty w^{*2}_\infty} = \frac{p\left(\xi, 0, \tau\right) - 1}{\frac{1}{2}\gamma \mathcal{M}^2_\infty}. \tag{4.132}$$

The modified Newtonian approximation is a semi-analytical model for the surface pressure distribution over blunt bodies. Anderson [56] reports that for a power law body with $b = 0.5$ and aspect ratio near unity, the modified Newtonian approximation does well in predicting the pressure distribution on the surface of the body. As can be seen from Fig. 4.11, the pseudospectral code also predicts close agreement for the pressure distribution on the surface of the body defined by $r = \sqrt{z}$. As a further check on the validity of the pseudospectral code, in Fig. 4.12 a comparison is made of the pseudospectral prediction for the shock shape for $\mathcal{M}_\infty = 3.5$ flow over a sphere with that of an empirical formula by Billig [57] developed for flow over spherically blunted cones based on experiment.

A grid convergence study is performed for the blunt body with the $L_\infty[\Omega]$ error over the domain, Ω in $\rho\left(\xi, \eta\right)$ shown in Fig. 4.13, at $\mathcal{M}_\infty = 3.5$ and $b = 0.5$, where the error is measured against a 65×33 or 2145 node numerical solution. For 861 nodes, the $L_\infty[\Omega]$ error over the domain, Ω in $\rho\left(\xi, \eta\right)$ has been reduced to the order of 10^{-12} and subsequently flattens due to roundoff error. Like grid convergence plots for the Taylor-Maccoll solution, the convergence of the error for the blunt body problem shows a spectral convergence rate as expected of the pseudospectral numerical technique.

4.3 Blunt Body Karhunen-Loève Modes

Ten solutions, also referred to as snapshots in the context of the KL method, are generated for ten different values of $\mathcal{M}_\infty$ chosen uniformly in the range $\mathcal{M}_\infty \in [3, 4]$, with the geometric parameter b fixed at 0.5. From these ten snapshots, ten KL

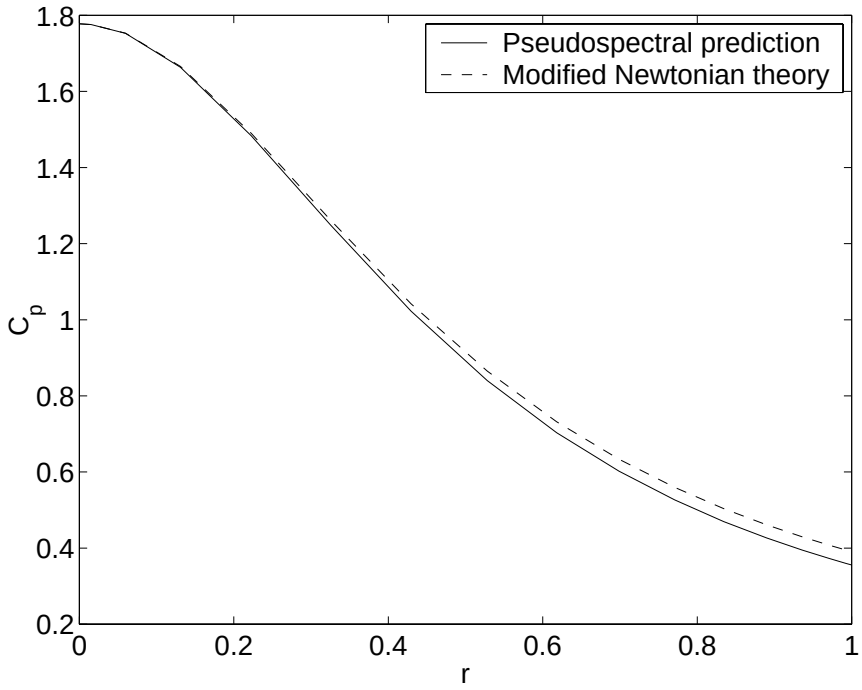

Figure 4.11. Blunt body surface C_p distribution predictions at $\mathcal{M}_\infty = 3.5$ from modified Newtonian theory and from the pseudospectral method, where $b = 0.5$; 17×9 grid.

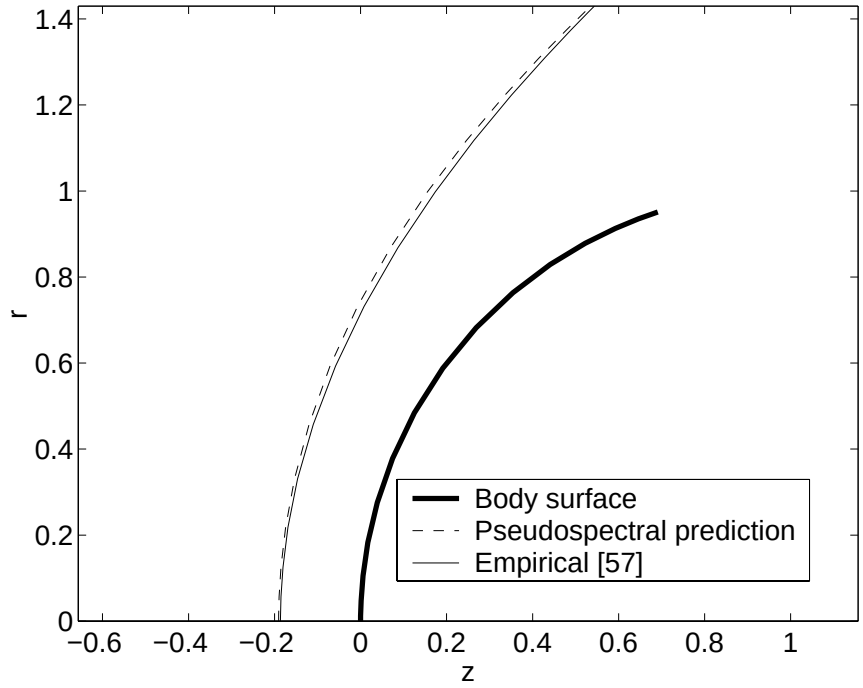

Figure 4.12. Shock shape prediction of the pseudospectral code for a sphere $\mathcal{M}_\infty = 3.5$ compared with an empirical formula [57] derived from experiments; 17×9 grid.

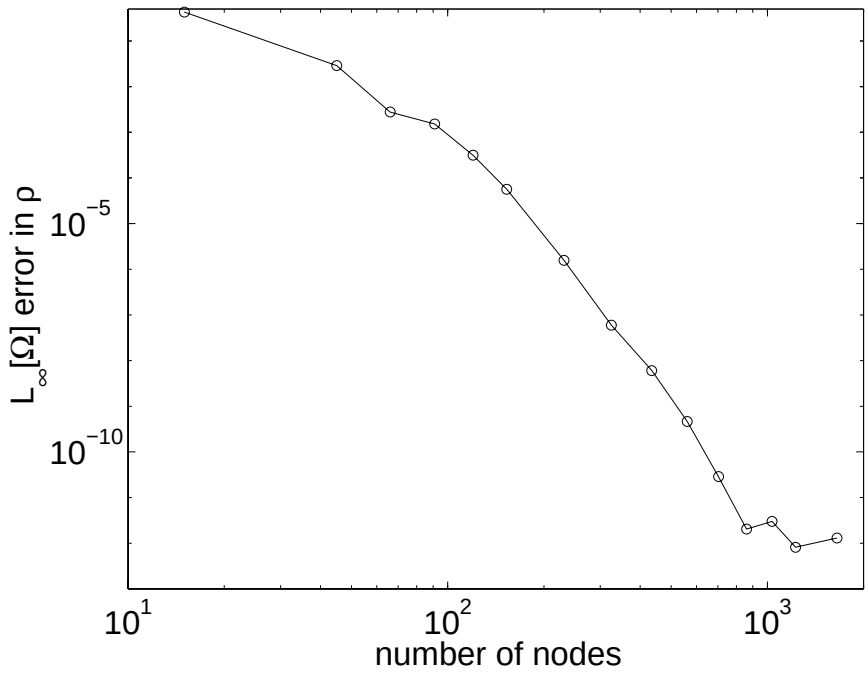

Figure 4.13. Grid convergence $L_\infty[\Omega]$ error in $\rho\,(\xi, \eta)$ measured against a baseline, 65×33 grid, solution for a $b = 0.5$, $\mathcal{M}_\infty = 3.5$ blunt body.

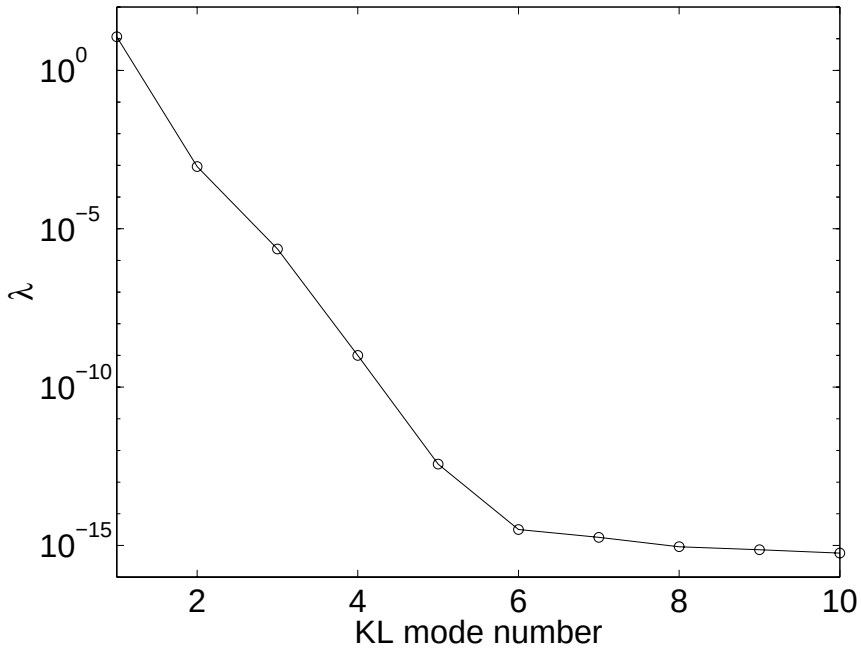

Figure 4.14. Eigenvalues of density for ten snapshots over the range $\mathcal{M}_\infty \in [3, 4]$.

modes, φ_k^q and associated eigenvalues λ_k^q, $k = 1, ..., 10$, $q = 1, ..., 6$, are calculated for each of the primitive variables, ρ, u, w, and p and the physical coordinates r and z, where subscripts indicate the number of the mode and superscripts dictate to which variable the KL modes and eigenvalues belong. The method of snapshots, Eqs. (A.25) and (A.23), was used to generate the KL modes and eigenvalues. A plot of the eigenvalues of density as a function of KL mode number are shown in Fig. 4.14 while the ten normalized KL modes are shown in Fig. 4.15. A rapid decay in the magnitude of the eigenvalues, and a progressively richer topologically structured set of KL modes is observed as the mode number increases.

4.4 Least-Squares Method

In the KL least-squares method, the steady state density, $\widetilde{\rho}\,(\xi, \eta)$, r and z velocity components, $\widetilde{u}\,(\xi, \eta)$ and $\widetilde{w}\,(\xi, \eta)$ respectively, pressure, $\widetilde{p}\,(\xi, \eta)$, and physical grid

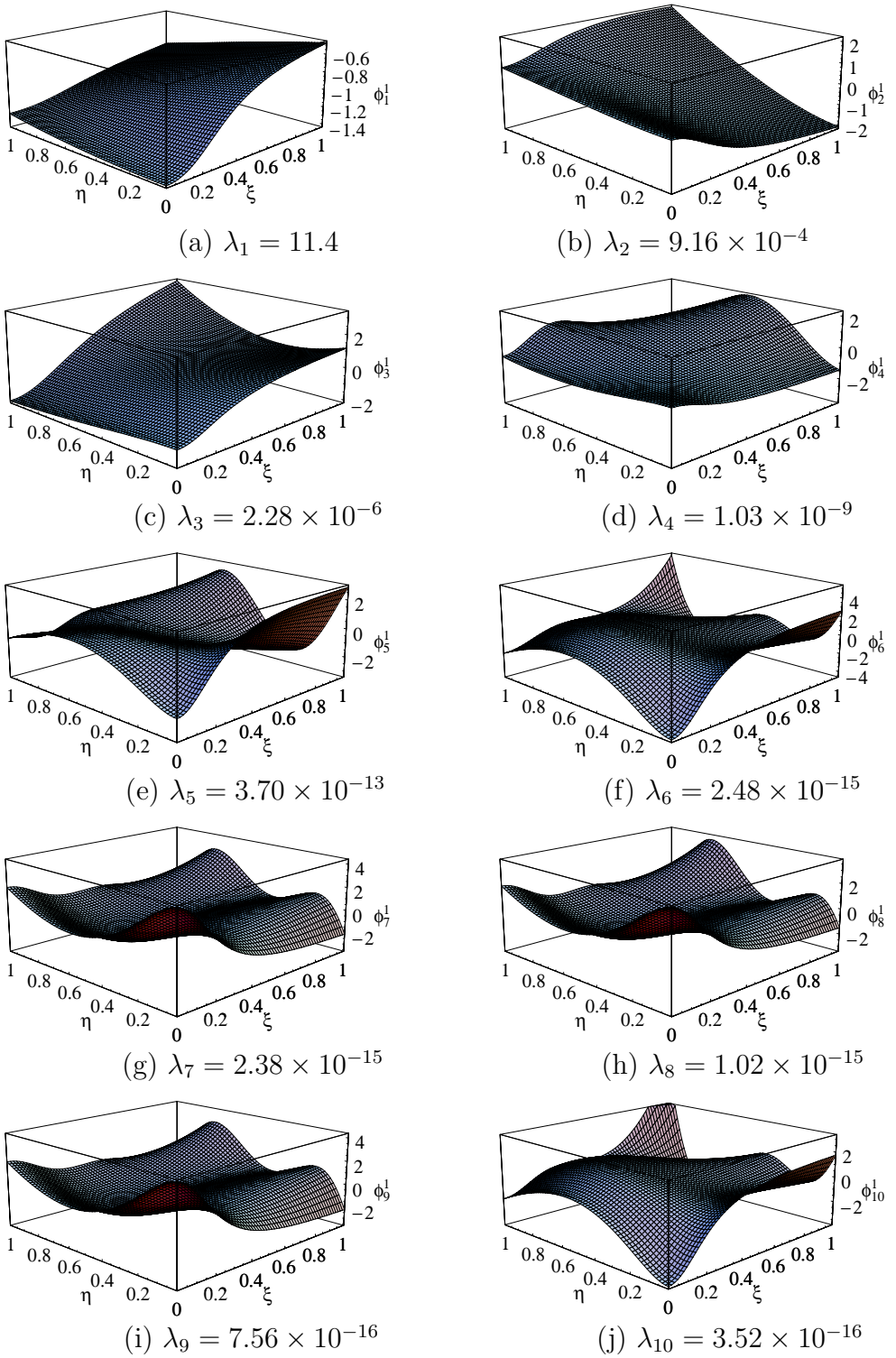

(a) $\lambda_1 = 11.4$ (b) $\lambda_2 = 9.16 \times 10^{-4}$

(c) $\lambda_3 = 2.28 \times 10^{-6}$ (d) $\lambda_4 = 1.03 \times 10^{-9}$

(e) $\lambda_5 = 3.70 \times 10^{-13}$ (f) $\lambda_6 = 2.48 \times 10^{-15}$

(g) $\lambda_7 = 2.38 \times 10^{-15}$ (h) $\lambda_8 = 1.02 \times 10^{-15}$

(i) $\lambda_9 = 7.56 \times 10^{-16}$ (j) $\lambda_{10} = 3.52 \times 10^{-16}$

Figure 4.15. Ten KL eigenmodes of density with associated eigenvalues, λ, generated from ten snapshots in the range $\mathcal{M}_\infty \in [3, 4]$.

coordinates $\widetilde{r}(\xi,\eta)$ and $\widetilde{z}(\xi,\eta)$ are approximated in terms of the KL modes as follows,

$$\begin{array}{l}
\widetilde{\rho}(\xi,\eta)=\sum_{k=1}^{K}a_k^1\varphi_k^1(\xi,\eta)\\
\widetilde{u}(\xi,\eta)=\sum_{k=1}^{K}a_k^2\varphi_k^2(\xi,\eta)\\
\widetilde{w}(\xi,\eta)=\sum_{k=1}^{K}a_k^3\varphi_k^3(\xi,\eta)\\
\widetilde{p}(\xi,\eta)=\sum_{k=1}^{K}a_k^4\varphi_k^4(\xi,\eta)\\
\widetilde{r}(\xi,\eta)=\sum_{k=1}^{K}a_k^5\varphi_k^5(\xi,\eta)\\
\widetilde{z}(\xi,\eta)=\sum_{k=1}^{K}a_k^6\varphi_k^6(\xi,\eta)
\end{array}. \tag{4.133}$$

Employing Eq. (4.133) , the KL least-squares formulation of the blunt body problem is written in the form of Eqs. (2.14) and (2.15) where

$$\widetilde{\mathbf{y}}(\xi,\eta)=\begin{bmatrix}\widetilde{\rho}(\xi,\eta)\\ \widetilde{u}(\xi,\eta)\\ \widetilde{w}(\xi,\eta)\\ \widetilde{p}(\xi,\eta)\\ \widetilde{r}(\xi,\eta)\\ \widetilde{z}(\xi,\eta)\end{bmatrix}, \tag{4.134}$$

$$\widehat{\mathbf{f}}\left(\widetilde{\mathbf{y}},\frac{\partial\widetilde{\mathbf{y}}}{\partial\xi},\frac{\partial\widetilde{\mathbf{y}}}{\partial\eta}\right)=\begin{bmatrix}
\widehat{\widetilde{u}}\frac{\partial\widetilde{u}}{\partial\xi}+\widehat{\widetilde{w}}\frac{\partial\widetilde{u}}{\partial\eta}+\frac{1}{\widetilde{\rho}}\left(\frac{\partial\xi}{\partial\widetilde{r}}\frac{\partial\widetilde{p}}{\partial\xi}+\frac{\partial\eta}{\partial\widetilde{r}}\frac{\partial\widetilde{p}}{\partial\eta}\right)\\
\widehat{\widetilde{u}}\frac{\partial\widetilde{w}}{\partial\xi}+\widehat{\widetilde{w}}\frac{\partial\widetilde{w}}{\partial\eta}+\frac{1}{\widetilde{\rho}}\left(\frac{\partial\xi}{\partial\widetilde{z}}\frac{\partial\widetilde{p}}{\partial\xi}+\frac{\partial\eta}{\partial\widetilde{z}}\frac{\partial\widetilde{p}}{\partial\eta}\right)\\
\widehat{\widetilde{u}}\frac{\partial p}{\partial\xi}-\widehat{\widetilde{w}}\frac{\partial p}{\partial\eta}-\gamma\widetilde{p}\left(\frac{\partial\xi}{\partial\widetilde{r}}\frac{\partial\widetilde{u}}{\partial\xi}+\frac{\partial\xi}{\partial\widetilde{z}}\frac{\partial\widetilde{w}}{\partial\xi}+\frac{\partial\eta}{\partial\widetilde{r}}\frac{\partial\widetilde{u}}{\partial\eta}+\frac{\partial\eta}{\partial\widetilde{z}}\frac{\partial\widetilde{w}}{\partial\eta}\right)-\frac{\gamma\widetilde{p}\widetilde{u}}{\widetilde{r}}\\
\widehat{\widetilde{u}}\frac{\partial\widetilde{\rho}}{\partial\xi}-\widehat{\widetilde{w}}\frac{\partial\widetilde{\rho}}{\partial\eta}-\widetilde{\rho}\left(\frac{\partial\xi}{\partial\widetilde{r}}\frac{\partial\widetilde{u}}{\partial\xi}+\frac{\partial\xi}{\partial\widetilde{z}}\frac{\partial\widetilde{w}}{\partial\xi}+\frac{\partial\eta}{\partial\widetilde{r}}\frac{\partial\widetilde{u}}{\partial\eta}+\frac{\partial\eta}{\partial\widetilde{z}}\frac{\partial\widetilde{w}}{\partial\eta}\right)-\frac{\widetilde{\rho}\widetilde{u}}{\widetilde{r}}
\end{bmatrix}, \tag{4.135}$$

and

$$\widehat{\mathbf{g}}\left(\widetilde{\mathbf{y}},\frac{\partial\widetilde{\mathbf{y}}}{\partial\xi},\frac{\partial\widetilde{\mathbf{y}}}{\partial\eta}\right)=\begin{bmatrix}\widetilde{v}_{BN}\left(\xi\right)\\ \left(\mathbf{v}_{\infty}\cdot\widetilde{\mathbf{e}}_{ST}-\widetilde{\mathbf{v}}\cdot\widetilde{\mathbf{e}}_{ST}\right)\big|_{(\xi,1)}\\ \left(\widetilde{\delta}-\frac{\gamma-1}{\gamma+1}\widetilde{\delta}_{\infty}+\frac{2\gamma}{(\gamma+1)\widetilde{\delta}_{\infty}}\right)\Big|_{(\xi,1)}\\ \left(\widetilde{p}-\frac{2}{\gamma+1}\widetilde{\delta}_{\infty}^{2}-\frac{\gamma-1}{\gamma+1}\right)\Big|_{(\xi,1)}\\ \left(\widetilde{\rho}-\frac{\widetilde{\delta}_{\infty}}{\widetilde{\delta}}\right)\Big|_{(\xi,1)}\\ \widetilde{\rho}\left(0,\eta,\tau\right)-\widetilde{\rho}\left(0,1,\tau\right)\left(\frac{\widetilde{p}(0,\eta,\tau)}{\widetilde{p}(0,1,\tau)}\right)^{1/\gamma}\\ \widetilde{r}\left(\xi,0\right)-r\left(\xi,0\right)\\ \widetilde{z}\left(\xi,0\right)-z\left(\xi,0\right)\end{bmatrix}, \tag{4.136}$$

where

$$\widetilde{\delta}=\widetilde{\mathbf{v}}\cdot\widetilde{\mathbf{e}}_{SN}|_{(\xi,1)}\,, \tag{4.137}$$

$$\widetilde{\delta}_{\infty}=\mathbf{v}_{\infty}\cdot\widetilde{\mathbf{e}}_{SN}|_{(\xi,1)}\,, \tag{4.138}$$

$$\widetilde{v}_{BN}\left(\xi\right)=\left(\widetilde{u}\frac{\partial\widetilde{z}}{\partial\xi}-\widetilde{w}\frac{\partial\widetilde{r}}{\partial\xi}\right)\Big|_{(\xi,0)}, \tag{4.139}$$

$$\widehat{\widetilde{u}}=\widetilde{u}\frac{\partial\xi}{\partial\widetilde{r}}+\widetilde{w}\frac{\partial\xi}{\partial\widetilde{z}}, \tag{4.140}$$

$$\widehat{\widetilde{w}}=\widetilde{u}\frac{\partial\eta}{\partial\widetilde{r}}+\widetilde{w}\frac{\partial\eta}{\partial\widetilde{z}}. \tag{4.141}$$

The approximate metric terms $\frac{\partial\xi}{\partial\widetilde{r}}$, $\frac{\partial\xi}{\partial\widetilde{z}}$, $\frac{\partial\eta}{\partial\widetilde{r}}$, and $\frac{\partial\eta}{\partial\widetilde{z}}$ are found from the inverse metrics in Eq. (4.31) and the relations in Eq. (4.133), *e.g.* $\frac{\partial\xi}{\partial\widetilde{r}}=-\frac{1}{J}\frac{\partial\widetilde{z}}{\partial\eta}$. The spatial derivatives in Eq. (4.135) are calculated by taking derivatives of the quantities in Eq. (4.133), *e.g.*

$$\frac{\partial}{\partial\xi}\widetilde{\rho}\left(\xi,\eta\right)=\sum_{k=1}^{K}a_{k}^{1}\frac{\partial}{\partial\xi}\varphi_{k}^{1}\left(\xi,\eta\right),\quad\frac{\partial}{\partial\eta}\widetilde{\rho}\left(\xi,\eta\right)=\sum_{k=1}^{K}a_{k}^{1}\frac{\partial}{\partial\eta}\varphi_{k}^{1}\left(\xi,\eta\right). \tag{4.142}$$

The terms $\widetilde{\mathbf{e}}_{ST}$, and $\widetilde{\mathbf{e}}_{SN}$ in Eqs. $(4.136-4.138)$ are found by substituting the KL approximations for the metrics $\frac{\partial\eta}{\partial\widetilde{r}}$, and $\frac{\partial\eta}{\partial\widetilde{z}}$ into Eqs. (4.80) and (4.81). In Eq. (4.136), the coordinates $r\left(\xi,0\right)$ and $z\left(\xi,0\right)$ are specified from the choice of b which fixes the

body surface via the parameterization in Eqs. (4.46) and (4.47) . The linear boundary conditions in Eq. $(4.102-4.104)$, $\left.\frac{\partial w}{\partial \xi}\right|_{(0,\eta,\tau)}=0$, $\left.\frac{\partial p}{\partial \xi}\right|_{(0,\eta,\tau)}=0$, $u|_{(0,\eta,\tau)}=0$, Eq. (4.101) , $\left.\frac{\partial z}{\partial \xi}\right|_{(0,\eta,\tau)}=0$, and $r|_{(0,\eta,\tau)}=0$ are not included in Eq. (4.136) since each of the KL modes satisfies them exactly; this is apparent upon noting that the KL modes are linear combinations of the snapshots from Eq. (A.23). In addition, at steady state we have $v(\xi,\tau)=0$, so that the evolution equations for physical grid coordinates and the equation for the shock velocity in Eqs. (4.43), (4.44) and (4.88) are not considered. The physical grid coordinates over the domain Ω are included implicitly in the functions $\widehat{\mathbf{f}}$ and $\widehat{\mathbf{g}}$ through the metrics, and explicitly in the last two components of $\widehat{\mathbf{g}}$ at the body surface, $\eta=0$.

We define the following error functions over the domain Ω

$$e_f^q=\widehat{f^q},\quad q=1,...,4, \tag{4.143}$$

where $\widehat{f^q}$ is the q^{th} component of the function $\widehat{\mathbf{f}}$. At the boundary S, the error function is defined as:

$$e_g^q=\widehat{g}^q,\quad q=1,...,8, \tag{4.144}$$

where $\widehat{g}^q$ is the q^{th} component of $\widehat{\mathbf{g}}$. A total error, e, is formed from Eqs. (4.143) and (4.144) as follows

$$e=\sum_{q=1}^{4}\int_{\Omega}\omega_f^q\sqrt{e_f^q e_f^q}d\Omega+\sum_{q=1}^{8}\int_{S}\omega_g^q\sqrt{e_g^q e_g^q}dS, \tag{4.145}$$

where $\omega_f^q=\omega_g^q=1$, $q=1,...,3$, $\omega_f^4=\omega_g^4=0.1$, $\omega_g^5=\omega_g^6=1$, and $\omega_g^7=\omega_g^8=1000$ are constant weights chosen empirically to enhance convergence to a global minimum for e. The coefficients in Eq. (4.133) are chosen via a Newton method such that the total error, e defined in Eq. (4.145) , is minimized.

4.5 Results for Karhunen-Loève Least-Squares Model for Supersonic Blunt Body Flow

4.5.1 Karhunen-Loève Mode Convergence for Ten Snapshot KL Model, $\mathcal{M}_\infty \in [3,4]$, $b = 1/2$

Convergence of the $L_\infty[\Omega]$ error in $\rho(\xi,\eta)$ as a function of the number of KL modes is shown in Figure 4.16 for a KL model built from ten snapshots. The ten snapshots are uniformly distributed over the range $\mathcal{M}_\infty \in [3,4]$, while the geometry is fixed at $b = 0.5$. The snapshots are generated using the pseudospectral solver described in [39] on both a 17×9 grid and a 22×12 grid. The error is assessed by comparison with a highly resolved 33×17 grid solution. After the fourth mode for the 17×9 grid KL model and after the fifth mode for the 22×12 grid KL model there is no further improvement in the accuracy of the model, since the KL model accuracy has reached the level of error in the samples as shown by the dark lines in Figure 4.16.

The distribution of $L_\infty[\Omega]$ error in $\rho(\xi,\eta)$ for the KL model over the entire range, $\mathcal{M}_\infty \in [3,4]$, is shown in Figure 4.17 for the KL model built from ten 17×9 grid pseudospectral snapshots. Once again, the $L_\infty[\Omega]$ error in $\rho(\xi,\eta)$ decreases with increasing number of KL modes until the approximate accuracy of the samples is reached around 5×10^{-5}. Once the accuracy of the snapshots has been reached, there is no further improvement in the accuracy with increasing number of KL modes, since the higher order modes do not contain relevant information; they are corrupted by numerical error in the KL modes. For finer grid solutions than the 22×12 grid, the KL model accuracy became very sensitive to the ω_f^q in Eq. (4.145); therefore, the 22×12 grid KL model is the finest grid KL model employed in the current work.

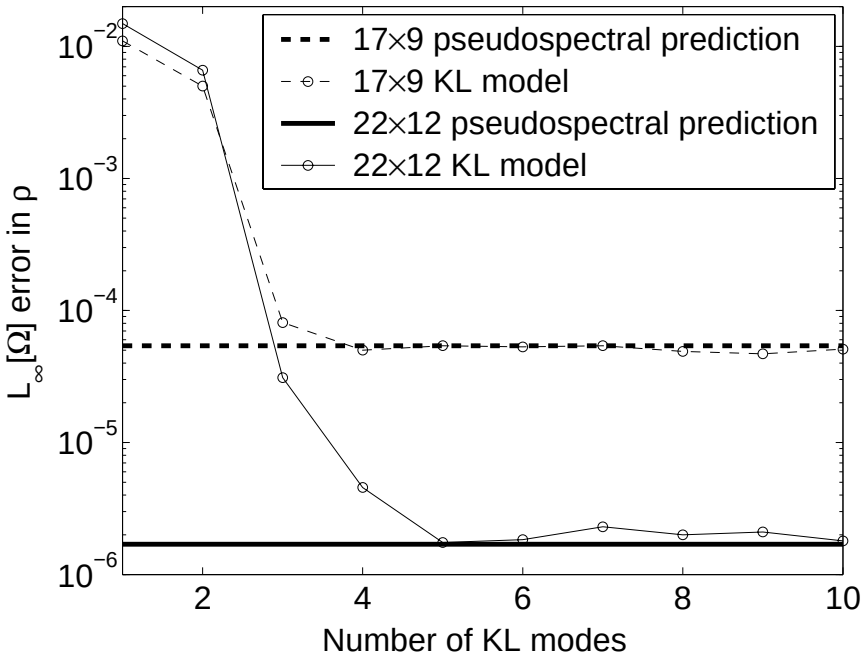

Figure 4.16. KL model $L_\infty[\Omega]$ error in ρ for both a 17×9 and 22×12 grid, $\mathcal{M}_\infty = 3.5, b = 0.5$. Errors determined by comparison to highly resolved 33×17 grid.

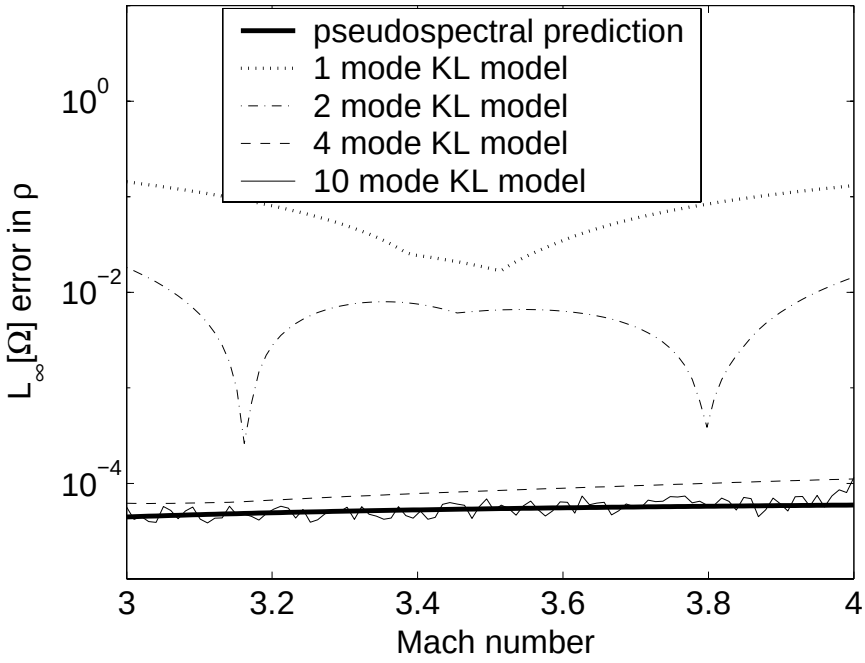

Figure 4.17. KL model $L_\infty[\Omega]$ error in ρ for a 17×9 grid, $\mathcal{M}_\infty \in [3, 4]$, $b = 0.5$. Errors determined by comparison to highly resolved 33×17 grid.

4.5.2 Single Variable Design Problem

To illustrate the use of a KL model for an optimal design problem, the power law body described parametrically in Eqs. (4.46) and (4.47) is considered, and the value of b is sought which minimizes the drag coefficient, C_D for fixed freestream Mach number, $\mathcal{M}_\infty = 3.5$, and ratio of specific heats, $\gamma = \frac{7}{5}$. For the axisymmetric problem, the equation for $C_D(b)$ is

$$C_D(b) = \frac{4}{\gamma \mathcal{M}_\infty^2} \int_0^1 pr \frac{\partial r}{\partial \xi}\bigg|_{\eta=0} d\xi. \tag{4.146}$$

The integral in Eq. (4.146) is evaluated by using Gauss quadrature to achieve high accuracy in C_D comparable to the accuracy in p and r from Eq. (4.146).

Before finding the value of b which minimizes C_D from Eq. (4.146), a KL model is built with ten uniformly spaced snapshots that span the design space in which the minimum is expected, that is $b \in [1/3, 1/2]$ for $\mathcal{M}_\infty = 3.5$. Here the snapshots are generated using the pseudospectral solver on a 17×9 grid. A plot of the eigenvalues of density as a function of KL mode number is shown in Figure 4.18 while the ten normalized KL modes are shown in Figure 4.19. There is a rapid decrease in the magnitude of the eigenvalues, and the KL modes become topologically richer as the mode number increases. A convergence plot of the $L_\infty[\Omega]$ error in $\rho(\xi, \eta)$ with respect to the number of KL modes is shown in Figure 4.20, where the error is measured against a highly resolved 33×17 grid solution of the pseudospectral solver. After the fourth mode there is no further improvement in the accuracy of the model, since the KL model accuracy has reached the level of error in the samples.

The distribution of $L_\infty[\Omega]$ error in $\rho(\xi, \eta)$ for the KL model over the entire range, $b \in [1/3, 1/2]$ is shown in Figure 4.21. Once again, the $L_\infty[\Omega]$ error decreases with increasing number of KL modes until the approximate accuracy of the samples is reached around 5×10^{-5}. Once the accuracy of the snapshots has been reached,

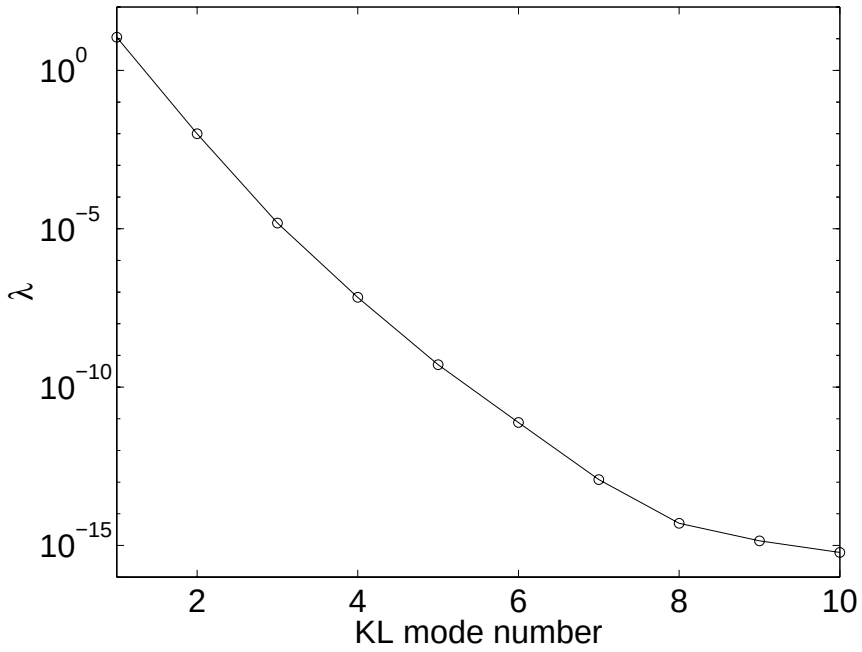

Figure 4.18. Eigenvalues of density for ten snapshots over the range $b \in [1/3, 1/2]$.

there is no further improvement in the accuracy with increasing number of KL modes, since the higher order modes do not contain relevant information; they are corrupted by numerical error in the KL modes.

Since we are interested in the drag coefficient, C_D, in Figure 4.22, we show the error convergence in C_D as a function of number of KL modes in the model over the range of geometric parameter $b \in [1/3, 1/2]$. The KL model was built from ten snapshots distributed uniformly over the range $b \in [1/3, 1/2]$; the snapshots were solved on a 17×9 grid. Again, the error is measured against a highly resolved 33×17 grid solution of the pseudospectral solver. It is seen that the error in the KL model is higher than the error in the pseudospectral solver over part of the range of b and lower over another part even with all ten modes used in the KL model. It may be that there is fortuitous cancelling of errors in the process of integrating to find C_D which over part of the range of b favors the pseudospectral method and

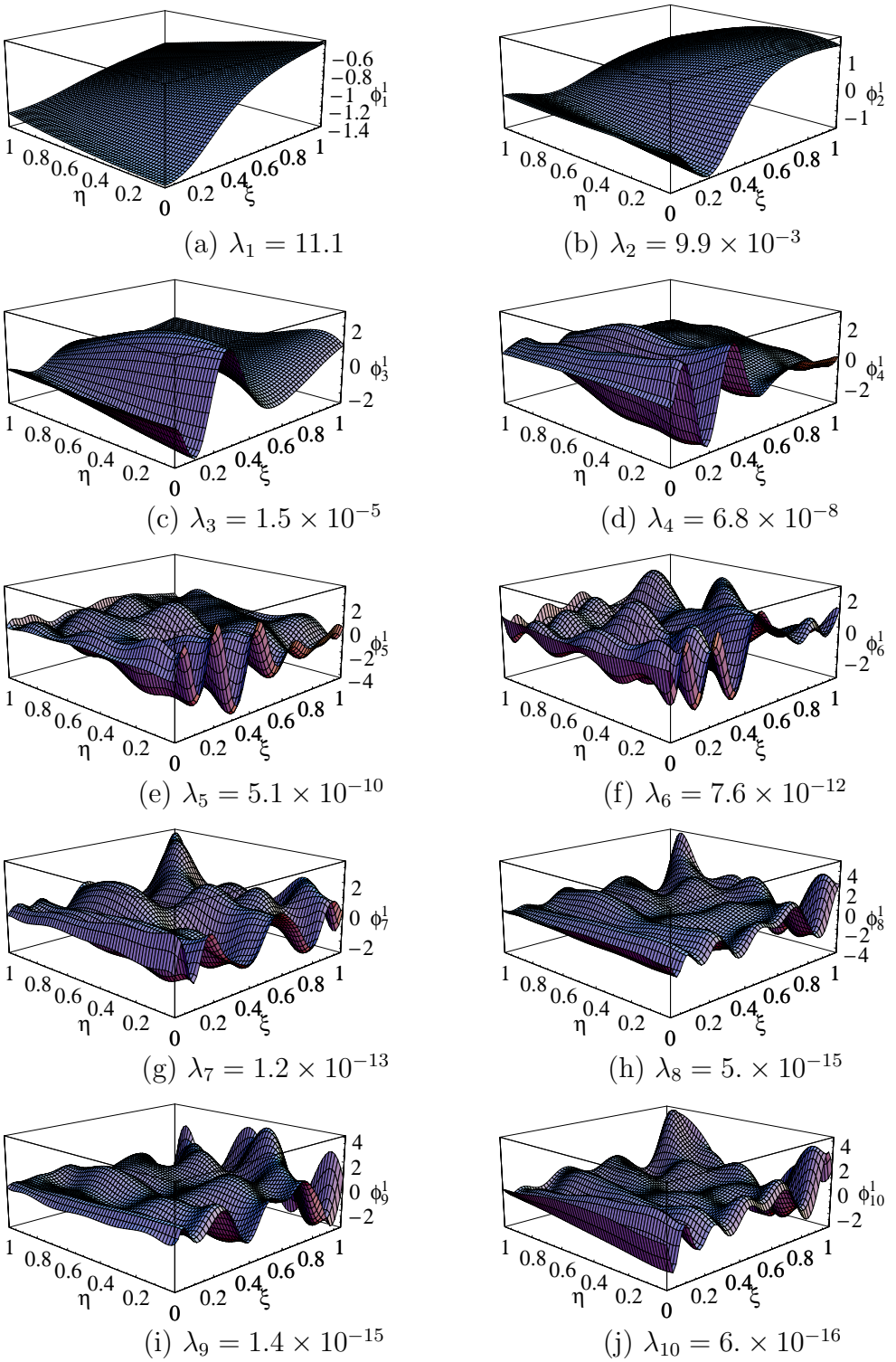

Figure 4.19. Ten KL eigenmodes of density with associated eigenvalues, λ, generated from ten snapshots in the range $b \in [1/3, 1/2]$.

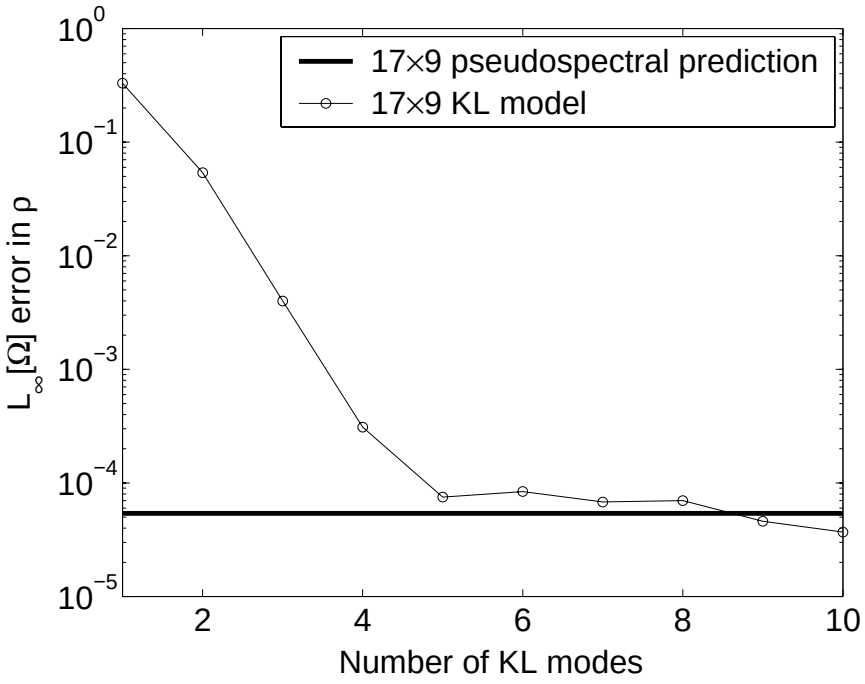

Figure 4.20. KL model $L_\infty[\Omega]$ error in ρ for a 17×9 grid, $\mathcal{M}_\infty = 3.5, b = 0.5$. Errors determined by comparison to highly resolved 33×17 grid.

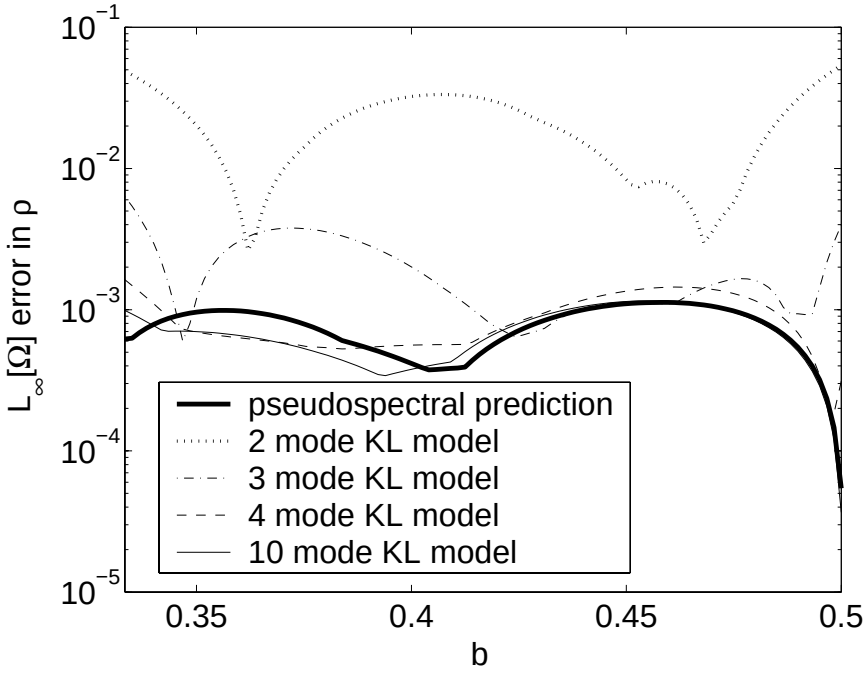

Figure 4.21. KL model $L_\infty[\Omega]$ error in ρ for a 17×9 grid, $b \in [1/3, 1/2]$, $\mathcal{M}_\infty = 3.5$. Errors determined by comparison to highly resolved 33×17 grid.

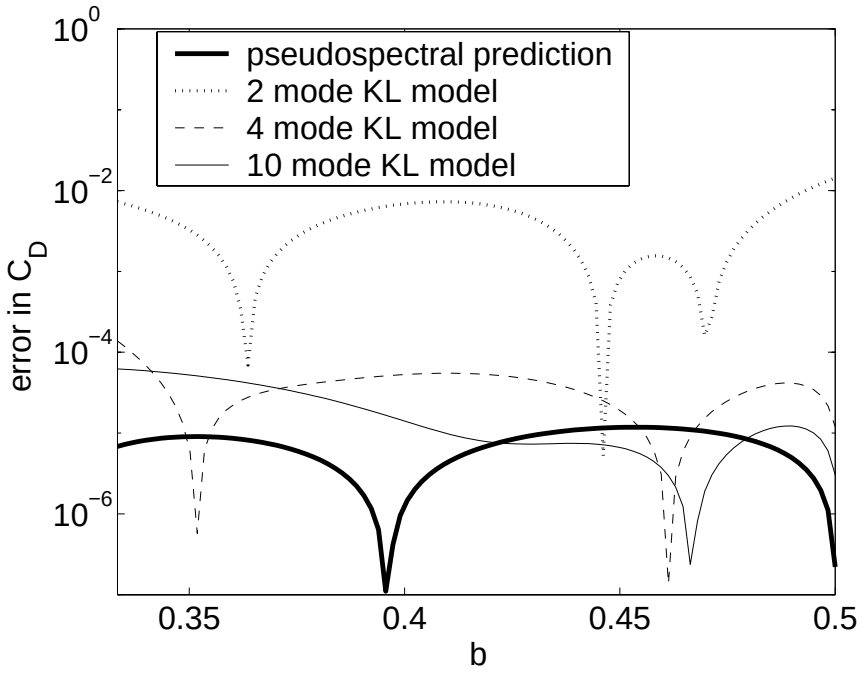

Figure 4.22. KL model $L_\infty[\Omega]$ error in ρ for a 17×9 grid, $b \in [1/3, 1/2]$, $\mathcal{M}_\infty = 3.5$. Errors determined by comparison to highly resolved 33×17 grid.

over another part favors the KL model. This seems likely since the plot of $L_\infty[\Omega]$ error in $\rho(\xi, \eta)$ from Figure 4.21 shows convergence in number of KL modes down to the level of accuracy in the snapshots.

In Figures 4.23 and 4.24, we show the plot of C_D versus b for KL models using various numbers of KL modes compared to C_D from the pseudospectral solver on the same 17×9 grid. It is seen that for the KL model with one or two modes, the prediction is fairly poor; in fact, for the case of one KL mode, the trend of decreasing C_D with increasing b is the opposite of what it should be. Including at least three KL modes in the model yields very good agreement with the actual solution. There is a bias error in the prediction of C_D versus b for KL models with greater than four modes. The bias error is on the order of the error for the pseudospectral prediction on a 17×9 grid, Fig. 4.21, from which the KL model was developed, so that this

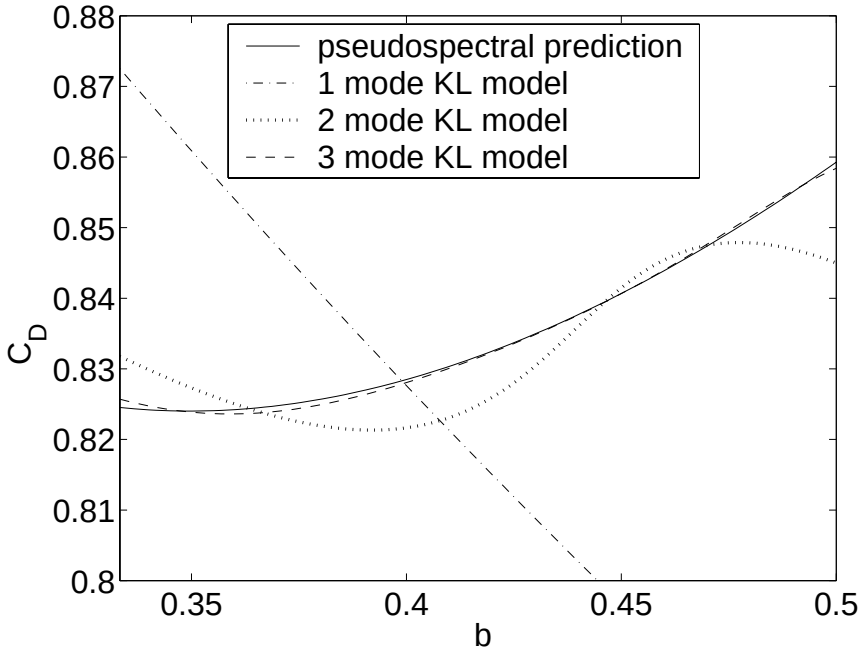

Figure 4.23. C_D versus b for the KL model built from 10 snapshots on a 17×9 grid, $\mathcal{M}_\infty = 3.5$

bias error is within the error tolerance of the KL model. From Figure 4.24 it is seen that the optimum value of b is 0.35 and the drag value for this geometry is $C_D = 0.824$.

Now we develop a KL model taking only three snapshots at $b = 1/3$, $5/12$, and $1/2$ from the pseudospectral solution on a 17×9 grid and compare the predictions for C_D from this KL model to a quadratic polynomial fit of the three snapshots. The plot of C_D versus b for the three mode KL model and the quadratic fit are shown in Figures 4.25 and 4.26 compared to C_D from the pseudospectral solver on the same 17×9 grid. The equation for the quadratic fit of C_D versus b is $C_D = 1.4601676 - 1.0082742b + 0.9983798b^2$. It is seen that the dependence of C_D on b is approximated quite well using a quadratic polynomial so that the three mode KL model is actually a less accurate approximation of C_D.

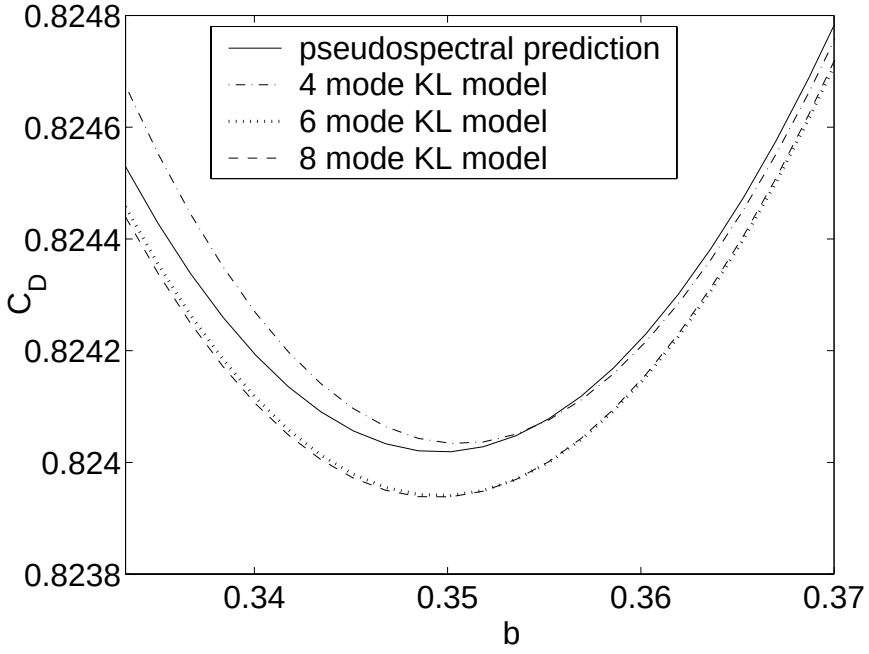

Figure 4.24. Magnification of C_D versus b for the KL model built from 10 snapshots on a 17×9 grid, $\mathcal{M}_\infty = 3.5$

4.5.3 Efficiency of Karhunen-Loève Model Versus Pseudospectral Solver

Figure 4.27 shows the error in the optimum C_D versus CPU time in seconds for both the KL model and pseudospectral solver along with linear fits of the data points to make comparison easier. The various data points representing the pseudospectral solutions are found by varying the number of grid points; finer grids yield more accurate results but also take longer to compute. The data points representing the KL model are all from KL models built with ten uniform snapshots over the range $b \in [1/3, 1/2]$ but with various levels of grid refinement and number of modes. The accuracy and computational cost for the KL model are functions of both the grid refinement in the snapshots and the number of modes used in the approximation; finer grid snapshots and more modes used in the KL model increase the accuracy of the predictions, but also the computational cost. In Figure 4.27 it is seen that

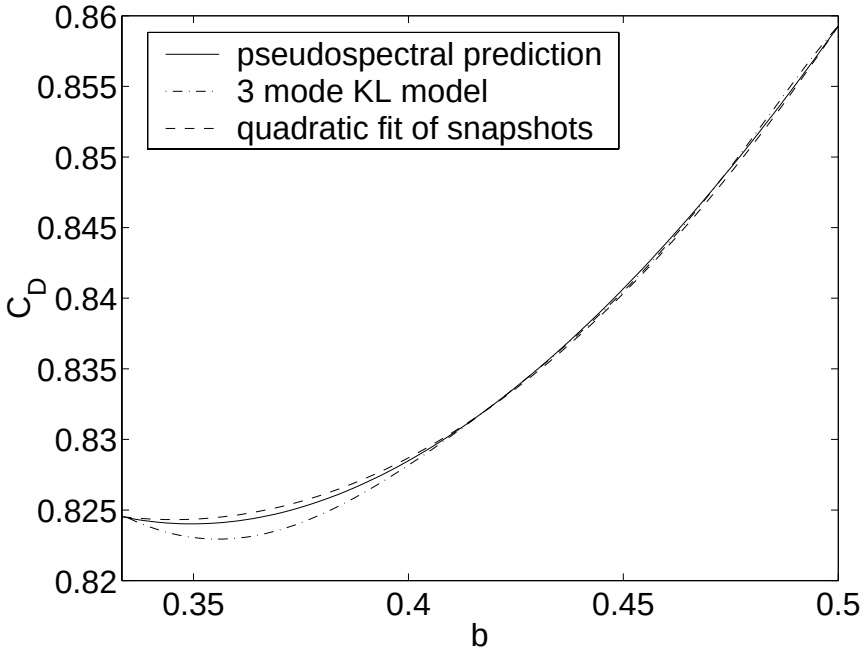

Figure 4.25. C_D versus b for the KL model built from 3 snapshots on a 17×9 grid and a quadratic fit of C_D from the same 3 snapshots, $\mathcal{M}_\infty = 3.5$

the KL model and pseudospectral method predictions have the same slope of error versus CPU time with the KL model at a slightly lower CPU time for the same level of accuracy.

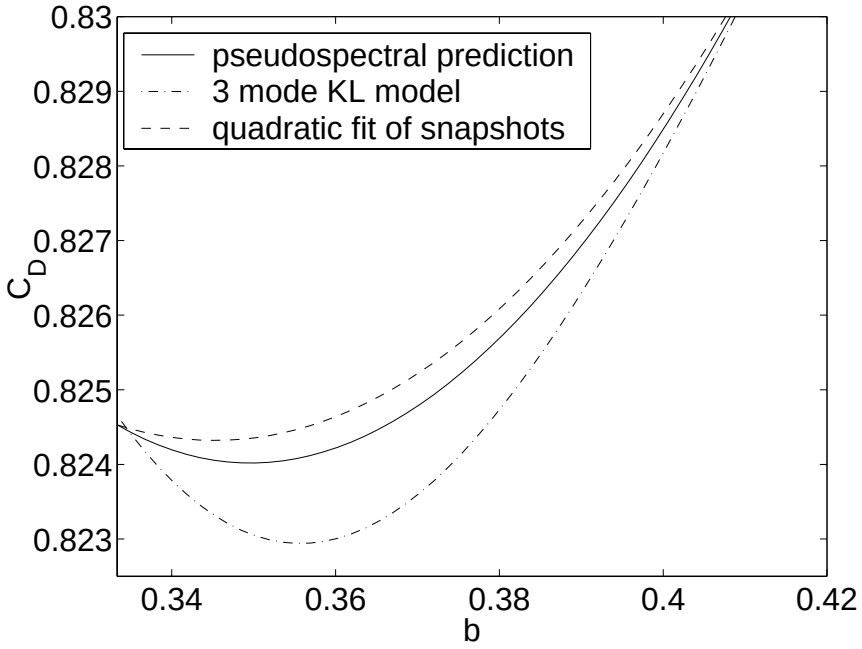

Figure 4.26. Magnification of C_D versus b for the KL model built from 3 snapshots on a 17×9 grid and a quadratic fit of C_D from the same 3 snapshots, $\mathcal{M}_\infty = 3.5$

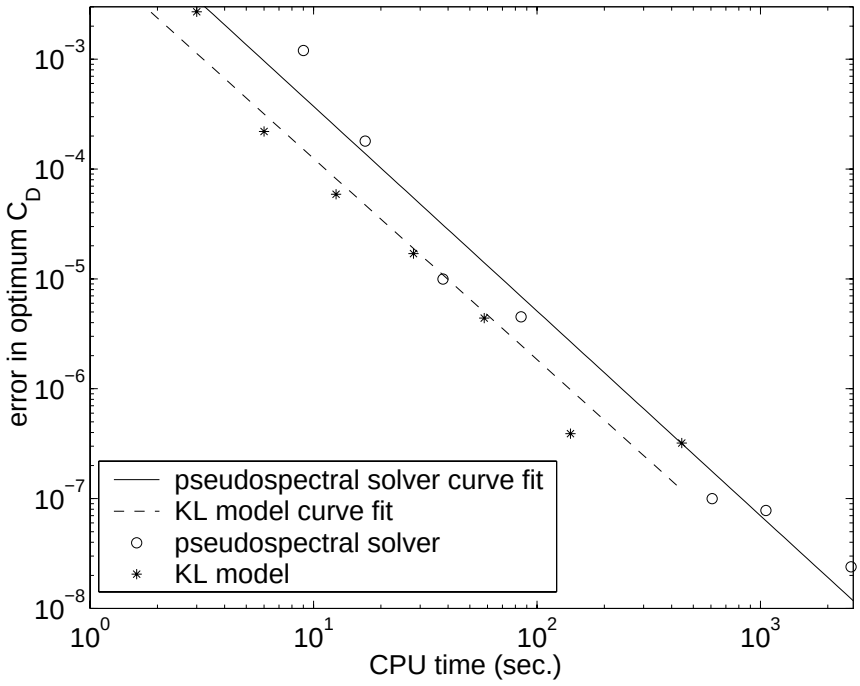

Figure 4.27. Error in the optimum C_D versus CPU cost in seconds for the KL model and pseudospectral solver, $\mathcal{M}_\infty = 3.5$ Errors determined by comparison to highly resolved 33×17 grid.

CHAPTER 5

CONCLUSIONS

5.1 Heat Conduction Problem

A KL Galerkin model was developed for a two-dimensional linear heat conduction problem with two different types of boundary conditions. The first boundary condition was multi-mode while the second one was a finite mode boundary condition in the sense that the exact separation of variables solution has only three terms in the series expansion of the solution. Comparing the efficiency of the KL Galerkin method with the pseudospectral method and a second order finite difference method, it was seen that both the KL Galerkin and pseudospectral methods were significantly more efficient than the second order finite difference method for both types of boundary conditions. The computational cost of sampling the design space and building the KL model was not included in the solution cost of the KL model even though this may add a significant amount of computational cost to the overall design process. The efficiency results of the heat conduction problem indicate that the higher efficiency of the KL method with respect to pseudospectral methods is problem-dependent. For the heat conduction problem with an infinite number of modes in the separation of variables solution, the pseudospectral method does not converge in a spectral manner, the KL method still converges spectrally, and consequently offers a significant increase in efficiency over the pseudospectral

method. On the other hand, for the heat conduction problem with only three terms in the separation of variables solution, both the pseudospectral method and the KL Galerkin methods converge spectrally.

A comparison of the accuracy of the KL model in predicting the average temperature as a function of aspect ratio built from only three snapshots with a quadratic polynomial least squares fit, or one dimensional response surface, for T_{avg} versus Γ revealed that the KL model was significantly more accurate. Although the computational cost of predicting T_{avg} by the KL method is more than that of the response surface, for a given level of accuracy the KL method may be more efficient since fewer design space samples would be needed for the KL method to achieve a specified accuracy level over the response surface method. As a consequence, the cost of building the KL model would be significantly less than the response surface particularly when multiple design variables are considered.

5.2 Blunt Body Problem

A pseudospectral numerical approximation technique was developed for the inviscid supersonic flow over a blunt body geometry. The discretized form of the governing equations and boundary conditions were formulated in terms of a system of ODEs which are solvable using a standard ODE solver. Due to the fitting of the shock and use of global polynomials in the solution approximation, the pseudospectral results show high accuracy and spectral convergence with number of nodes.

A KL least-squares model for the supersonic flow over a blunt body geometry was developed. The error convergence rate for the KL model is rapid, with the maximum accuracy level achieved with five KL modes for the single design variable problem posed. The maximum accuracy of the KL model is theoretically limited to the accuracy of the snapshots from which the model was built, and the results shown

here support the theoretical accuracy limit. Comparison of the computational cost of the KL model versus the pseudospectral method reveals slightly lower cost for the KL model than for the pseudospectral method. This is due to the fact that both the pseudospectral and KL least-squares methods exhibit spectral convergence rates. Given the additional overhead in sampling the design space, finding and then storing the KL eigenmodes, the advantage of using the KL method in favor of a direct solver is not clear, since the direct solver in this case is of comparable efficiency. Furthermore, it has been shown that for the blunt body optimal design problem, representing the functional dependence of C_D on b by a quadratic polynomial is more accurate than the predictions for C_D from a KL model employing three modes. Given that the computational cost of predicting C_D from a quadratic polynomial is much less than the cost of the KL model, it is not advantageous to use the KL method for this specific design problem.

The current work has contributed in beginning to make serious comparison of the computational efficiency of the KL method with other discrete approximations such as a second order finite difference and pseudospectral method, as well as comparing the accuracy of the KL method with response surfaces. These types of cost comparisons are something that has received little attention in the literature. Furthermore, although many researchers have employed finite difference, finite element, or finite volume methods with relatively low convergence rates in design applications, from the current results it may be worthwhile to explore the use of pseudospectral type methods instead. The current work has contributed also in beginning to compare the efficiency and accuracy of the KL method for different classes of problems such as linear versus nonlinear problems, infinite mode and finite mode problems. More work is needed to clarify what problems would be best solved by the KL method or would be more easily and efficiently solved by some other discrete method. Finally,

the current work is novel in that it is the first work to use shock fitting with the KL method, and one of the first studies where a KL model has been developed for a geometry in a supersonic flow.

5.3 Future Work

Future work includes the solution of multi-variable design problems using the KL method and the evaluation of the accuracy and efficiency of the KL method as compared with response surfaces with multiple design variables. Storage requirements for the KL method also need to be investigated as compared to the response surface method when full flow field information is necessary for the design problem. The KL method automatically retains all the flow field information whereas if the flow field is needed in the response surface method, the original flow field solutions must be retained. If more design space samples are required for the response surface to achieve the same level of accuracy as the KL method, then in addition to requiring longer to build the response surface model, it would also require more storage to maintain all the flow field information. The savings in both computational cost of building the model and the reduction in storage requirements could be significant for the KL method as compared to the response surface method particularly as the number of design variables increases, and this needs to be shown.

A Galerkin method employing Chebyshev polynomials as a basis, instead of the pseudospectral method using global Lagrange interpolating polynomials, needs to be implemented to determine whether the same poor convergence rate for the heat conduction problem with the infinite mode boundary condition is seen for both methods. In addition, if a Galerkin method employing Chebyshev polynomials is employed, the KL modes could be expressed as a linear combination of Chebyshev polynomials; this would reduce the storage requirements of the KL modes since

only the coefficients in the series expansion would have to be retained. Also, the computational cost for the Chebyshev based Galerkin and the KL Galerkin methods should be significantly less than the pseudospectral method employed here. This improvement in computational efficiency needs to be quantified.

The necessity to use shock fitting to obtain both the pseudospectral and KL model results in a significant complication that renders application of both methods difficult for problems with embedded discontinuities; nevertheless, recent work by Nasuti and Onofri [58], has shown promise in fitting complex two dimensional shock structures. In addition, although the topology of the current problem is simple enough to permit a single domain solution, for problems with more complex topologies, multiple shocks for example, a multi-domain pseudospectral method such as that proposed by Kopriva [59], is more convenient. Combining the shock fitting scheme of Nasuti and Onofri with the multi-domain pseudospectral method of Kopriva to obtain pseudospectral solutions for the supersonic flow over arbitrary two-dimensional geometries is an area for future research.

Assuming that one can obtain multi-domain solutions for problems with complex shocks, the next step would be the creation of a KL model. Creation of a multi-domain KL model by generating a separate set of KL modes for each domain should be possible; nevertheless, a methodology would be needed to handle situations where for example the shock structure changes resulting in a change in the number of domains as parameters in the problem change. It may not be clear for such problems the appropriate set of KL modes to use in approximating the solution in a particular domain.

Since the efficiency of the KL method suffers when the integrals in the KL model are evaluated each time the model is run, as is the case for general nonlinear problems, the possibility of generating approximations to these integrals at the time

of building the model needs to be investigated. Perhaps the governing equations could be linearized about a baseline geometry to remove the nonlinearity. The ability to evaluate the integral terms at the time of constructing the model is critical to developing KL models which are significantly less costly to run than discrete approximations such as the pseudospectral method, particularly when the cost of building the KL model is accounted for. A future paper will focus on comparing the computational cost for a linear heat conduction problem, where the integrals in the Galerkin formulation are evaluated at the time of building the model, versus a heat conduction problem with temperature dependent diffusivity, where the integrals in the Galerkin formulation are evaluated each time a new solution to the model is required. A linearization of the governing equations about a baseline geometry will also be performed and the results for accuracy and efficiency assessed.

APPENDIX A

KARHUNEN-LOÈVE DECOMPOSITION

Given a set of $F_k(\boldsymbol{\xi})$, $k = 1, ..., K$, we seek a set of real, orthonormal basis functions, $\widehat{\varphi}_i(\boldsymbol{\xi})$, *i.e.*

$$\int_\Omega \widehat{\varphi}_i(\boldsymbol{\xi})\,\widehat{\varphi}_j(\boldsymbol{\xi})\,d\boldsymbol{\xi} = \delta_{ij}, \quad i = 1, ..., L, \quad L \leq K, \tag{A.1}$$

and coefficients, c_{ki} such that approximating $F_k(\boldsymbol{\xi})$ by,

$$F_k(\boldsymbol{\xi}) \approx \sum_{i=1}^{L} c_{ki}\widehat{\varphi}_i(\boldsymbol{\xi}), \tag{A.2}$$

minimizes ε^2 in the following expression:

$$\varepsilon^2 = \frac{1}{K\int_\Omega d\boldsymbol{\xi}} \sum_{k=1}^{K} \int_\Omega \left(F_k(\boldsymbol{\xi}) - \sum_{i=1}^{L} c_{ki}\widehat{\varphi}_i(\boldsymbol{\xi}) \right)^2 d\boldsymbol{\xi}, \tag{A.3}$$

subject to the orthonormality constraint, Eq. (A.1). Here, $\boldsymbol{\xi} \equiv (\xi, \eta)$ is a spatial variable of dimension two defined over the domain, $\Omega : \{\xi \in [0,1], \eta \in [0,1]\}$.

At this point, let us assume that we have a set of orthonormal basis functions, $\widehat{\varphi}_i(\boldsymbol{\xi})$, $i = 1, ..., L$, and propose that the coefficients, c_{ki}, be

$$c_{ki} = \int_\Omega F_k(\boldsymbol{\xi})\,\widehat{\varphi}_i(\boldsymbol{\xi})\,d\boldsymbol{\xi}, \quad \begin{matrix} k = 1, ..., K \\ i = 1, ..., L \end{matrix}. \tag{A.4}$$

We will show that this choice yields a minimum value of ε^2. For any other choice of coefficients b_{ki}, ε^2 can be written

$$\varepsilon^2 = \frac{1}{K\int_\Omega d\boldsymbol{\xi}} \sum_{k=1}^{K} \int_\Omega \left(F_k(\boldsymbol{\xi}) - \sum_{i=1}^{L} b_{ki}\widehat{\varphi}_i(\boldsymbol{\xi}) \right)^2 d\boldsymbol{\xi}. \tag{A.5}$$

Substituting the following expression for the b_{ki},

$$\sum_{i=1}^{L} b_{ki} = \sum_{i=1}^{L} c_{ki} - \sum_{i=1}^{L} (c_{ki} - b_{ki}), \tag{A.6}$$

into Eq. (A.5) and making use of Eqs. (A.1) and (A.4), ε^2 in Eq. (A.5) is, after simplification,

$$\varepsilon^2 = \frac{1}{K \int_\Omega d\boldsymbol{\xi}} \sum_{k=1}^{K} \left(\int_\Omega \left(F_k(\boldsymbol{\xi}) - \sum_{i=1}^{L} c_{ki} \widehat{\varphi}_i(\boldsymbol{\xi}) \right)^2 d\boldsymbol{\xi} + \sum_{i=1}^{L} (c_{ki} - b_{ki})^2 \right), \tag{A.7}$$

from which it is clear that choosing $b_{ki} = c_{ki}$ minimizes ε^2.

Having found the optimal choice of c_{ki} from Eq. (A.4), the set of functions, $\widehat{\varphi}_i(\boldsymbol{\xi})$, $i = 1, ..., L$, which minimize ε^2 are found next. Let us expand the integrand in Eq. (A.3):

$$\begin{aligned} \varepsilon^2 = \frac{1}{K \int_\Omega d\boldsymbol{\xi}} \sum_{k=1}^{K} \Bigg(& \int_\Omega (F_k(\boldsymbol{\xi}))^2 d\boldsymbol{\xi} - 2 \sum_{i=1}^{L} c_{ki} \int_\Omega F_k(\boldsymbol{\xi}) \widehat{\varphi}_i(\boldsymbol{\xi}) d\boldsymbol{\xi} \\ & + \sum_{i=1}^{L} \sum_{j=1}^{L} c_{ki} c_{kj} \int_\Omega \widehat{\varphi}_i(\boldsymbol{\xi}) \widehat{\varphi}_j(\boldsymbol{\xi}) d\boldsymbol{\xi} \Bigg). \end{aligned} \tag{A.8}$$

Imposing the restriction of orthonormality from Eq. (A.1), Eq. (A.8) becomes:

$$\varepsilon^2 = \frac{1}{K \int_\Omega d\boldsymbol{\xi}} \sum_{m=1}^{K} \left(\int_\Omega (F_k(\boldsymbol{\xi}))^2 d\boldsymbol{\xi} - 2 \sum_{i=1}^{L} c_{ki} \int_\Omega F_k(\boldsymbol{\xi}) \widehat{\varphi}_i(\boldsymbol{\xi}) d\boldsymbol{\xi} + \sum_{i=1}^{L} c_{ki}^2 \right). \tag{A.9}$$

Substituting definition for c_{ki} from Eq. (A.4) into Eq. (A.9) yields

$$\varepsilon^2 = \frac{1}{K \int_\Omega d\boldsymbol{\xi}} \sum_{m=1}^{K} \left(\int_\Omega (F_k(\boldsymbol{\xi}))^2 d\boldsymbol{\xi} - \sum_{i=1}^{L} c_{ki}^2 \right), \tag{A.10}$$

or

$$\varepsilon^2 = \frac{1}{K \int_\Omega d\boldsymbol{\xi}} \sum_{k=1}^{K} \left(\int_\Omega (F_k(\boldsymbol{\xi}))^2 d\boldsymbol{\xi} - \sum_{i=1}^{L} \int_\Omega F_k(\boldsymbol{\xi}) \widehat{\varphi}_i(\boldsymbol{\xi}) d\boldsymbol{\xi} \int_\Omega F_k(\boldsymbol{\xi}') \widehat{\varphi}_i(\boldsymbol{\xi}') d\boldsymbol{\xi}' \right). \tag{A.11}$$

Observing that the terms $\int_\Omega [F_k(\boldsymbol{\xi})]^2 d\boldsymbol{\xi}$ and $\int_\Omega d\boldsymbol{\xi}$ in Eq. (A.11) are known constants, it is evident that minimizing ε^2 is equivalent to minimizing:

$$-\frac{1}{K} \sum_{k=1}^{K} \left(\sum_{i=1}^{L} \int_\Omega F_k(\boldsymbol{\xi}) \widehat{\varphi}_i(\boldsymbol{\xi}) d\boldsymbol{\xi} \int_\Omega F_k(\boldsymbol{\xi}') \widehat{\varphi}_i(\boldsymbol{\xi}') d\boldsymbol{\xi}' \right), \tag{A.12}$$

or upon interchanging integration and summation, minimizing ε^2 is equivalent to maximizing:

$$\int_\Omega \int_\Omega \mathbf{R}(\boldsymbol{\xi},\boldsymbol{\xi}') \sum_{i=1}^{L} \widehat{\varphi}_i(\boldsymbol{\xi}) \widehat{\varphi}_i(\boldsymbol{\xi}') d\boldsymbol{\xi} d\boldsymbol{\xi}', \tag{A.13}$$

where

$$\mathbf{R}(\boldsymbol{\xi},\boldsymbol{\xi}') = \frac{1}{K} \sum_{k=1}^{K} F_k(\boldsymbol{\xi}) F_k(\boldsymbol{\xi}'). \tag{A.14}$$

subject to Eq. (A.1) .

Next the maximization of Eq. (A.13) via calculus of variations is considered. Suppose that $\varphi_i(\boldsymbol{\xi})$, $i = 1, ..., L$, are the functions which maximize the expression in Eq. (A.13) . Then any functions, $\widehat{\varphi}_i(\boldsymbol{\xi})$, can be written as $\widehat{\varphi}_i(\boldsymbol{\xi}) = \varphi_i(\boldsymbol{\xi}) + \epsilon \widetilde{\varphi}_i(\boldsymbol{\xi})$, where ϵ is a constant and $\widetilde{\varphi}_i(\boldsymbol{\xi})$ is an arbitrary function. Substituting $\widehat{\varphi}_i(\boldsymbol{\xi}) = \varphi_i(\boldsymbol{\xi}) + \epsilon \widetilde{\varphi}_i(\boldsymbol{\xi})$ into Eq. (A.13) , the function to be maximized $f(\epsilon)$, becomes

$$f(\epsilon) = \int_\Omega \int_\Omega \mathbf{R}(\boldsymbol{\xi},\boldsymbol{\xi}') \sum_{i=1}^{L} \left(\varphi_i(\boldsymbol{\xi}) + \epsilon \widetilde{\varphi}_i(\boldsymbol{\xi})\right) \left(\varphi_i(\boldsymbol{\xi}') + \epsilon \widetilde{\varphi}_i(\boldsymbol{\xi}')\right) d\boldsymbol{\xi} d\boldsymbol{\xi}', \tag{A.15}$$

subject to Eq. (A.1) . In order to solve this constrained maximization problem, the method of Lagrange multipliers is employed, and a maximum for the following modified function $f^*(\epsilon)$ is sought:

$$\begin{aligned} f^*(\epsilon) = & \int_\Omega \int_\Omega \mathbf{R}(\boldsymbol{\xi},\boldsymbol{\xi}') \sum_{i=1}^{L} \left(\varphi_i(\boldsymbol{\xi}) + \epsilon \widetilde{\varphi}_i(\boldsymbol{\xi})\right) \left(\varphi_i(\boldsymbol{\xi}') + \epsilon \widetilde{\varphi}_i(\boldsymbol{\xi}')\right) d\boldsymbol{\xi} d\boldsymbol{\xi}' \\ & - \sum_{i=1}^{L} \lambda_i \left(\int_\Omega \left(\varphi_i(\boldsymbol{\xi}') + \epsilon \widetilde{\varphi}_i(\boldsymbol{\xi}')\right) \left(\varphi_i(\boldsymbol{\xi}') + \epsilon \widetilde{\varphi}_i(\boldsymbol{\xi}')\right) d\boldsymbol{\xi}' - 1 \right), \end{aligned} \tag{A.16}$$

where the λ_i are the Lagrange multipliers. Now for a maximum, it is required that $\frac{d}{d\epsilon} f^*(\epsilon) = 0$ at $\epsilon = 0$. Differentiating Eq. (A.16) with respect to ϵ and evaluating at $\epsilon = 0$ yields the following equation after simplifying

$$\begin{aligned} \frac{d}{d\epsilon} f^*(\epsilon)\Big|_{\epsilon=0} = & \int_\Omega \int_\Omega \mathbf{R}(\boldsymbol{\xi},\boldsymbol{\xi}') \sum_{i=1}^{L} \left(\varphi_i(\boldsymbol{\xi}) \widetilde{\varphi}_i(\boldsymbol{\xi}') + \widetilde{\varphi}_i(\boldsymbol{\xi}) \varphi_i(\boldsymbol{\xi}')\right) d\boldsymbol{\xi} d\boldsymbol{\xi}' \\ & - 2 \sum_{i=1}^{L} \lambda_i \int_\Omega \varphi_i(\boldsymbol{\xi}') \widetilde{\varphi}_i(\boldsymbol{\xi}') d\boldsymbol{\xi}' \\ & = 0. \end{aligned} \tag{A.17}$$

Since, by definition, $\mathbf{R}(\boldsymbol{\xi},\boldsymbol{\xi}') = \mathbf{R}(\boldsymbol{\xi}',\boldsymbol{\xi})$ in Eq. $(A.14)$, and since $\boldsymbol{\xi}$ and $\boldsymbol{\xi}'$ are dummy variables, it is observed that the two terms inside parenthesis in Eq. (A.17) are equivalent, so that Eq. (A.17) can be written as

$$\sum_{i=1}^{L} \int_{\Omega} \left(\int_{\Omega} \mathbf{R}(\boldsymbol{\xi},\boldsymbol{\xi}')\varphi_i(\boldsymbol{\xi})d\boldsymbol{\xi} - \lambda_i\varphi_i(\boldsymbol{\xi}') \right) \widetilde{\varphi}_i(\boldsymbol{\xi}')d\boldsymbol{\xi}' = 0. \tag{A.18}$$

From Eq. (A.18) it is seen that the quantity in parenthesis must be equal to zero since the $\widetilde{\varphi}_i(\boldsymbol{\xi}')$ are arbitrary and generally non-zero functions, so that Eq. (A.18) becomes

$$\int_{\Omega} \mathbf{R}(\boldsymbol{\xi},\boldsymbol{\xi}')\varphi_i(\boldsymbol{\xi})d\boldsymbol{\xi} = \lambda_i\varphi_i(\boldsymbol{\xi}'), \quad i = 1, ..., L. \tag{A.19}$$

It is recognized that Eq. $(A.19)$ is simply the definition for the eigensystem of the linear integral operator

$$\int_{\Omega} \mathbf{R}(\boldsymbol{\xi},\boldsymbol{\xi}') \left(\cdot\right) d\boldsymbol{\xi}, \tag{A.20}$$

so that the finite series of orthonormal functions which minimize Eq. (A.3) are the first L eigenfunctions of this operator. Since it is easily shown that the operator in Eq. (A.20) is self-adjoint, *i.e.*

$$\int_{\Omega} \left(\int_{\Omega} \mathbf{R}(\boldsymbol{\xi},\boldsymbol{\xi}')f(\boldsymbol{\xi})d\boldsymbol{\xi} \right) g(\boldsymbol{\xi}')d\boldsymbol{\xi}' = \int_{\Omega} \left(\int_{\Omega} \mathbf{R}(\boldsymbol{\xi},\boldsymbol{\xi}')g(\boldsymbol{\xi}')d\boldsymbol{\xi}' \right) f(\boldsymbol{\xi})d\boldsymbol{\xi}, \tag{A.21}$$

and positive definite, *i.e.*

$$\int_{\Omega} \left(\int_{\Omega} \mathbf{R}(\boldsymbol{\xi},\boldsymbol{\xi}')f(\boldsymbol{\xi})d\boldsymbol{\xi} \right) f(\boldsymbol{\xi}')d\boldsymbol{\xi}' > 0, \tag{A.22}$$

the eigenvalues, λ_i, are all real and positive.

Next the computation of the eigensystem in Eq. (A.19) by the method of snapshots as proposed by Sirovich [49] is considered. Since the kernel $\mathbf{R}(\boldsymbol{\xi},\boldsymbol{\xi}')$ is composed of K linearly independent solutions, $F_k(\boldsymbol{\xi})$, $k = 1, ..., K$, the eigenfunctions, $\varphi_i(\boldsymbol{\xi})$ can be expressed as a linear combination of these solutions, *i.e.*

$$\varphi_i(\boldsymbol{\xi}) = \sum_{j=1}^{K} \alpha_{ij}F_j(\boldsymbol{\xi}), \quad i = 1, ..., K. \tag{A.23}$$

The coefficients, α_{ij}, are found by substituting Eq. (A.23) into Eq. (A.19) and making use of Eq. (A.14) which yields

$$\int_\Omega \frac{1}{K}\sum_{k=1}^{K} F_k(\boldsymbol{\xi})F_k(\boldsymbol{\xi}')\sum_{j=1}^{K}\alpha_{ij}F_j(\boldsymbol{\xi})d\boldsymbol{\xi} \tag{A.24}$$
$$= \lambda_i \sum_{j=1}^{K}\alpha_{ij}F_j(\boldsymbol{\xi}'), \quad i = 1, ..., K,$$

or after simplifying

$$\sum_{k=1}^{K}\alpha_{ik}\beta_{jk} = \lambda_i\alpha_{ij}, \quad \begin{matrix} i = 1, ..., K, \\ j = 1, ..., K, \end{matrix} \tag{A.25}$$

where

$$\beta_{jk} = \frac{1}{K}\int_\Omega F_j(\boldsymbol{\xi})F_k(\boldsymbol{\xi})d\boldsymbol{\xi}. \tag{A.26}$$

Solving the discrete eigenvalue problem for the α_{ij} from Eq. (A.25), the eigenvectors of Eq. (A.20) are then reconstructed via Eq. (A.23). This procedure will be repeated for each of the six components of the steady state solution vector $x_k^q(\boldsymbol{\xi})$, $q = 1, ..., 6$, $k = 1, ..., K$, which includes the density, pressure, velocity components and the physical grid coordinates. For this multi component problem Eq. (A.19) becomes

$$\int_\Omega \mathbf{R}^q(\boldsymbol{\xi},\boldsymbol{\xi}')\varphi_k^q(\boldsymbol{\xi})d\boldsymbol{\xi} = \lambda_k^q\varphi_k^q(\boldsymbol{\xi}'), \quad \begin{matrix} q = 1, ..., 6, \\ k = 1, ..., K, \end{matrix} \tag{A.27}$$

where

$$\mathbf{R}^q(\boldsymbol{\xi},\boldsymbol{\xi}') = \frac{1}{K}\sum_{k=1}^{K} X_k^q(\boldsymbol{\xi})X_k^q(\boldsymbol{\xi}'). \tag{A.28}$$

APPENDIX B

INTERPOLATION ERROR USING LAGRANGE INTERPOLATING POLYNOMIALS

In calculating the derivatives of the Lagrange interpolating polynomials at the nodes, e.g. $\frac{dL_p^{(N)}}{d\xi}(\xi_n)$, there will be interpolation error. We will assess the magnitude of the interpolation error of the Lagrange interpolating polynomials by comparing the exponential function,

$$f(x) = e^x, \tag{B.1}$$

and its analytic first and second derivatives with its numerical approximations. Consistent with the methodology in the current work, we will approximate $f(x)$ in terms of Lagrange interpolating polynomials, *i.e.*

$$f(x) \approx \sum_{i=0}^{N} f(x_i) L_i^{(N)}(x). \tag{B.2}$$

The exact first and second derivatives of $f(x)$ are

$$\frac{df}{dx} = e^x, \tag{B.3}$$

$$\frac{d^2 f}{dx^2} = e^x, \tag{B.4}$$

and the numerical approximations are

$$\frac{df}{dx} \approx \sum_{i=0}^{N} f(x_i) \frac{dL_i^{(N)}}{dx}(x), \tag{B.5}$$

$$\frac{d^2 f}{dx^2} \approx \sum_{i=0}^{N} f(x_i) \frac{d^2 L_i^{(N)}}{dx^2}(x). \tag{B.6}$$

The derivatives of the Lagrange interpolating polynomials, $\frac{dL_i^{(N)}}{dx}(x)$ and $\frac{d^2 L_i^{(N)}}{dx^2}(x)$ are evaluated at the nodes x_p, $p = 0, ..., N$ according to the algorithm in [43]. The distribution of error in the function, first derivative, $\varepsilon'(x)$, and second derivative, $\varepsilon''(x)$, defined as follows:

$$\varepsilon(x) = \left| e^x - \sum_{i=0}^{N} f(x_i) L_i^{(N)}(x) \right|, \tag{B.7}$$

$$\varepsilon'(x) = \left| e^x - \sum_{i=0}^{N} f(x_i) \frac{dL_i^{(N)}}{dx}(x) \right|, \tag{B.8}$$

$$\varepsilon''(x) = \left| e^x - \sum_{i=0}^{N} f(x_i) \frac{d^2 L_i^{(N)}}{dx^2}(x) \right|, \tag{B.9}$$

are plotted for various values of N for both a Chebyshev and uniform grid distribution in Figures B.1, B.2, and B.3. As the value of N increases, the uniform grid exhibits a larger error at the endpoints than the Chebyshev grid. It is for this reason that a Chebyshev grid is preferred for numerically solving the problems.

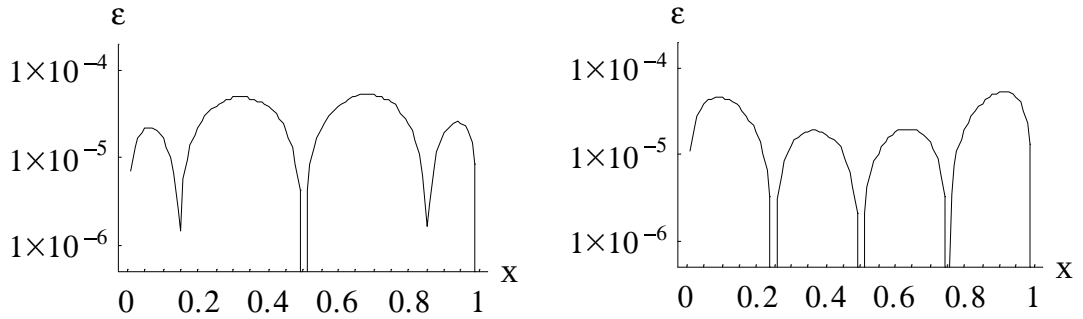

(a) 5 node Chebyshev grid

(b) 5 node uniform grid

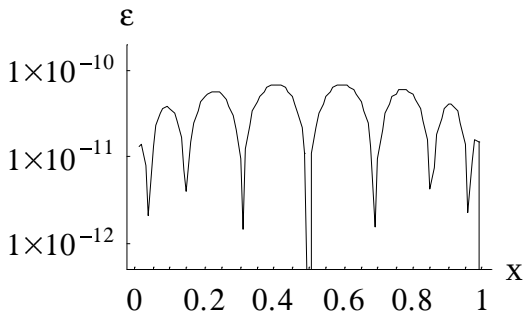

(c) 9 node Chebyshev grid

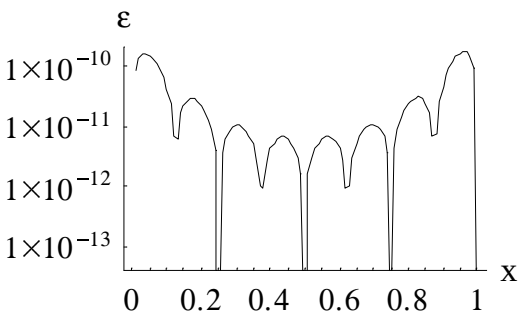

(d) 9 node uniform grid

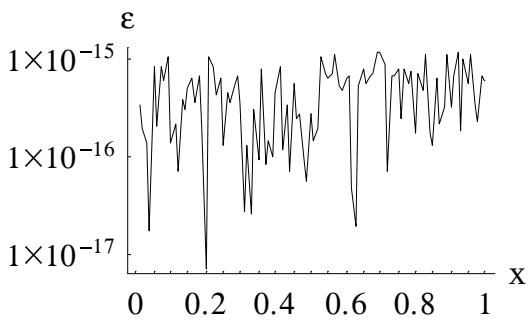

(e) 17 node Chebyshev grid

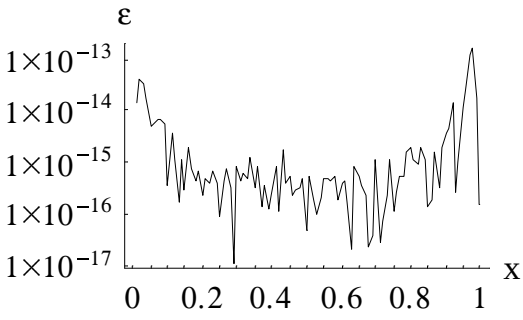

(f) 17 node uniform grid

Figure B.1. Interpolation error in approximating $y = e^x$.

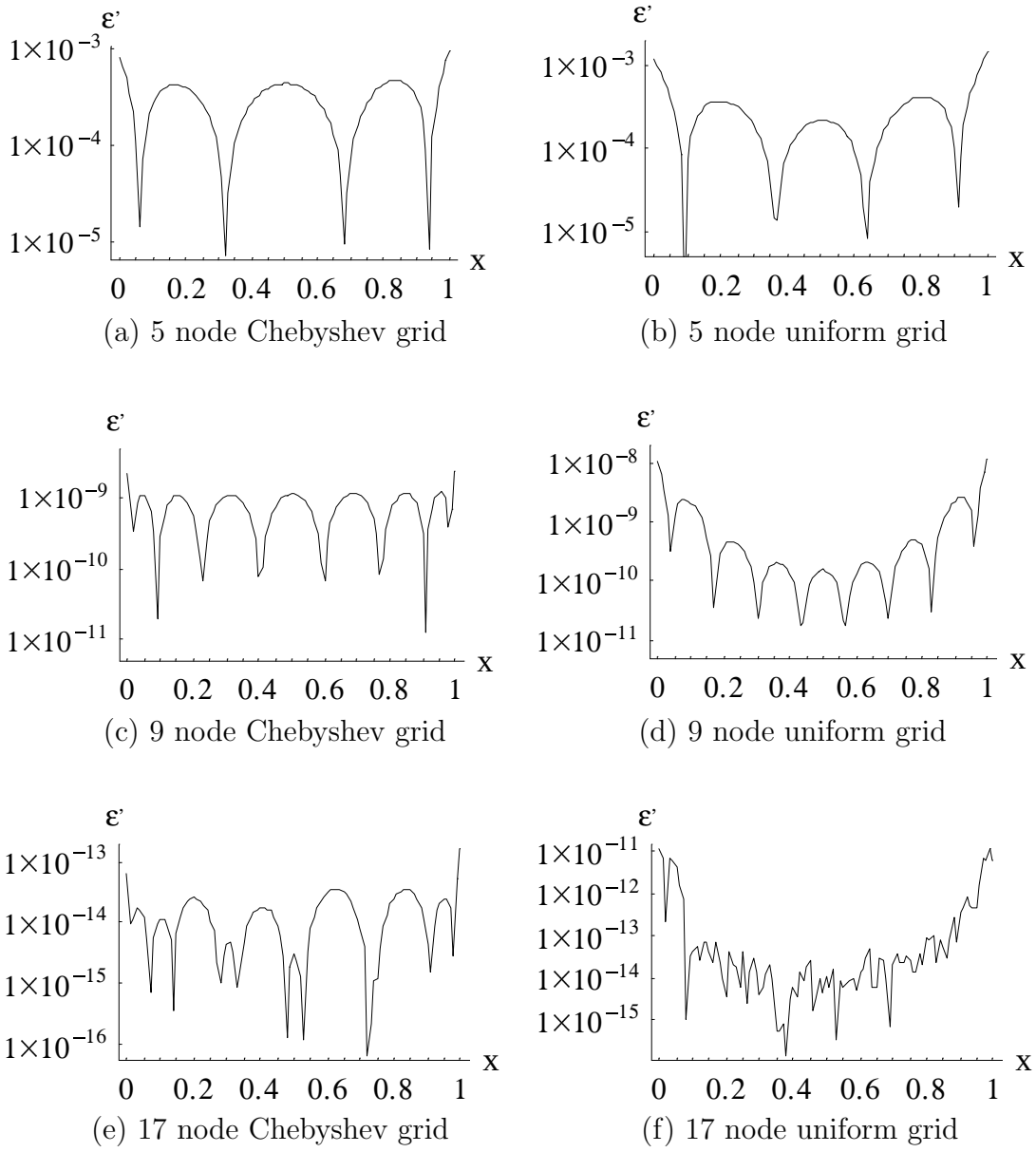

(a) 5 node Chebyshev grid

(b) 5 node uniform grid

(c) 9 node Chebyshev grid

(d) 9 node uniform grid

(e) 17 node Chebyshev grid

(f) 17 node uniform grid

Figure B.2. Interpolation error in approximating the first derivative of $y = e^x$.

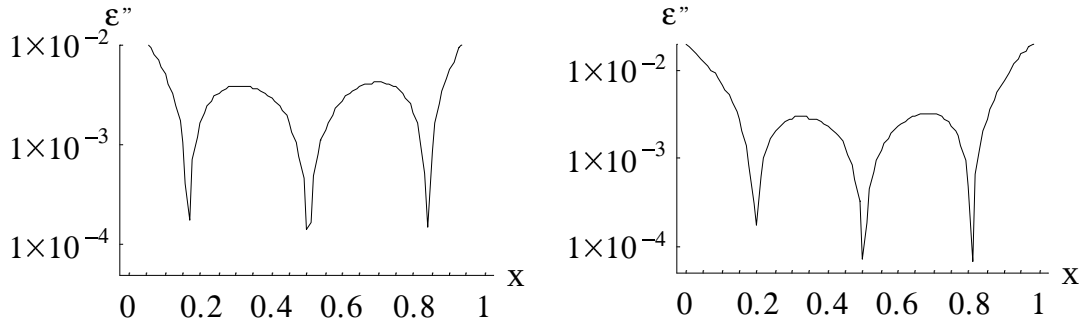

(a) 5 node Chebyshev grid

(b) 5 node uniform grid

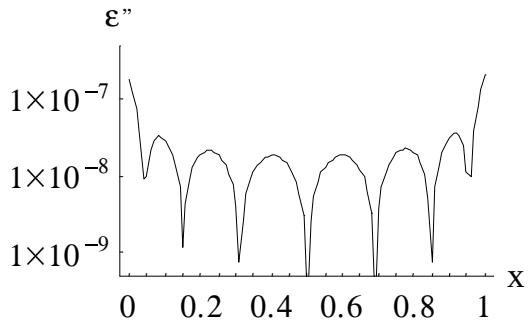

(c) 9 node Chebyshev grid

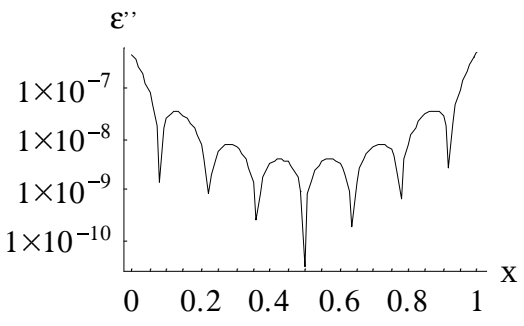

(d) 9 node uniform grid

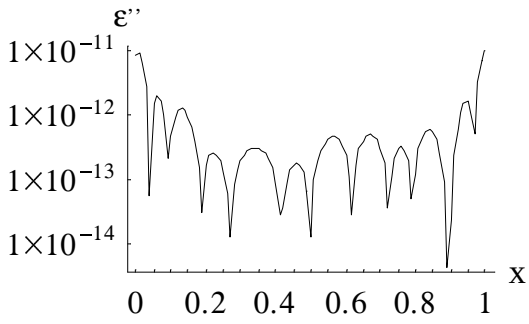

(e) 17 node Chebyshev grid

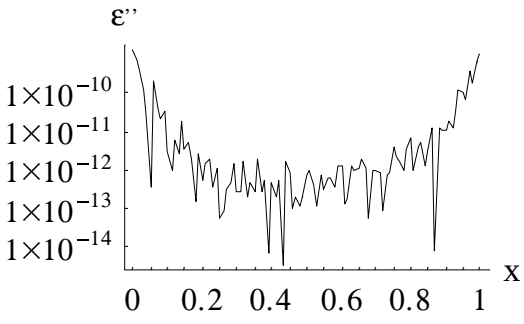

(f) 17 node uniform grid

Figure B.3. Interpolation error in approximating the second derivative of $y = e^x$.

APPENDIX C

SEPARATION OF VARIABLES SOLUTION FOR TWO-DIMENSIONAL HEAT CONDUCTION PROBLEM

The two-dimensional steady-state heat conduction equation,

$$\frac{\partial^2 T}{\partial x^2} + \Gamma^2 \frac{\partial^2 T}{\partial y^2} = 0, \tag{C.1}$$

and the following boundary conditions,

$$\frac{\partial T}{\partial x}(0, y) = \beta\sqrt{\Gamma} T(0, y), \tag{C.2}$$

$$\frac{\partial T}{\partial x}(1, y) = -\beta\sqrt{\Gamma} T(1, y), \tag{C.3}$$

$$\frac{\partial T}{\partial y}(x, 0) = -\frac{1}{\Gamma}, \tag{C.4}$$

$$\frac{\partial T}{\partial y}(x, 1) = -\frac{\beta}{\sqrt{\Gamma}} T(x, 1), \tag{C.5}$$

can be solved by the method of separation of variables. We will assume that $T(x, y)$ can be expressed as the product of two one-dimensional functions, i.e.

$$T(x, y) = F(x) G(y). \tag{C.6}$$

Substituting Eq. (C.6) into the governing equation, (C.1), we have

$$\frac{d^2 F}{dx^2} G + \Gamma^2 \frac{d^2 G}{dy^2} F = 0, \tag{C.7}$$

or

$$\frac{1}{F}\frac{d^2 F}{dx^2} = -\frac{\Gamma^2}{G}\frac{d^2 G}{dy^2}. \tag{C.8}$$

Since the left-hand side of Eq. (C.8) is a function of x only and the right-hand side is a function of y only, both sides must be equal to a constant which we will call σ^2. Eq. (C.8) becomes

$$\frac{1}{F}\frac{d^2F}{dx^2} = -\frac{\Gamma^2}{G}\frac{d^2G}{dy^2} = -\sigma^2, \tag{C.9}$$

or

$$\frac{d^2F}{dx^2} = -F\sigma^2, \tag{C.10}$$

and

$$\frac{d^2G}{dy^2} = \left(\frac{\sigma}{\Gamma}\right)^2 G. \tag{C.11}$$

Employing Eq. (C.6), the boundary conditions in Eqs. (C.2 – C.5) become the following

$$\frac{dF}{dx}(0) = \beta\sqrt{\Gamma}F(0), \tag{C.12}$$

$$\frac{dF}{dx}(1) = -\beta\sqrt{\Gamma}F(1), \tag{C.13}$$

$$F(x)\frac{dG}{dy}(0) = -\frac{1}{\Gamma}, \tag{C.14}$$

$$\frac{dG}{dy}(1) = -\frac{\beta}{\sqrt{\Gamma}}G(1). \tag{C.15}$$

The solution to Eq. (C.10) is

$$F(x) = c_1 \sin\sigma x + c_2 \cos\sigma x, \tag{C.16}$$

and the solution to Eq. (C.11) is

$$G(y) = c_3 \sinh\frac{\sigma}{\Gamma}y + c_4 \cosh\frac{\sigma}{\Gamma}y, \tag{C.17}$$

where c_1, c_2, c_3, c_4 and σ are unknown constants to be determined by enforcing the boundary conditions, Eqs. (C.12 – C.15). Substituting the expression for $F(x)$ from Eq. (C.16) into the first boundary condition for $F(x)$, Eq. (C.12), yields the following for c_1 in terms of c_2,

$$c_1 = \frac{\beta\sqrt{\Gamma}}{\sigma}c_2. \tag{C.18}$$

Substituting $F(x)$ into the second boundary condition for $F(x)$, Eq. (C.13), yields the following,

$$c_1\sigma\cos\sigma - c_2\sigma\sin\sigma = -\beta\sqrt{\Gamma}c_1\sin\sigma - \beta\sqrt{\Gamma}c_2\cos\sigma, \tag{C.19}$$

or making use of Eq. (C.18), we have after simplifying

$$\sigma^2\sin\sigma - 2\beta\sigma\sqrt{\Gamma}\cos\sigma - \beta^2\Gamma\sin\sigma = 0. \tag{C.20}$$

Eq. (C.20) can also be written as

$$\tan\sigma = 2\frac{\left(\sigma/\beta\sqrt{\Gamma}\right)}{\left(\frac{\sigma}{\beta\sqrt{\Gamma}}\right)^2 - 1}, \tag{C.21}$$

so that the discrete values of σ, denoted σ_k, $k = 1, ..., \infty$, which satisfy Eq. (C.20) can be graphically represented as the intersections of the two curves, Figure C.1, from the left and right sides of Eq. (C.21) respectively. Eq. (C.21) is an nonlinear function for σ with an infinite number of solutions, σ_k, $k = 1, ..., \infty$, where $\sigma_k \to (k-1)\pi$ in the limit as $k \to \infty$, as can be seen from Figure C.1. The function $F(x)$ which satisfies Eq. (C.10) and the boundary conditions is

$$F(x) = \sum_{k=1}^{\infty} c_k \left(\frac{\beta\sqrt{\Gamma}}{\sigma_k}\sin\sigma_k x + \cos\sigma_k x \right). \tag{C.22}$$

Now turning to the boundary condition on $G(y)$, Eq. (C.5), it will be enforced by substituting the expression for $G(y)$ from Eq. (C.17) into this equation to arrive at the following expression,

$$c_3\frac{\sigma}{\Gamma}\cosh\frac{\sigma}{\Gamma} + c_4\frac{\sigma}{\Gamma}\sinh\frac{\sigma}{\Gamma} = -\frac{\beta}{\sqrt{\Gamma}}\left(c_3\sinh\frac{\sigma}{\Gamma} + c_4\cosh\frac{\sigma}{\Gamma}\right). \tag{C.23}$$

Solving Eq. (C.23) for c_3 in terms of c_4 yields the following

$$c_3 = -\frac{\sigma\sinh\frac{\sigma}{\Gamma} + \beta\sqrt{\Gamma}\cosh\frac{\sigma}{\Gamma}}{\sigma\cosh\frac{\sigma}{\Gamma} + \beta\sqrt{\Gamma}\sinh\frac{\sigma}{\Gamma}}c_4, \tag{C.24}$$

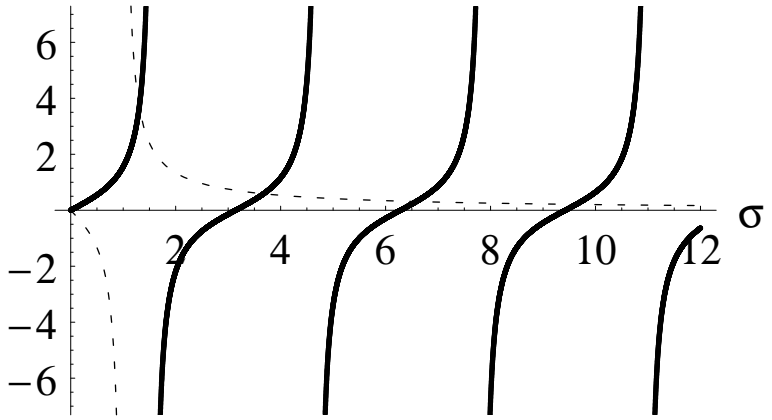

Figure C.1. Eigenvalues, σ_k, located at the intersection of two curves for $\beta = 1$, $\Gamma = 1$.

so that $G(y)$ becomes

$$G(y) = c_4 \left(\cosh \frac{\sigma_k}{\Gamma} y - h_k(\beta, \Gamma) \sinh \frac{\sigma_k}{\Gamma} y \right), \quad k = 1, ..., \infty, \tag{C.25}$$

where

$$h_k(\beta, \Gamma) = \frac{\sigma_k \sinh \frac{\sigma_k}{\Gamma} + \beta\sqrt{\Gamma} \cosh \frac{\sigma_k}{\Gamma}}{\sigma_k \cosh \frac{\sigma_k}{\Gamma} + \beta\sqrt{\Gamma} \sinh \frac{\sigma_k}{\Gamma}}. \tag{C.26}$$

The temperature distribution which satisfies the governing equation, Eq. (C.1), and three of the boundary conditions, Eqs. (C.2), (C.3) and (C.5), is

$$T(x, y) = \sum_{k=1}^{\infty} c_k \left(\frac{\beta\sqrt{\Gamma}}{\sigma_k} \sin \sigma_k x + \cos \sigma_k x \right) \left(\cosh \frac{\sigma_k}{\Gamma} y - h_k(\beta, \Gamma) \sinh \frac{\sigma_k}{\Gamma} y \right). \tag{C.27}$$

The fourth boundary condition, Eq. (C.4), can be enforced by substituting the expression for $T(x, y)$ from Eq. (C.27) into this equation and then solving for the unknown coefficients, c_k, $k = 1, ..., \infty$, *i.e.*

$$\sum_{k=1}^{\infty} c_k \left(\frac{\beta\sqrt{\Gamma}}{\sigma_k} \sin \sigma_k x + \cos \sigma_k x \right) h_k(\beta, \Gamma) \sigma_k = 1. \tag{C.28}$$

The coefficients, c_k, in Eq. (C.28) can be found by enforcing that the inner product of this equation with respect to each of the x-direction modal functions be equal to

zero, *i.e.*

$$\sum_{k=1}^{\infty} c_k h_k(\beta,\Gamma)\,\sigma_k \int_0^1 \left(\frac{\beta\sqrt{\Gamma}}{\sigma_k}\sin\sigma_k x+\cos\sigma_k x\right)\left(\frac{\beta\sqrt{\Gamma}}{\sigma_j}\sin\sigma_j x+\cos\sigma_j x\right)dx \tag{C.29}$$

$$=\int_0^1 \left(\frac{\beta\sqrt{\Gamma}}{\sigma_j}\sin\sigma_j x+\cos\sigma_j x\right)dx,\quad j=1,...,\infty.$$

Observing that if $k=j$ then $\int_0^1 \left(\frac{\beta\sqrt{\Gamma}}{\sigma_k}\sin\sigma_k x+\cos\sigma_k x\right)\left(\frac{\beta\sqrt{\Gamma}}{\sigma_j}\sin\sigma_j x+\cos\sigma_j x\right)dx = 0$, Eq. $(C.29)$ becomes

$$c_k h_k(\beta,\Gamma)\,\sigma_k \int_0^1 \left(\frac{\beta\sqrt{\Gamma}}{\sigma_k}\sin\sigma_k x+\cos\sigma_k x\right)^2 dx \tag{C.30}$$

$$=\int_0^1 \left(\frac{\beta\sqrt{\Gamma}}{\sigma_k}\sin\sigma_k x+\cos\sigma_k x\right)dx,\quad k=1,...,\infty,$$

so that the coefficients, c_k, are

$$c_k=\frac{\int_0^1 \left(\frac{\beta\sqrt{\Gamma}}{\sigma_k}\sin\sigma_k x+\cos\sigma_k x\right)dx}{h_k(\beta,\Gamma)\,\sigma_k\int_0^1 \left(\frac{\beta\sqrt{\Gamma}}{\sigma_k}\sin\sigma_k x+\cos\sigma_k x\right)^2 dx},\quad k=1,...,\infty, \tag{C.31}$$

or upon simplifying

$$\begin{aligned} c_k &= \frac{\left(4\beta\sqrt{\Gamma}\,(1-\cos\sigma_k)+4\sigma_k\sin\sigma_k\right)/h_k(\beta,\Gamma)}{\left(2\sigma_k\left(\beta\sqrt{\Gamma}+\beta^2\Gamma+\sigma_k^2-\beta\sqrt{\Gamma}\cos 2\sigma_k\right)+(\sigma_k^2-\beta^2\Gamma)\sin 2\sigma_k\right)}, \\ k &= 1,...,\infty. \end{aligned} \tag{C.32}$$

APPENDIX D

INTEGRATION BY PARTS IN TWO-DIMENSIONS FOR INCORPORATION OF BOUNDARY CONDITIONS IN THE GALERKIN METHOD OF WEIGHTED RESIDUALS

In order to incorporate the boundary conditions into the KL Galerkin approximation, we use integration by parts. In two dimensions, we will start with the two functions $F(x,y)$ and $G(x,y)$. Using the chain rule, the product $F(x,y)G(x,y)$ is differentiated in the following manner,

$$\frac{\partial\left(FG\right)}{\partial x}=\frac{\partial F}{\partial x}G+F\frac{\partial G}{\partial x}. \tag{D.1}$$

Then integrating both sides and rearranging terms yields,

$$\int_0^1\int_0^1 F\frac{\partial G}{\partial x}dxdy=\int_0^1\int_0^1\frac{\partial\left(FG\right)}{\partial x}dxdy-\int_0^1\int_0^1 G\frac{\partial F}{\partial x}dxdy. \tag{D.2}$$

We can simplify Eq. (D.2) further to yield,

$$\int_0^1\int_0^1 F\frac{\partial G}{\partial x}dxdy=\int_0^1\left[F\left(1,y\right)G\left(1,y\right)-F\left(0,y\right)G\left(0,y\right)\right]dy-\int_0^1\int_0^1 G\frac{\partial F}{\partial x}dxdy, \tag{D.3}$$

and in like manner

$$\int_0^1\int_0^1 F\frac{\partial G}{\partial y}dxdy=\int_0^1\left[F\left(x,1\right)G\left(x,1\right)-F\left(x,0\right)G\left(x,0\right)\right]dx-\int_0^1\int_0^1 G\frac{\partial F}{\partial y}dxdy. \tag{D.4}$$

Eqs. (D.3) and (D.4) are used in the heat conduction problem to incorporate the boundary conditions into the KL Galerkin approximation.

APPENDIX E

GAUSSIAN QUADRATURE AT ARBITRARY NODAL POINTS

The integrals in this work are evaluated by using Gauss-Legendre quadrature which is able to integrate polynomials of degree $2N+1$ using $N+1$ nodes. Since the spatial discretization of the governing equations has been accomplished by representing the solution as a sum of Lagrange interpolating polynomials, the approximate solution can be integrated exactly by using Gauss-Legendre quadrature with a sufficient number of nodes. If we have a polynomial $f^N(x)$ of degree N for example, then the Gauss-Legendre integration rule is

$$\int_{-1}^{1} f^N(x)dx = \sum_{i=1}^{N} \overline{w}_i f^N(\overline{x}_i). \tag{E.1}$$

There are well known routines for calculating the weights, $\overline{w}_i$, and the abscissas, $\overline{x}_i$, for example [60].

Since, in the current work, the nodal distribution for the pseudospectral solver was chosen to be a Chebyshev distribution, x_j, rather than a Legendre distribution, $\overline{x}_i$, it is necessary to find the weights, w_j, such that

$$\int_{-1}^{1} f^N(x)dx = \sum_{j=1}^{N} w_j f^N(x_j). \tag{E.2}$$

This is accomplished by recalling the approximation for $f^N(x)$ in terms of Lagrange interpolating polynomials, *i.e.*

$$f^N(x) = \sum_{j=1}^{N} f^N(x_j) L_j^{(N)}(x). \tag{E.3}$$

Eq. (E.3) is used to evaluate $f^N(x)$ at the Gauss-Legendre nodes, $\overline{x}_i$, as follows

$$f^N(\overline{x}_i) = \sum_{j=1}^{N} f^N(x_j) L_j^{(N)}(\overline{x}_i). \tag{E.4}$$

Substituting Eq. (E.4) into Eq. (E.1) yields the following

$$\int_{-1}^{1} f^N(x)dx = \sum_{i=1}^{N} \overline{w}_i \sum_{j=1}^{N} f^N(x_j) L_j^{(N)}(\overline{x}_i), \tag{E.5}$$

or after reversing the order of summation over i and j, we have

$$\int_{-1}^{1} f^N(x)dx = \sum_{j=1}^{N} \left[\sum_{i=1}^{N} \overline{w}_i L_j^{(N)}(\overline{x}_i) \right] f^N(x_j). \tag{E.6}$$

Clearly, Eq. (E.6) yields the weights, w_j, for Gaussian integration using the Chebyshev nodes, x_j, *i.e.*

$$w_j = \sum_{i=1}^{N} \overline{w}_i L_j^{(N)}(\overline{x}_i). \tag{E.7}$$

APPENDIX F

CROCCO'S THEOREM AND THE VORTICITY TRANSPORT EQUATION

F.1 Crocco's Theorem

It is common, especially in texts on compressible flow, to present what is known as Crocco's theorem. The many different versions presented in many standard texts are non-uniform and often of unclear validity. Its utility is confined mainly to providing an alternative way of expressing the linear momentum principle which provides some insight into the factors which influence fluid motion. In special cases, it can be integrated to form a more useful relationship, similar to Bernoulli's equation, between fundamental fluid variables. The heredity of this theorem is not always clear, though, as we shall see it is nothing more than a combination of the linear momentum principle coupled with some definitions from thermodynamics. Here we will first present a result valid for inviscid flows for the evolution of stagnation enthalpy, which is closely related to Crocco's theorem. Next we will show how the restrictions can be relaxed so as to obtain what we call the extended Crocco's theorem. We then show how this reduces to a form which is similar to a form presented in many texts.

F.1.1 Stagnation enthalpy variation

First consider the inviscid form of the linear momentum equation with no body force in Cartesian index notation,

$$\frac{\partial v_i}{\partial t} + v_j \frac{\partial v_i}{\partial x_j} = -\frac{1}{\rho}\frac{\partial p}{\partial x_i}. \tag{F.1}$$

Next, we make use of the following vector identity

$$v_j \frac{\partial v_i}{\partial x_j} = \frac{\partial}{\partial x_i}\left(\frac{v_j v_j}{2}\right) - \epsilon_{ijk} v_j \omega_k, \tag{F.2}$$

where the vorticity, ω_k, is defined as

$$\omega_k = \epsilon_{kmn}\frac{\partial v_n}{\partial x_m}, \tag{F.3}$$

and the alternating unit tensor ϵ_{ijk} of rank three is defined to be

$$\epsilon_{ijk} = \begin{cases} 1 & \text{if } ijk = 123, 231, \text{ or } 312, \\ 0 & \text{if any two indices are identical,} \\ -1 & \text{if } ijk = 321, 213, \text{ or } 132, \end{cases} \tag{F.4}$$

so that Eq. (F.1) becomes

$$\frac{\partial v_i}{\partial t} + \frac{\partial}{\partial x_i}\left(\frac{v_j v_j}{2}\right) - \epsilon_{ijk} v_j \omega_k = -\frac{1}{\rho}\frac{\partial p}{\partial x_i}. \tag{F.5}$$

Taking the dot product with v_i, and rearranging, we get

$$\frac{\partial}{\partial t}\left(\frac{v_i v_i}{2}\right) + v_i \frac{\partial}{\partial x_i}\left(\frac{v_j v_j}{2}\right) = \epsilon_{ijk} v_i v_j \omega_k - \frac{1}{\rho} v_i \frac{\partial p}{\partial x_i}. \tag{F.6}$$

Since ϵ_{ijk} is antisymmetric and $v_i v_j$ is symmetric, their tensor inner product is zero, so we get

$$\frac{\partial}{\partial t}\left(\frac{v_i v_i}{2}\right) + v_i \frac{\partial}{\partial x_i}\left(\frac{v_j v_j}{2}\right) = -\frac{1}{\rho} v_i \frac{\partial p}{\partial x_i}. \tag{F.7}$$

Now recall the Gibbs relation from thermodynamics, which in effect defines the entropy s,

$$Tds = de - \frac{p}{\rho^2} d\rho, \tag{F.8}$$

where e is the specific internal energy. The definition of enthalpy, h, is

$$h = e + \frac{p}{\rho}. \tag{F.9}$$

Differentiating the equation for enthalpy, we get

$$dh = de + \frac{1}{\rho}dp - \frac{p}{\rho^2}d\rho. \tag{F.10}$$

Eliminating de in favor of dh in the Gibbs equation gives

$$Tds = dh - \frac{1}{\rho}dp. \tag{F.11}$$

If we choose to apply this relation to the motion following a fluid particle, we can say then that

$$T\frac{ds}{dt} = \frac{dh}{dt} - \frac{1}{\rho}\frac{dp}{dt}. \tag{F.12}$$

Expanding, we get

$$T\left(\frac{\partial s}{\partial t} + v_i\frac{\partial s}{\partial x_i}\right) = \frac{\partial h}{\partial t} + v_i\frac{\partial h}{\partial x_i} - \frac{1}{\rho}\left(\frac{\partial p}{\partial t} + v_i\frac{\partial p}{\partial x_i}\right). \tag{F.13}$$

Rearranging, we get

$$T\left(\frac{\partial s}{\partial t} + v_i\frac{\partial s}{\partial x_i}\right) - \left(\frac{\partial h}{\partial t} + v_i\frac{\partial h}{\partial x_i}\right) + \frac{1}{\rho}\frac{\partial p}{\partial t} = -\frac{1}{\rho}v_i\frac{\partial p}{\partial x_i}. \tag{F.14}$$

We then use the above identity to eliminate the pressure gradient term from the linear momentum equation in favor of enthalpy, entropy, and unsteady pressure terms,

$$\frac{\partial}{\partial t}\left(\frac{v_i v_i}{2}\right) + v_i\frac{\partial}{\partial x_i}\left(\frac{v_j v_j}{2}\right) = T\left(\frac{\partial s}{\partial t} + v_i\frac{\partial s}{\partial x_i}\right) - \left(\frac{\partial h}{\partial t} + v_i\frac{\partial h}{\partial x_i}\right) + \frac{1}{\rho}\frac{\partial p}{\partial t}. \tag{F.15}$$

Rearranging slightly, noting that $v_i v_i = v_j v_j$, we get

$$\frac{\partial}{\partial t}\left(h + \frac{1}{2}v_j v_j\right) + v_i\frac{\partial}{\partial x_i}\left(h + \frac{1}{2}v_j v_j\right) = T\left(\frac{\partial s}{\partial t} + v_i\frac{\partial s}{\partial x_i}\right) + \frac{1}{\rho}\frac{\partial p}{\partial t}. \tag{F.16}$$

If we define, as is common, the total enthalpy h_o as

$$h_o = h + \frac{1}{2} v_j v_j, \tag{F.17}$$

we can then state

$$\frac{\partial h_o}{\partial t} + v_i \frac{\partial h_o}{\partial x_i} = T \left(\frac{\partial s}{\partial t} + v_i \frac{\partial s}{\partial x_i} \right) + \frac{1}{\rho} \frac{\partial p}{\partial t}, \tag{F.18}$$

or

$$\frac{dh_o}{dt} = T \frac{ds}{dt} + \frac{1}{\rho} \frac{\partial p}{\partial t}. \tag{F.19}$$

We can use the first law of thermodynamics written in terms of entropy, which for this inviscid flow reduces to the isentropic relation

$$\frac{ds}{dt} = 0, \tag{F.20}$$

to eliminate the entropy derivative and arrive at

$$\rho \frac{dh_o}{dt} = \frac{\partial p}{\partial t}. \tag{F.21}$$

Thus we see that the time rate of change of the total enthalpy of a fluid particle in the absence of viscous effects is influenced only by an unsteady pressure field.

F.1.2 Extended Crocco's theorem

With a slight modification of the preceeding analysis, we arrive at what we will call the extended Crocco's theorem. Begin once more with the linear momentum equation, Eq. (F.5). Now assume we have a functional representation of enthalpy in the form

$$h = h\left(s, p\right). \tag{F.22}$$

Then we get

$$dh = \left. \frac{\partial h}{\partial s} \right|_p ds + \left. \frac{\partial h}{\partial p} \right|_s dp. \tag{F.23}$$

We also thus deduce from the Gibbs relation $dh = Tds + (1/\rho)\, dp$ that

$$\left.\frac{\partial h}{\partial s}\right|_p = T, \qquad \left.\frac{\partial h}{\partial p}\right|_s = \frac{1}{\rho}. \tag{F.24}$$

Now, since we have $h = h\,(s, p)$, we can take its derivative with respect to each and all of the coordinate directions to obtain

$$\frac{\partial h}{\partial x_i} = \left.\frac{\partial h}{\partial s}\right|_p \frac{\partial s}{\partial x_i} + \left.\frac{\partial h}{\partial p}\right|_s \frac{\partial p}{\partial x_i}. \tag{F.25}$$

Substituting known values for the thermodynamic derivatives, we get

$$\frac{\partial h}{\partial x_i} = T\frac{\partial s}{\partial x_i} + \frac{1}{\rho}\frac{\partial p}{\partial x_i}. \tag{F.26}$$

We can use this to eliminate directly the pressure gradient from the linear momentum equation, Eq. (F.5) to obtain

$$\frac{\partial v_i}{\partial t} + \frac{\partial}{\partial x_i}\left(\frac{v_j v_j}{2}\right) - \epsilon_{ijk} v_j \omega_k = T\frac{\partial s}{\partial x_i} - \frac{\partial h}{\partial x_i}. \tag{F.27}$$

Rearranging slightly, we get the extended Crocco's theorem:

$$\frac{\partial v_i}{\partial t} + \frac{\partial}{\partial x_i}\left(h + \frac{v_j v_j}{2}\right) = T\frac{\partial s}{\partial x_i} + \epsilon_{ijk} v_j \omega_k. \tag{F.28}$$

Again, employing the total enthalpy, $h_o = h + \frac{1}{2} v_j v_j$, we write the extended Crocco's theorem as

$$\frac{\partial v_i}{\partial t} + \frac{\partial h_o}{\partial x_i} = T\frac{\partial s}{\partial x_i} + \epsilon_{ijk} v_j \omega_k. \tag{F.29}$$

F.1.3 Traditional Crocco's theorem

For a steady, inviscid flow, the extended Crocco's theorem reduces to what is usually called Crocco's theorem:

$$\frac{\partial h_o}{\partial x_i} = T\frac{\partial s}{\partial x_i} + \epsilon_{ijk} v_j \omega_k, \tag{F.30}$$

$$\nabla h_o = T\nabla s + \mathbf{v} \times \boldsymbol{\omega}, \tag{F.31}$$

where $\boldsymbol{\omega}$ is the vorticity vector. If the flow is further required to be homeoentropic, we get

$$\frac{\partial h_o}{\partial x_i} = \epsilon_{ijk} v_j \omega_k. \tag{F.32}$$

We then find that surfaces on which h_o is constant are parallel to both the velocity and vorticity vector fields. Taking the dot product with v_i, we get

$$\begin{aligned} v_i \frac{\partial h_o}{\partial x_i} &= v_i \epsilon_{ijk} v_j \omega_k, & \text{(F.33)} \\ v_i \frac{\partial h_o}{\partial x_i} &= \epsilon_{ijk} v_i v_j \omega_k, & \text{(F.34)} \\ &= 0, & \text{(F.35)} \end{aligned}$$

and likewise taking the dot product with ω_i, we get

$$\begin{aligned} \omega_i \frac{\partial h_o}{\partial x_i} &= \omega_i \epsilon_{ijk} v_j \omega_k, & \text{(F.36)} \\ \omega_i \frac{\partial h_o}{\partial x_i} &= \epsilon_{ijk} \omega_i v_j \omega_k, & \text{(F.37)} \\ &= 0. & \text{(F.38)} \end{aligned}$$

For a local coordinate system which has component s aligned with the velocity vector v_i, and the other two directions n, and b, mutually orthogonal, we have $v_i = (v_s, 0, 0)^T$. Eq. (F.35) then reduces to

$$(v_s, 0, 0) \cdot \begin{pmatrix} \frac{\partial h_o}{\partial s} \\ \frac{\partial h_o}{\partial n} \\ \frac{\partial h_o}{\partial b} \end{pmatrix} = \mathbf{0}. \tag{F.39}$$

Forming this dot product yields

$$v_s \frac{\partial h_o}{\partial s} = 0. \tag{F.40}$$

For $v_s \neq 0$, we get that

$$h_o = C\,(n, b)\,. \tag{F.41}$$

On a particular streamline, the function $C(n, b)$ will be a constant, so we see that the stagnation enthalpy is constant along a streamline and varies from streamline to streamline. Upon integrating Eq. (F.32), it is evident that, if the flow is steady, homeoentropic, and irrotational, the total enthalpy will be constant throughout the flowfield:

$$h_o = C. \tag{F.42}$$

We also note that in the steady state limit, the stagnation enthalpy equation, Eq. (F.21), gives an identical expression as Crocco's theorem evaluated along a streamline, Eq. (F.35).

F.2 Vorticity transport equation

Here we will take the curl of the linear momenta principle, Eq. (F.1), to obtain a relationship, the vorticity transport equation, which shows how the vorticity field evolves in an inviscid fluid. Subsequently, the reduction of the vorticity transport equation in the limit of steady state and for a two-dimensional flow is presented. First we recall some useful vector identities:

$$(\mathbf{v} \cdot \nabla)\,\mathbf{v} = \nabla\left(\frac{\mathbf{v} \cdot \mathbf{v}}{2}\right) + \boldsymbol{\omega} \times \mathbf{v}, \tag{F.43}$$

$$\nabla \times (\mathbf{a} \times \mathbf{b}) = (\mathbf{b} \cdot \nabla)\,\mathbf{a} - (\mathbf{a} \cdot \nabla)\,\mathbf{b} + \mathbf{a}\,(\nabla \cdot \mathbf{b}) - \mathbf{b}\,(\nabla \cdot \mathbf{a}), \tag{F.44}$$

$$\nabla \times (\nabla\phi) = 0, \tag{F.45}$$

$$\nabla \cdot (\nabla \times \mathbf{v}) = \nabla \cdot \boldsymbol{\omega} = 0. \tag{F.46}$$

We start now with the linear momentum principle for a general inviscid fluid with no body force:

$$\frac{\partial \mathbf{v}}{\partial t} + (\mathbf{v} \cdot \nabla)\,\mathbf{v} = -\frac{1}{\rho}\nabla p. \tag{F.47}$$

We expand the term $(\mathbf{v}\cdot\nabla)\,\mathbf{v}$ and then apply the curl operator to both sides to get

$$\nabla\times\left(\frac{\partial\mathbf{v}}{\partial t}+\nabla\left(\frac{\mathbf{v}\cdot\mathbf{v}}{2}\right)+\boldsymbol{\omega}\times\mathbf{v}\right)=-\nabla\times\left(\frac{1}{\rho}\nabla p\right). \tag{F.48}$$

This becomes, via the linearity of the various operators,

$$\frac{\partial}{\partial t}\underbrace{(\nabla\times\mathbf{v})}_{\boldsymbol{\omega}}+\underbrace{\nabla\times\left(\nabla\left(\frac{\mathbf{v}\cdot\mathbf{v}}{2}\right)\right)}_{=0}+\nabla\times\boldsymbol{\omega}\times\mathbf{v}=-\nabla\times\left(\frac{1}{\rho}\nabla p\right). \tag{F.49}$$

Using our vector identity for the term with two cross products we get

$$\underbrace{\frac{\partial\boldsymbol{\omega}}{\partial t}+(\mathbf{v}\cdot\nabla)\,\boldsymbol{\omega}}_{=\frac{d\boldsymbol{\omega}}{dt}}-(\boldsymbol{\omega}\cdot\nabla)\,\mathbf{v}+\boldsymbol{\omega}(\underbrace{\nabla\cdot\mathbf{v}}_{=-\frac{1}{\rho}\frac{d\rho}{dt}})-\mathbf{v}(\underbrace{\nabla\cdot\boldsymbol{\omega}}_{=0})=-\nabla\times\left(\frac{1}{\rho}\nabla p\right). \tag{F.50}$$

Rearranging, we have

$$\frac{d\boldsymbol{\omega}}{dt}-\frac{\boldsymbol{\omega}}{\rho}\frac{d\rho}{dt}=(\boldsymbol{\omega}\cdot\nabla)\,\mathbf{v}-\nabla\times\left(\frac{1}{\rho}\nabla p\right), \tag{F.51}$$

$$\frac{1}{\rho}\frac{d\boldsymbol{\omega}}{dt}-\frac{\boldsymbol{\omega}}{\rho^2}\frac{d\rho}{dt}=\left(\frac{\boldsymbol{\omega}}{\rho}\cdot\nabla\right)\mathbf{v}-\frac{1}{\rho}\nabla\times\left(\frac{1}{\rho}\nabla p\right), \tag{F.52}$$

$$\frac{d}{dt}\left(\frac{\boldsymbol{\omega}}{\rho}\right)=\left(\frac{\boldsymbol{\omega}}{\rho}\cdot\nabla\right)\mathbf{v}-\frac{1}{\rho}\nabla\times\left(\frac{1}{\rho}\nabla p\right). \tag{F.53}$$

Now consider the term $\nabla\times\left(\frac{1}{\rho}\nabla p\right)$. In Einstein notation, we have

$$\epsilon_{ijk}\frac{\partial}{\partial x_j}\left(\frac{1}{\rho}\frac{\partial p}{\partial x_k}\right) = \epsilon_{ijk}\left(\frac{1}{\rho}\frac{\partial^2 p}{\partial x_j\partial x_k}-\frac{1}{\rho^2}\frac{\partial\rho}{\partial x_j}\frac{\partial p}{\partial x_k}\right), \tag{F.54}$$

$$= \frac{1}{\rho}\underbrace{\epsilon_{ijk}\frac{\partial^2 p}{\partial x_j\partial x_k}}_{=0}-\frac{1}{\rho^2}\epsilon_{ijk}\frac{\partial\rho}{\partial x_j}\frac{\partial p}{\partial x_k}, \tag{F.55}$$

$$= -\frac{1}{\rho^2}\nabla\rho\times\nabla p. \tag{F.56}$$

Multiplying both sides by ρ,we write the final general form of the vorticity transport equation as

$$\rho\frac{d}{dt}\left(\frac{\boldsymbol{\omega}}{\rho}\right)=\underbrace{(\boldsymbol{\omega}\cdot\nabla)\,\mathbf{v}}_{A}+\underbrace{\frac{1}{\rho^2}\nabla\rho\times\nabla p}_{B}. \tag{F.57}$$

Here we see that the evolution of vorticity scaled by the density is affected by two physical processes, namely

- A: bending and stretching of vortex tubes,

- B: non-barotropic, also known as baroclinic, effects (if a fluid is barotropic, then $p = p(\rho)$ and $\nabla p = \frac{dp}{d\rho}\nabla\rho$ thus $\nabla\rho \times \nabla p = \nabla\rho \times \left(\frac{dp}{d\rho}\right)\nabla\rho = 0$.).

Another variation of the vorticity transport equation can be found by starting with the vorticity transport equation in the form of Eq. (F.53). Then, from the Gibbs equation in the form of Eq. (F.26) we solve for the pressure gradient in terms of gradients in enthalpy and entropy:

$$\frac{1}{\rho}\nabla p = \nabla h - T\nabla s. \tag{F.58}$$

Eliminating the pressure gradient term in Eq. (F.53) using the Gibbs equation yields the following form of the vorticity transport equation

$$\frac{d}{dt}\left(\frac{\boldsymbol{\omega}}{\rho}\right) = \left(\frac{\boldsymbol{\omega}}{\rho}\cdot\nabla\right)\mathbf{v} - \frac{1}{\rho}\nabla\times(\nabla h - T\nabla s) \tag{F.59}$$

Now consider the term $\nabla\times(\nabla h - T\nabla s)$. Employing the vector identity $\nabla\times(\nabla\phi) = 0$, this term reduces to $-\nabla\times(T\nabla s)$. In Einstein notation, we have

$$\begin{aligned} -\epsilon_{ijk}\frac{\partial}{\partial x_j}\left(T\frac{\partial s}{\partial x_k}\right) &= -\epsilon_{ijk}\left(T\frac{\partial^2 s}{\partial x_j\partial x_k} + \frac{\partial T}{\partial x_j}\frac{\partial s}{\partial x_k}\right), &\text{(F.60)}\\ &= -T\underbrace{\epsilon_{ijk}\frac{\partial^2 s}{\partial x_j\partial x_k}}_{=0} - \epsilon_{ijk}\frac{\partial T}{\partial x_j}\frac{\partial s}{\partial x_k}, &\text{(F.61)}\\ &= -\nabla T\times\nabla s. &\text{(F.62)}\end{aligned}$$

The vorticity transport equation can be written in the following form:

$$\frac{d}{dt}\left(\frac{\boldsymbol{\omega}}{\rho}\right) = \left(\frac{\boldsymbol{\omega}}{\rho}\cdot\nabla\right)\mathbf{v} + \frac{1}{\rho}(\nabla T\times\nabla s), \tag{F.63}$$

or by multiplying both sides by ρ, we write the final general form of the vorticity transport equation as

$$\rho\frac{d}{dt}\left(\frac{\boldsymbol{\omega}}{\rho}\right) = (\boldsymbol{\omega}\cdot\nabla)\mathbf{v} + \nabla T\times\nabla s. \tag{F.64}$$

Both forms of the vorticity transport equation, Eqs. (F.53) and (F.63), were first published by Vazsonyi [61], and are sometimes referred to as the vorticity transport equation of Vazsonyi.

APPENDIX G

TAYLOR-MACCOLL SIMILARITY SOLUTION

A brief description of the geometry, governing equations and numerical technique for the solution to the axisymmetric, inviscid, non heat conducting, supersonic flow of a calorically perfect, ideal gas over a cone at zero angle of inclination to a uniform freestream flow, *i.e.* Taylor-Maccoll flow, [54], is presented here. The geometry of the problem is shown in Figure G.1 , where $\mathcal{M}_\infty$ is the freestream Mach number, θ_C, and θ_S are the cone and shock angles respectively, r^* and θ are the two coordinate directions, and u_r^* and u_θ^* are the dimensional components of velocity in the r^* and θ directions, respectively.

The steady-state continuity, r^*- and $\theta-$ momenta, and energy equations in semi-conservative form for an axisymmetric problem are

$$\frac{1}{r^{*2}}\frac{\partial}{\partial r^*}\left(r^{*2}\rho^* u_r^*\right) + \frac{1}{r^*\sin\theta}\frac{\partial}{\partial\theta}\left(\rho^* u_\theta^*\sin\theta\right) = 0, \tag{G.1}$$

$$\frac{1}{r^{*2}}\frac{\partial}{\partial r^*}\left(r^{*2}\rho^* u_r^{*2}\right) + \frac{1}{r^*\sin\theta}\frac{\partial}{\partial\theta}\left(\rho^* u_r^* u_\theta^*\sin\theta\right) + \frac{\partial p^*}{\partial r^*} = \frac{\rho^* u_\theta^{*2}}{r^*}, \tag{G.2}$$

$$\frac{1}{r^{*2}}\frac{\partial}{\partial r^*}\left(r^{*2}\rho^* u_r^* u_\theta^*\right) + \frac{1}{r^*\sin\theta}\frac{\partial}{\partial\theta}\left(\rho^* u_\theta^{*2}\sin\theta\right) + \frac{1}{r^*}\frac{\partial p^*}{\partial\theta} = -\frac{\rho^* u_r^* u_\theta^*}{r^*}, \tag{G.3}$$

$$\begin{aligned} &\frac{1}{r^{*2}}\frac{\partial}{\partial r^*}\left(\rho^* r^{*2}\left(e^* + \frac{\mathbf{v}^*\cdot\mathbf{v}^*}{2} + \frac{p^*}{\rho^*}\right)u_r^*\right) \\ &+\frac{1}{r^*\sin\theta}\frac{\partial}{\partial\theta}\left(\rho^* u_\theta^*\left(e^* + \frac{\mathbf{v}^*\cdot\mathbf{v}^*}{2} + \frac{p^*}{\rho^*}\right)\sin\theta\right) \\ = \;& 0, \end{aligned} \tag{G.4}$$

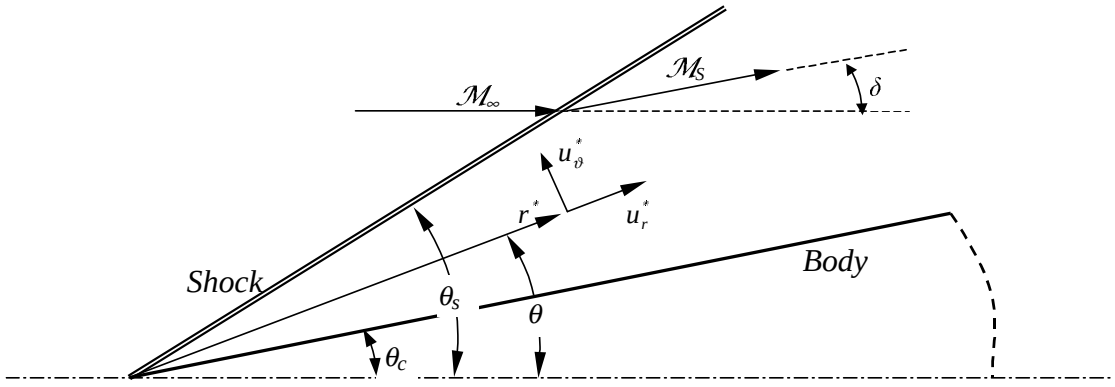

Figure G.1. Schematic of the supersonic flow about a cone.

where p^* is the pressure, ρ^* is the density, e^* is the internal energy, and $\mathbf{v}^*$ is the velocity vector. We will study solutions for which $\frac{\partial}{\partial r^*} = 0$, so that Eqs. (G.1 − G.4) become

$$\frac{d}{d\theta}\left(\rho^* u^*_\theta \sin\theta\right) = 0, \tag{G.5}$$

$$\frac{d}{d\theta}\left(\rho^* u^*_r u^*_\theta \sin\theta\right) - \rho^* u^{*2}_\theta \sin\theta = 0, \tag{G.6}$$

$$\frac{1}{\sin\theta}\frac{d}{d\theta}\left(\rho^* u^{*2}_\theta \sin\theta\right) + \frac{dp^*}{d\theta} + \rho^* u^*_r u^*_\theta = 0, \tag{G.7}$$

$$\frac{d}{d\theta}\left(\rho^* u^*_\theta \left(e^* + \frac{\mathbf{v}^*\cdot\mathbf{v}^*}{2} + \frac{p^*}{\rho^*}\right)\sin\theta\right) = 0; \tag{G.8}$$

in addition, the shock is assumed to have no curvature so no vorticity is generated at the shock boundary. The r^* momentum equation, Eq. (G.6) , after reduction via the continuity equation (G.5) can be written as

$$u^*_\theta - \frac{du^*_r}{d\theta} = 0. \tag{G.9}$$

We note that for this flow the vorticity,

$$\boldsymbol{\omega}^* = \nabla \times \mathbf{v}^*, \tag{G.10}$$

reduces to

$$\boldsymbol{\omega}^* = \begin{bmatrix} 0 \\ 0 \\ \frac{1}{r^*}\left(u_\theta^* - \frac{du_r^*}{d\theta}\right) \end{bmatrix}, \tag{G.11}$$

and thus from Eq. (G.9) , we conclude that $\boldsymbol{\omega}^* = \mathbf{0}$; the flow is irrotational. The energy equation, Eq. (G.8) , can be written in the following form

$$\frac{d}{d\theta}\left(\rho^* u_\theta^* h_o^* \sin\theta\right) = 0, \tag{G.12}$$

where

$$h_o^* = e^* + \frac{\mathbf{v}^* \cdot \mathbf{v}^*}{2} + \frac{p^*}{\rho^*}. \tag{G.13}$$

Making use of the continuity equation, Eq. (G.5) , Eq. (G.12) becomes

$$\frac{dh_o^*}{d\theta} = 0, \tag{G.14}$$

which, after integration, holds that the total enthalpy, h_o^*, is constant for the flow field. We also note that a standard Rankine-Hugoniot jump analysis shows that h_o^* is also constant across the oblique shock so that the stagnation enthalpy maintains the same value in the pre- and post-shock flow field. It is also well known, however, that the stagnation pressure and density suffer a jump over the oblique shock.

Since the definition of the enthalpy is

$$h^* = e^* + \frac{p^*}{\rho^*}, \tag{G.15}$$

Eq. (G.13) can also be expressed as

$$h_o^* = h^* + \frac{\mathbf{v}^* \cdot \mathbf{v}^*}{2}, \tag{G.16}$$

Since the flow is assumed to be calorically perfect, we have

$$h^* = c_p T^*, \tag{G.17}$$

where c_p is the specific heat at constant pressure. And for the ideal gas, we have

$$p^* = \rho^* R^* T^*, \tag{G.18}$$

where R^* is the specific gas constant. Combining Eq. (G.17) and Eq. (G.18) , we have the following expression for h^*

$$h^* = \frac{\gamma}{\gamma - 1}\frac{p^*}{\rho^*}, \tag{G.19}$$

where γ is the ratio of specific heats.

We now show that the flow is isentropic by starting with the following definition of entropy

$$T^* ds^* = dh^* - \frac{1}{\rho^*} dp^*, \tag{G.20}$$

which can be expressed as

$$T^* \frac{ds^*}{dt} = \frac{dh^*}{dt} - \frac{1}{\rho^*}\frac{dp^*}{dt}, \tag{G.21}$$

where $\frac{d}{dt} = \frac{\partial}{\partial t} + \mathbf{v}^* \cdot \nabla$ is the substantial derivative, which for the current problem becomes

$$T^* \frac{u_\theta^*}{r^*}\frac{ds^*}{d\theta} = \frac{u_\theta^*}{r^*}\frac{dh^*}{d\theta} - \frac{1}{\rho^*}\frac{u_\theta^*}{r^*}\frac{dp^*}{d\theta}, \tag{G.22}$$

or, for $u_\theta^* \neq 0$,

$$T^* \frac{ds^*}{d\theta} = \frac{dh^*}{d\theta} - \frac{1}{\rho^*}\frac{dp^*}{d\theta}. \tag{G.23}$$

Taking the derivative of Eq. (G.15) with respect to θ yields

$$\frac{dh^*}{d\theta} = \frac{de^*}{d\theta} + \frac{1}{\rho^*}\frac{dp^*}{d\theta} - \frac{p^*}{\rho^{*2}}\frac{d\rho^*}{d\theta}, \tag{G.24}$$

and taking derivatives of Eq. (G.13) with respect to θ yields

$$\frac{dh_o^*}{d\theta} = \frac{de^*}{d\theta} + \frac{1}{\rho^*}\frac{dp^*}{d\theta} - \frac{p^*}{\rho^{*2}}\frac{d\rho^*}{d\theta} + \mathbf{v}^* \cdot \frac{d\mathbf{v}^*}{d\theta} = 0, \tag{G.25}$$

so that substituting Eq. (G.25) into Eq. (G.24) yields

$$\frac{dh^*}{d\theta} = -\mathbf{v}^* \cdot \frac{d\mathbf{v}^*}{d\theta} = -u_r^*\frac{du_r^*}{d\theta} - u_\theta^*\frac{du_\theta^*}{d\theta}, \tag{G.26}$$

Substituting Eq. (G.26) into Eq. (G.23) , yields

$$T^* \frac{ds^*}{d\theta} = -u_r^* \frac{du_r^*}{d\theta} - u_\theta^* \frac{du_\theta^*}{d\theta} - \frac{1}{\rho^*} \frac{dp^*}{d\theta}. \tag{G.27}$$

Next, by making use of Eq. (G.5), the θ momentum equation, Eq. (G.7) , can be written in the following form

$$\frac{1}{\rho^*} \frac{dp^*}{d\theta} + u_\theta^* \frac{du_\theta^*}{d\theta} + u_\theta^* u_r^* = 0, \tag{G.28}$$

and substituting this into Eq. (G.27) yields

$$T^* \frac{ds^*}{d\theta} = u_r^* \left(u_\theta^* - \frac{du_r^*}{d\theta} \right). \tag{G.29}$$

Finally, employing Eq. (G.9) , Eq. (G.29) becomes

$$\frac{ds^*}{d\theta} = 0, \tag{G.30}$$

which holds that the entropy is constant throughout the flow field. We can therefore use the following isentropic relationship between p^* and ρ^*

$$\frac{p^*}{p_o^*} = \left(\frac{\rho^*}{\rho_o^*} \right)^\gamma, \tag{G.31}$$

where p_o^* and ρ_o^* are the post-shock stagnation pressure and density.

Substituting Eq. (G.31) into Eq. (G.19) yields the following equation for enthalpy,

$$h^* = \frac{\gamma p_o^* \rho^{*\gamma-1}}{(\gamma - 1)\, \rho_o^{*\gamma}}, \tag{G.32}$$

so that the expression for the total enthalpy in Eq. (G.16) becomes

$$h_o^* = \frac{1}{2} \left(u_r^{*2} + u_\theta^{*2} \right) + \frac{\gamma p_o^* \rho^{*\gamma-1}}{(\gamma - 1)\, \rho_o^{*\gamma}}. \tag{G.33}$$

Recalling that h_o^* is a constant and differentiating Eq. (G.33) with respect to θ yields

$$\frac{\gamma p_o^* \rho^{*\gamma-1}}{\rho_o^{*\gamma} \rho^*} \frac{d\rho^*}{d\theta} + u_r^* u_\theta^* + u_\theta^* \frac{du_\theta^*}{d\theta} = 0, \tag{G.34}$$

and substituting for $\frac{1}{\rho}\frac{d\rho^*}{d\theta}$ from the continuity equation, Eq. (G.5) , Eq. (G.34) becomes

$$u_r^* u_\theta^* + u_\theta^* \frac{du_\theta^*}{d\theta} - \frac{\gamma p_o^* \rho^{*\gamma-1}}{u_\theta^* \rho_o^{*\gamma}} \left(2u_r^* + u_\theta^* \cot\theta + \frac{du_\theta^*}{d\theta} \right) = 0. \tag{G.35}$$

Substituting $\frac{\gamma p_o^* \rho^{*\gamma-1}}{\rho_o^{*\gamma}}$ from Eq. (G.33) into Eq. (G.35) yields the following

$$\begin{aligned} & \frac{(\gamma-1)}{2} \left(2h_o^* - u_r^{*2} - u_\theta^{*2} \right) \left(2u_r^* + u_\theta^* \cot\theta + \frac{du_\theta^*}{d\theta} \right) \\ = \;& u_\theta^{*2} \left(u_r^* + \frac{du_\theta^*}{d\theta} \right), \end{aligned} \tag{G.36}$$

or upon rearranging we have

$$\frac{du_\theta^*}{d\theta} = \frac{u_\theta^{*2} u_r^* - \frac{(\gamma-1)}{2} \left(2h_o^* - u_r^{*2} - u_\theta^{*2} \right) \left(2u_r^* + u_\theta^* \cot\theta \right)}{\frac{(\gamma-1)}{2} \left(2h_o^* - u_r^{*2} - u_\theta^{*2} \right) - u_\theta^{*2}}. \tag{G.37}$$

The velocities, u_r^* and u_θ^* are nondimensionalized as follows

$$u_r = u_r^* / \sqrt{2h_o^*}, \tag{G.38}$$

$$u_\theta = u_\theta^* / \sqrt{2h_o^*}, \tag{G.39}$$

so that Eqs. (G.9) and (G.37) become

$$\frac{du_r}{d\theta} = u_\theta, \tag{G.40}$$

and

$$\frac{du_\theta}{d\theta} = \frac{u_\theta^2 u_r - \frac{(\gamma-1)}{2} \left(1 - u_r^2 - u_\theta^2 \right) \left(2u_r + u_\theta \cot\theta \right)}{\frac{(\gamma-1)}{2} \left(1 - u_r^2 - u_\theta^2 \right) - u_\theta^2} \tag{G.41}$$

respectively. The dimensionless density can be found as a function of u_r and u_θ by substituting Eq. (G.32) into Eq. (G.33) to yield the following

$$\rho = \left(1 - u_r^2 - u_\theta^2 \right)^{\frac{1}{\gamma-1}}, \tag{G.42}$$

where

$$\rho = \rho^* / \rho_o^*. \tag{G.43}$$

The dimensionless pressure can then be found by the isentropic relation in Eq. (G.31) , *i.e.*

$$p = \rho^{\gamma}, \tag{G.44}$$

where

$$p = p^*/p_o^*. \tag{G.45}$$

To solve the system of first order ODEs, Eqs. (G.40) and (G.41), initial conditions for u_r and u_θ are specified immediately downstream of the shock at $\theta = \theta_S$, denoted by u_{rS} and $u_{\theta S}$ as a function of $u_{r\infty}$, $\mathcal{M}_\infty$, θ_S, and γ from

$$u_{rS} = u_{r\infty}, \tag{G.46}$$

and

$$u_{\theta S} = u_{r\infty} \tan\left(\theta_S - \delta\right), \tag{G.47}$$

where

$$\delta = \tan^{-1}\left(2\left(\frac{\mathcal{M}_\infty^2 \sin^2\theta_S - 1}{\mathcal{M}_\infty^2\left(\gamma + \cos 2\theta_S\right) + 2}\right)\cot\theta_S\right). \tag{G.48}$$

Eq. (G.46) is the Rankine-Hugoniot condition which demands that the component of velocity in the direction tangent to the shock does not change across the shock, while Eq. (G.47) comes from both the geometry of the problem, Figure G.1, and Eq. (G.46) . The expression for the post-shock angle of the fluid velocity, δ, with respect to the pre-shock fluid velocity in Eq. (G.48) is a well known result of the Rankine-Hugoniot jump conditions across an oblique shock.

The numerical solution procedure is summarized by specifying $\mathcal{M}_\infty^2$, $u_{r\infty}$, γ, and θ_C and then by iterating on the value for θ_S until the condition that $u_\theta\left(\theta_C\right) = 0$ is satisfied for the desired cone angle, θ_C. For a particular guess of θ_S, the values of u_{rS}, and $u_{\theta S}$, are specified from Eqs. (G.46) and (G.47) , then the system of ODEs in Eqs. (G.40) and (G.41) are integrated form θ_S to θ_C. In order to

integrate Eqs. (G.40) and (G.41) using a standard ODE solver, it is necessary that the integration proceed in the direction of increasing θ rather than decreasing θ so that the following change of variables is needed

$$\theta = \theta_S - \widehat{\theta}, \tag{G.49}$$

so that

$$\frac{d}{d\theta} = -\frac{d}{d\widehat{\theta}}, \tag{G.50}$$

is substituted into Eqs. (G.40) and (G.41) and the resulting system of ODEs is integrated from $\widehat{\theta} = 0$ to $\widehat{\theta} = \theta_S - \theta_C$. If $u_\theta(\theta_C)$ does not equal zero, another guess is made for θ_S until $u_\theta(\theta_C) = 0$ is satisfied within a tolerance of 10^{-16} for the current problem. Once the solution for $u_r\left(\widehat{\theta}\right)$ and $u_\theta\left(\widehat{\theta}\right)$ where $\widehat{\theta} \in [0, \theta_S - \theta_C]$ is found, $u_r(\theta)$ and $u_\theta(\theta)$ are found as a function of θ from Eq. (G.49), and $\rho(\theta)$ and $p(\theta)$ are then taken from Eqs. (G.42) and (G.44) respectively. For verification of the pseudospectral solver, the velocity components u and w in the radial and axial directions respectively are needed, and can be found from the following equations

$$u = \sqrt{\frac{2\gamma p_o^* \rho_\infty^*}{(\gamma - 1)\rho_o^* p_\infty^*}} \left(u_r(\theta)\sin\theta - u_\theta(\theta)\cos\theta\right), \tag{G.51}$$

$$w = \sqrt{\frac{2\gamma p_o^* \rho_\infty^*}{(\gamma - 1)\rho_o^* p_\infty^*}} \left(u_r(\theta)\cos\theta + u_\theta(\theta)\sin\theta\right). \tag{G.52}$$

BIBLIOGRAPHY

[1] P. A. Gnoffo, J. K. Weilmuenster, H. H. Hamilton, D. R. Olynick, and E. Venkatapathy. Computational aerothermodynamic design issues for hypersonic vehicles. *Journal of Spacecraft and Rockets*, 36(1):21, 1999.

[2] J. F. Rodriguez, J. E. Renaud, B. A. Wujek, and R. V. Tappeta. Trust region model management in multidisciplinary design optimization. *Journal of Computational and Applied Mathematics*, 124:139, 2000.

[3] S. M. Batill and M. A. Stelmack. Framework for multidisciplinary design based on response-surface approximations. *Journal of Aircraft*, 36(1):287, 1999.

[4] A. Jameson. Re-engineering the design process through computation. *Journal of Aircraft*, 36(1):36, 1999.

[5] J. Reuther, J. J. Alonso, M. J. Rimlinger, and A. Jameson. Aerodynamic shape optimization of supersonic aircraft configurations via an adjoint formulation on distributed memory parallel computers. *Computers and Fluids*, 28:675, 1999.

[6] J. J. Reuther, A. Jameson, J. J. Alonso, M. J. Rimlinger, and D. Saunders. Constrained multipoint aerodynamic shape optimization using an adjoint formulation and parallel computers, parts 1-2. *Journal of Aircraft*, 36(1):51, 1999.

[7] J. L. Lion. *Optimal Control of Systems Governed by Partial Differential Equations*. Springer-Verlag, Berlin, 1971.

[8] H. M. Park and M. W. Lee. An efficient method of solving the Navier-Stokes equations for flow control. *International Journal for Numerical Methods in Engineering*, 41:1133, 1998.

[9] A. Theodoropoulou, R. A. Adomaitis, and E. Zafiriou. Model reduction for optimization of rapid thermal chemical deposition systems. *IEEE Transactions on Semiconductor Manufacturing*, 11(1):85, 1998.

[10] P. A. LeGresley and J. J. Alonso. Airfoil design optimization using reduced order models based on proper orthogonal decomposition. AIAA Paper 2000-2545, 2000.

[11] W. H. Jou, W. P. Huffman, D. P. Young, R.G. Melvin, M.B. Bieterman, C.L. Hilmes, and F.T. Johnson. Practical considerations in aerodynamic design optimization. AIAA Paper 95-1730-CP, 1995.

[12] N. Aubry, P. Holmes, J. L. Lumley, and E. Stone. The dynamics of coherent structures in the wall region of a turbulent boundary layer. *Journal of Fluid Mechanics*, 192:115, 1988.

[13] L. Sirovich and H. Park. Turbulent thermal convection in a finite domain: Part i. theory. *Physics of Fluids A*, 2(9):1649, 1990.

[14] H. Park and L. Sirovich. Turbulent thermal convection in a finite domain: Part ii. numerical results. *Physics of Fluids A*, 2(9):1659, 1990.

[15] C.-C. Chen and H.-C. Chang. Accelerated disturbance damping of an unknown distributed system by nonlinear feedback. *AIChE Journal*, 38(9):1461, 1992.

[16] H. M. Park and D. H. Cho. The use of the Karhunen-Loève decomposition for the modeling of distributed parameter systems. *Chemical Engineering Science*, 51(1):81, 1996.

[17] H. M. Park and M. W. Lee. An efficient method of solving the Navier-Stokes equations for flow control. *International Journal for Numerical Methods in Engineering*, 41:1133, 1998.

[18] H. M. Park and M. W. Lee. Boundary control of the Navier-Stokes equation by empirical reduction of modes. *Computer Methods in Applied Mechanics and Engineering*, 188:165, 2000.

[19] H. M. Park and M. W. Lee. Control of Navier-Stokes equations by means of mode reduction. *International Journal for Numerical Methods in Fluids*, 33:535, 2000.

[20] H. M. Park and J. H. Lee. A method of solving inverse convection problems by means of mode reduction. *Chemical Engineering Sciences*, 53(9):1731, 1998.

[21] H. M. Park and J. H. Lee. Reduction of modes for the solution of inverse natural convection problems. *Computer Methods in Applied Mechanics and Engineering*, 190:919, 2000.

[22] H. M. Park and J. H. Lee. Solution of an inverse heat transfer problem by means of empirical reduction of modes. *Zeitschrift fr angewandte Mathematik und Physik*, 51:17, 2000.

[23] H. M. Park and W. S. Jung. Recursive solution of an inverse heat transfer problem in rapid thermal processing systems. *International Journal of Heat and Mass Transfer*, 44:2053, 2001.

[24] H. M. Park and W. S. Jung. The Karhunen-Loève Galerkin method for the inverse natural convection problems. *International Journal of Heat and Mass Transfer*, 44:155, 2001.

[25] H. M. Park and T. Y. Yoon. Solution of inverse radiation problems using the Karhunen-Loève Galerkin procedure. *Journal of Quantitative Spectroscopy and Radiative Transfer*, 68:489, 2001.

[26] P. A. LeGresley and J. J. Alonso. Dynamic domain decomposition and error correction for reduced order models. AIAA Paper 2003-0250, 2003.

[27] D. J. Lucia. *Reduced Order Modeling for High Speed Flows with Moving Shocks*. PhD thesis, Air Force Institute of Technology, Wright-Patterson Air Force Base, Ohio, U.S.A., 2001.

[28] G. P. Brooks and J. M. Powers. A Karhunen-Loève least-squares technique for optimization of geometry of a blunt body in supersonic flow. *Journal of Computational Physics*, 2003. (In review).

[29] V. V. Rusanov. A blunt body in a supersonic stream. *Annual Review of Fluid Mechanics*, 8:377, 1976.

[30] W. D. Hayes and R. F. Probstein. *Hypersonic Flow Theory*, volume 1. Academic Press, New York, 1966.

[31] C. C. Lin and S. I. Rubinov. On the flow behind curved shocks. *Journal of Mathematics and Physics*, 27:105, 1948.

[32] P. R. Garabedian and H. M. Lieberstein. On the numerical calculation of detached bow shock waves in hypersonic flow. *Journal of the Aeronautical Sciences*, 25(1):109, 1958.

[33] M. D. Van Dyke. The supersonic blunt-body problem - review and extension. *Journal of the Aero/Space Sciences*, 25(4):485, 1958.

[34] M. W. Evans and F. H. Harlow. Calculation of supersonic flow past an axially symmetric cylinder. *Journal of the Aeronautical Sciences*, 25(1):269, 1958.

[35] G. Moretti and M. Abbett. A time-dependent computational method for blunt body flows. *AIAA Journal*, 4(12):2136, 1966.

[36] M. Y. Hussaini, D. A. Kopriva, M. D. Salas, and T. A. Zang. Spectral methods for the Euler equations: Part 2. Chebyshev methods and shock-fitting. *AIAA Journal*, 23(2):234, 1985.

[37] D. A. Kopriva, T. A. Zang, and M. Y. Hussaini. Spectral methods for the Euler equations: the blunt body problem revisited. *AIAA Journal*, 29(9):1458, 1991.

[38] G. P. Brooks and J. M. Powers. A Karhunen-Loève Galerkin technique with shock-fitting for optimization of a blunt body geometry. AIAA Paper 2002-3861, 2002.

[39] G. P. Brooks and J. M. Powers. A pseudospectral approximation of a blunt body in supersonic flow. *Journal of Computational Physics*, 2003. (In review).

[40] D. Gottlieb and S. Orszag. *Numerical Analysis of Spectral Methods: Theory and Applications*. SIAM-CBMS, Philadelphia, 1977.

[41] C. Canuto, M. Y. Hussaini, A. Quarteroni, and T. A. Zang. *Spectral Methods in Fluid Dynamics*. Springer-Verlag, 1988.

[42] D. Gottlieb and J. S. Hesthaven. Spectral methods for hyperbolic problems. *Journal of Computational and Applied Mathematics*, 128:83, 2001.

[43] B. Fornberg. *A Practical Guide to Psuedospectral Methods*. Cambridge University Press, 1998.

[44] B. A. Finlayson. *The Method of Weighted Residuals and Variational Principles*. Academic Press, New York, 1972.

[45] K. Karhunen. Zur spektraltheorie stochastischer prozesse. *Annales Academiae Scientiarum Fennicae*, 34, 1946.

[46] M. Loève. *Probability Theory*. Van Nostrand, Princeton, N.J., 1955.

[47] J. Lumley. *Stochastic Tools in Turbulence*. Academic Press, 1970.

[48] A. Rosenfeld and A. C. Kak. *Digital Picture Processing*. Academic Press, 1976.

[49] L. Sirovich. Turbulence and the dynamics of coherent structures. part 1-3. *Quarterly of Applied Mathematics*, 45(3):561, 1987.

[50] K. W. Thompson. Time dependent boundary conditions for hyperbolic systems. *Journal of Computational Physics*, 68:1, 1987.

[51] K. W. Thompson. Time dependent boundary conditions for hyperbolic systems, II. *Journal of Computational Physics*, 89:439, 1990.

[52] A. C. Hindmarsh. Odepack, a systematized collection of ODE solvers. In *et al.* R.S. Stepleman, editor, *Scientific Computing*, Amsterdam, page 55. North Holland, 1983.

[53] L. R. Petzold. Automatic selection of methods for solving stiff and nonstiff systems of ordinary differential equations. *SIAM Journal on Scientific Computing*, 4:136, 1983.

[54] G.I. Taylor and J.W. Maccoll. The air pressure on a cone moving at high speeds. *Proceedings of the Royal Society, Ser. A*, 139:278, 1933.

[55] L. Lees. Hypersonic flow. In *Proceedings of the Fifth International Aeronautical Conference*, Los Angeles, page 241. Institute of the Aeronautical Sciences, 1955.

[56] J. D. Anderson, Jr. *Hypersonic and High Temperature Gas Dynamics*. McGraw-Hill Inc., 1989.

[57] F. S. Billig. Shock-wave shapes around spherical and cylinder-nosed bodies. *Journal of Spacecraft and Rockets*, 4(6):822, 1967.

[58] F. Nasuti and M. Onofri. Analysis of unsteady supersonic viscous flows by a shock-fitting technique. *AIAA Journal*, 34(7):1428, 1996.

[59] D. A. Kopriva. Computation of hyperbolic equations on complicated domains with patched and overset Chebyshev grids. *SIAM Journal on Scientific and Statistical Computing*, 10(1):120, 1989.

[60] W. H. Press, S. A. Teukolsky, W. T. Vetterling, and Brian P. Flannery. *Numerical Recipes in Fortran.* Cambridge University Press, 2nd edition, 1992.

[61] A. Vazsonyi. On rotational gas flows. *Quarterly of Applied Mathematics*, 3:29, 1945.